A STUDY OF THE WEDGE CUTTING FORCE THROUGH TRANSVERSELY STIFFENED PLATES: AN APPLICATION TO SHIP GROUNDING RESISTANCE

by

PATRICK E. LITTLE

M.B.A., University of Baltimore, 1992
B.S., Marine Engineering, United States Coast Guard Academy, 1986

Submitted to the Departments of Ocean Engineering and Mechanical Engineering
in Partial Fulfillment of the Requirements for the Degrees of

MASTER OF SCIENCE IN NAVAL ARCHITECTURE AND MARINE ENGINEERING

and

MASTER OF SCIENCE IN MECHANICAL ENGINEERING

at the
Massachusetts Institute of Technology
May 1994

Signature of Author _____
Department of Ocean Engineering
May 1994

Certified by _____
Tomasz Wierzbicki
Professor of Applied Mechanics, Thesis Supervisor

Certified by _____
Frank A. McClintock
Professor of Mechanical Engineering, Thesis Reader

Accepted by _____
Professor Ain A. Sonin, Chairman
Department Graduate Committee
Department of Mechanical Engineering

Accepted by _____
Professor A. Douglas Carmichael
Department Graduate Chairman
Department of Ocean Engineering

A STUDY OF THE WEDGE CUTTING FORCE THROUGH TRANSVERSELY STIFFENED PLATES: AN APPLICATION TO SHIP GROUNDING RESISTANCE

by

Patrick E. Little

Submitted to the Departments of Ocean Engineering and Mechanical Engineering on May 13, 1994 in partial fulfillment of the requirements for the degrees of Master of Science in Naval Architecture and Marine Engineering and Master of Science of Mechanical Engineering

Abstract

Tests were made to study the contribution of transverse ship structural members to the grounding force on a ship. Two types of test specimens, scaled 1:16, were designed from a prototype very large crude oil carrier (VLCC). They consisted of a transverse member between two longitudinal members, with the variable being the width of the spacing between the longitudinal members. Two wedges were designed. A narrow wedge with a radiused cutting face was used with the narrower specimens. A wide wedge with a prismoid-type shape was used with the wider specimens. Four tests were conducted. The general trend for each test was similar, namely, a sharp rise in force as the wedge approached within seven to ten times the plate thickness of the transverse member, followed by a decay as the wedge passed through. The main difference between the narrow and wide specimens was that the decay on the wide specimen was more gradual.

The initial rise in force as the wedge approached the transverse member was described by a crack splitting model. The peak value of force was qualitatively attributed to the progressive crushing of corner elements formed at the intersection of the bottom plating with the transverse member. A simplified

analytical model was developed describing the force resulting from the interaction between the wedge and the transverse member. The simplified model ignored the initial stiffening and peak force.

The analytical model was compared to the experimental results and shown to underestimate the peak force by 20% for the narrow specimen/narrow wedge tests and by 5% for the wide specimen/wide wedge tests. A comparison of the work per length of cut was also made between the analytical model and test results. The analytical model was shown to estimate the work at the end of the test to within 5% for both types of tests.

Thesis Supervisor: Tomasz Wierzbicki
Title: Professor of Applied Mechanics

Acknowledgments

I would like to thank Professor Tomasz Wierzbicki for the guidance and support he has provided as my thesis advisor. The entire process has been a valuable learning experience for me. Thanks are also due to Professor Frank McClintock whose thought provoking questions, while never easy to answer, have provided valuable insight and elevated the quality of this thesis. Special thanks are due to Mr. Arthur Rudolph of the Civil Engineering Machine Shop. He not only skillfully manufactured many of the components used in the experiments, but also provided sound guidance which improved the experimental design and was of immeasurable value towards successful completion of the tests. Thanks are due to Mohamed and Mark for their assistance in the design and running of experiments, and providing counsel as needed. Finally, but most importantly, I wish to express my appreciation to my wife, Susan, and children, Brendan, Cameron and Sarah, for their love, sacrifice and perseverance during this work.

Table of Contents

List of Figures

List of Tables

1.0 - Introduction

1.1 Background

Throughout its history, waterborne transportation has had the potential for accidents such as collision at sea or grounding of a vessel upon a shoal. This has been accepted in the past as the price of doing business. Pushed along by the development of technology, ship sizes have increased dramatically in the last 40 years. As an example, prior to 1956, there were no tankers with a cargo size greater than 50,000 tons. Today, Ultra Large Crude Carriers, with a cargo capacity of greater than 400,000 tons, are not uncommon. The current magnitude of cargo size, coupled with the hazardous or toxic nature of the cargo, has resulted in a situation where even a small amount of damage can result in an environmental catastrophe.

Most of the attention of the maritime community in the past has been on the problem of collision at sea. The grounding of ships has remained a largely unexplored area. However, the grounding of the EXXON VALDEZ in Alaska's Prince William Sound in 1989 changed that. The sheer magnitude of the ensuing environmental disaster shocked the public's senses. This accident, and others in recent years, prompted the U.S. Congress to pass the Oil Pollution Act in August of 1990 (OPA 90). OPA 90 mandates that all U.S. and foreign flag vessels which operate on U.S. waters, and which are constructed or undergo major conversion after June 30, 1991, have a double hull to protect against the loss of cargo in the event of a collision or grounding. Vessels constructed earlier will be required to be fitted with a double hull by the year 2015.

It is worth noting that the selection of the double hull as the design of choice was a result of the political process in the U.S. There are alternative designs for reducing oil outflow in the event of a grounding or collision, including intermediate horizontal decks and hydrostatic control. The problem is that the technical and theoretical tools required to make an accurate and realistic assessment of different tanker designs do not currently exist in a complete form.

In order to develop such needed computational tools, a joint MIT-Industry Program on Safe Tankers was started in the summer of 1992. The primary goals of the program are to develop computational models to predict structural damage in grounding and collision, and to increase rupture resistance through improved hull design and fabrication techniques. The work is progressing by studying the mechanics associated with the basic damage modes encountered during a typical ship grounding. Once these basic modes of damage are understood, they can be combined and applied in a damage prediction model for a ship using the principles of crashworthiness engineering.

1.2 Goal of Present Research

The aim of the present research is to contribute to the state of the art in the prediction of damage to ships from groundings by studying the wedge cutting force through transversely stiffened plates. The research includes scale model tests and an analysis of the wedge cutting force. Most of the previous work on the steady-state damage process has focused on the cutting force through an unstiffened plate.

Chapter 1 provides an overview of the grounding process and a summary of the previous work in the area of plate cutting mechanics. Chapter 2

describes the design of small scale "ship" models and the experimental procedures used to perform small scale tests on them. Chapter 3 summarizes the results of the transversely stiffened plate cutting tests. A series of analytical models describing a transversely stiffened plate subjected to cutting is developed in Chapter 4. Chapter 5 contains conclusions drawn from the work and recommends areas for future study.

1.3 Grounding Scenario

For clarity during the discussion, Figure 1-1 illustrates in a simplified form the major structural members directly involved in grounding damage. They are the hull plating, longitudinal stiffeners, web frames and transverse bulkheads.

A brief overview of the grounding situation is useful in order to understand the context of the current research. Wierzbicki, Rady, Peer & Shin (1990) proposed a model of the grounding situation as follows. Consider a ship of mass M traveling with a forward speed V which strikes an underwater rock or reef. Damage is assumed to start at the bow, or forward part of the ship, and proceed toward the stern. The momentum of the ship, MV, is dissipated through any number of possible modes during the grounding. The process can be broken into four steps:

1. Outer dynamics of the grounding event
2. Initiation of local damage
3. Interaction between overall ship motion and localized damage
4. Steady-state damage

Outer dynamics refers to the rigid body motion used to determine the reaction forces between the ship and bottom during grounding . Initiation of local damage relates to the initial rock-hull interaction. The rock may rupture the skin of the hull or it may only dent the structure. The development of localized damage is defined by the magnitudes of the contact forces in the rigid-body motion of the ship and local crushing of the hull girder. The contact forces establish the penetration depth of the rock into the hull. Steady-state damage refers to the lengthwise damage to the ship hull by the rock caused by the dissipation of the ship's remaining momentum after the rock has reached its full penetration depth. Figure 1-2 illustrates a profile view of this situation. The effect of the sea-state is not considered.

This thesis focuses on Step 4 of the grounding , steady-state damage. It is assumed that the rock has already penetrated the hull and that the remaining momentum of the ship is being dissipated as the rock deforms the structural members in its path. The length of the damage zone from the damaging action of the rock is related to the grounding resistance of the ship structure and the amount of oil spilled. Each of the ship's structural members (plating, longitudinal stiffeners, transverse frames and bulkheads) contributes to this process.

1.4 Previous Work

Initial work in the field of ship collision resistance was presented by Minorsky (1959). His work involved the effectiveness of ship side protection against collision. The study was performed by analyzing the data from 50 ship collisions. Minorsky hypothesized the resistance of a ship to collision was proportional to the volume of material deformed during the collision. Resistance

is provided by structural members which have depth in the direction of impact, such as decks, flats, double bottoms, transverse bulkheads in the struck vessel and longitudinal bulkheads in the striking vessel. The shell plating in the struck vessel is not included, for example, because after the initial penetration, it provides negligible energy absorption. Thus, for each collision, Minorsky was able to calculate the kinetic energy lost from momentum principles and the resistance of the ship to a 90° collision from the volume of damaged material. For the ships studied, the relationship between energy absorbed in collision, E_T, and resistance to collision, R_T, is determined to be;

$$E_T = 414.5\ R_T + 121{,}900\ \text{Tons-Knots}^2. \qquad (1.1)$$

R_T is the damaged volume in units of length cubed, or $(\text{Feet})^2 x (\text{Inch})$ in equation (1.1). Equation (1.1) showed considerable scatter for low speed collisions when compared to the data used in Minorsky's work.

Vaughn (1978) extended Minorky's hypothesis to include the grounding of ships as well as collisions. He studied the behavior of a plate penetrated by a rigid wedge in order to estimate the damage to a ship's bottom plating if it were cut by a sharp rock or ice. The work done in penetrating the plating was decomposed into 2 parts: bending, similar to that done by Minorsky, and plate tearing. The plate tearing work was considered as a surface energy function per unit length for the fracture, or tearing apart, of the plate. Vaughn used experimental data from Akita & Kitamura (1972) to determine a proportionality constant for the fracture parameter. Vaughn (1980) conducted his own tests and modified his earlier results to fit the testing data. Defining ℓ as the distance of penetration into the plate, t as the plate thickness and θ is the wedge semi-angle, the resultant expression for energy is;

$$W = 5.5\,\ell\,t^{1.5} + 0.0044\,\ell^{2}\,t^{2}\tan\theta. \qquad (1.2)$$

Additional work was performed by Woisin (1982), Jones, Jouri & Birch (1984), Jones and Jouri (1987) and Lu and Calladine (1990) in order to determine the energy required to drive a rigid wedge into a steel plate.

Wierzbicki & Thomas (1993) developed a closed form solution for the initial wedge cutting force through a thin sheet. A single-term formula for indentation force and energy absorption was derived by relating the near tip and far field deformation events through a single geometric parameter, the instantaneous rolling radius of the flaps. Defining σ_0 as the flow stress, $\overline{\delta_t}$ as a dimensionless crack opening displacement parameter and μ as the coefficient of friction, the resulting expression for force is;

$$F = 3.28\,\sigma_0\,(\overline{\delta_t})^{0.2}\,\ell^{0.4}\,t^{1.6}\,\mu^{0.4}. \qquad (1.3)$$

The expression was considered valid over a range of wedge semi-angles $10^\circ \le \theta \le 30^\circ$ and friction coefficients $0.1 \le \mu \le 0.4$. Experimental work performed by Maxwell (1993) confirmed this work for wedge semi-angles of 20° and 30° and sought to achieve steady-state cutting results.

A solution for the steady-state wedge cutting force through thin plates was subsequently provided by Zheng & Wierzbicki (1994). Steady-state plate cutting experiments which support the theory were accomplished by Yahiaoui, Bracco, Little & Trauth (1994). Zheng and Wierzbicki's work also included a less rigorous formula which could provide a quick estimate of the wedge cutting force. Defining $M_0 = (\frac{2}{\sqrt{3}}\sigma_0)\frac{t^2}{4}$ as the plane-strain condition fully plastic bending

moment and B as the wedge half shoulder width, the simplified expression for force is;

$$F = M_0 \left(4 \frac{B}{t} \sin \theta \tan \theta + 3\pi\right)(1 + \mu \cot \theta) \qquad (1.4)$$

This expression was shown to provide reasonable accuracy compared with the more rigorous formulation during the testing conducted by Yahiaoui et al. (1994).

The plate cutting work has formed a basis for continued work in ship grounding resistance where the resistance is defined by the force required to push a wedge through the plate. The natural progression is to add structural elements to the plating and determine how this affects the cutting force. One approach is the concept of equivalent thickness, or smearing. Vaughn (1977) used this approach to estimate grounding damage to ships by created a smeared model of the ship. He smeared all of the supporting structural members shown in Figure 1-2 to a uniform shell thickness of t_{eq}. Defining V_{plate} and V_{supp} as the volume of damaged hull plating and supporting structure, and A as the area of damage, t_{eq} is found from;

$$At_{eq} = V_{plate} + V_{supp.} \qquad (1.5)$$

Wierzbicki et al., (1990) derived a modified expression which considered the height of the rock during the damage process. Defining subscript 1 as referring to longitudinal stiffener-plating combinations, subscript b as referring to a bulkhead with stiffener combination or web frame , Δ as the height of the rock penetration into the ship and l is the spacing between transverse frames, the overall equivalent thickness, t_{eq}, is determined as

$$t_{eq} = (t_{eq})_l + (t_{eq})_b \frac{\Delta}{l} \tag{1.6}$$

Defining A as the stiffener cross-sectional area, b as the associated width of plating and t as the thickness of the shell plating or bulkhead, the subscript t_{eq} values are determined using;

$$t_{eq} = t + \frac{A}{b}. \tag{1.7}$$

Figure 1-3 illustrates the referenced dimensions.

Paik (1993) has performed work which supports the equivalent thickness concept. He conducted an extensive study of the initiation phase of the cutting of a longitudinally stiffened steel plate by a rigid wedge. The study was performed by varying several factors, including plate thickness, plate aspect ratio, wedge tip angle/shape and stiffener properties. Plate thicknesses in the tests ranged from 3.4 to 7.0 mm. All of the stiffeners were of the flatbar type. From the test results, Paik was able to derive an empirical formula relating the absorbed energy to cutting length. Defining $C_{1.5}$ as a test constant which is dependent upon wedge angle, the expression is;

$$W = C_{1.5}\, \sigma_o\, t_{eq}^{1.5}\, l^{1.5}. \tag{1.8}$$

The expression compared within 10% to the previous work of Lu and Calladine and Wierzbicki and Thomas. Paik's work supported the idea of replacing a longitudinally stiffened plate with an unstiffened plate of equivalent thickness as in equation (1.7) for the initiation phase of the cutting process.

Paik also performed cutting tests on two specimens with a single transverse stiffener. From the tests, Paik observed that the peak cutting force for a transversely stiffened specimen was higher than for a longitudinal specimen with the same base plate thickness. However, the energy absorbed during the cutting process was of the same order of magnitude for both transversely and longitudinally stiffened specimens. Paik did not derive an expression for the energy absorbed while cutting the transversely stiffened plate.

Kuroiwa, Kawamoto & Yuhara (1992) performed a study on the damage of ship bottom structures due to grounding. The study included both experiments on 1/3 scale models and numerical simulations of full scale single and double bottom VLCC's (very large crude carriers). A total of two models were tested, with one of each bottom type. The experimental models were very similar to actual ship structure, including shell plating, longitudinal stiffeners, transverse frames and longitudinal bulkheads. For comparison, the test results were compared to a Minorsky method formula for raking force, where α is an empirical constant, A_i represents the damaged volume per unit length of a structural member and σ_Y is the yield strength of the material:

$$F = \alpha * \sum_i (\sigma_y * A_i) \qquad (1.9)$$

The predicted forces from equation (1.9) were about 170 and 150% of the experimentally observed force values, respectively when using $\alpha = 0.8$ (experimentally determined for general cargo ships). Kuroiwa et al., hypothesized that the difference was due to two factors. First, a VLCC's structure is different from that of a general cargo ship. A VLCC tends to have a larger spacing between stiffeners and transverse frames. The second factor was the sharpness of the rock model and the ease with which it could bend the

stiffeners. As a result, the experimental results were fit to a modified equation of the following form;

$$F = \alpha_p * \Sigma(\sigma_y * A)_p + \alpha_s * \Sigma(\sigma_y * A)_s, \quad (1.10)$$

where subscript p represents bottom plates while subscript s represents stiffeners. The empirical constants were found to be $\alpha_p = 0.8$ and $\alpha_s = 0.3$. The numerical simulation was performed using MSC/DYNA. The results showed force levels on the order of 20% greater than that observed in the experiments.

A critique of the previous work leads to several important observations. The unstiffened plate cutting work appears to be very valuable, especially considering that the longitudinal stiffeners can be smeared in using the equivalent thickness from equation (1.7). However, the work in this area does not include the effect of transverse structure (frames or bulkheads) commonly found in all types of ships. A comprehensive steady-state cutting model of a ship's hull must take this into account. In addition, there has been no consideration of the interaction between the transverse and longitudinal structure and its effect on cutting resistance.

While Paik's work on transverse stiffening is a useful first step, it is important to note the inaccuracies in the modeling. As shown in Figure 1-4, the transverse members on Paik's specimens were unrestrained at the ends. In a typical oil tanker, the end conditions for the transverse frames are typically clamped, since they are continuously welded to the longitudinal tank bulkheads. Finally, the work of Kuroiwa et al., points out a major dilemma to any study in this area, namely the problem of rock geometry. It is apparent that the geometry of the rock can have a significant effect on the separation mode and force levels observed.

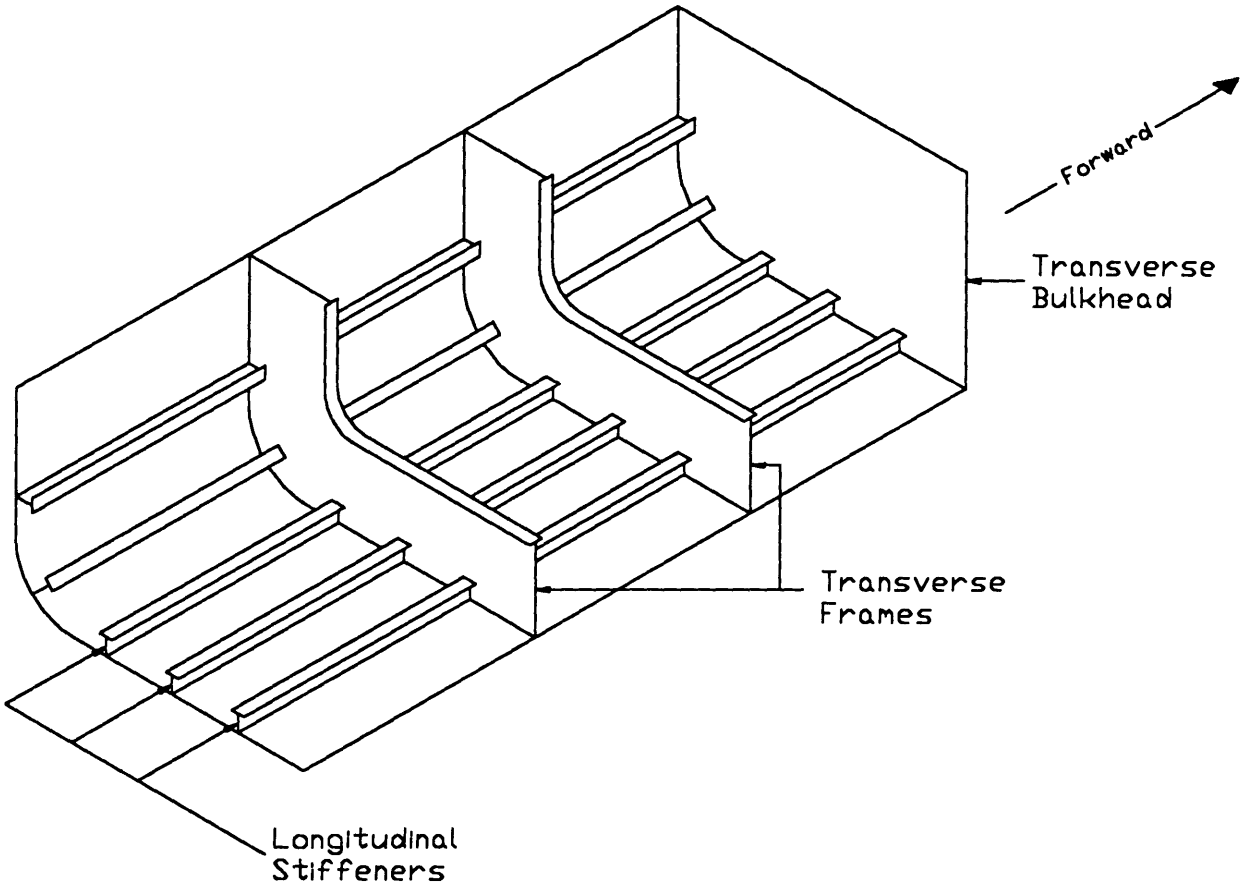

Figure 1-1. Major Ship Structural Members

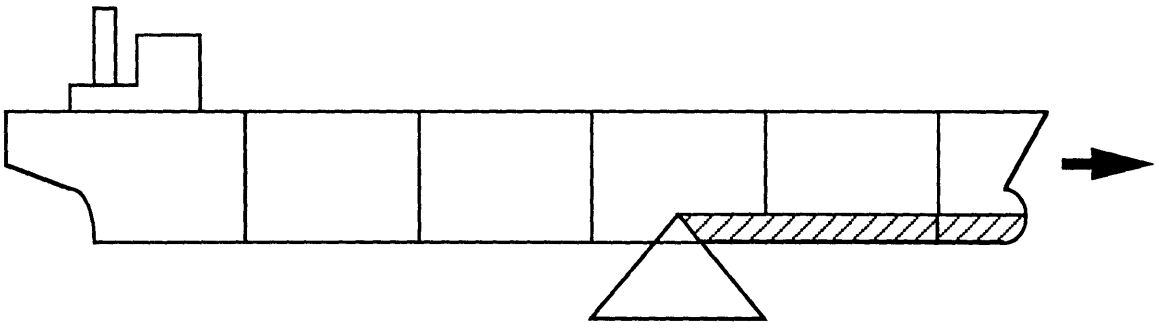

Figure 1-2. The Grounding Scenario

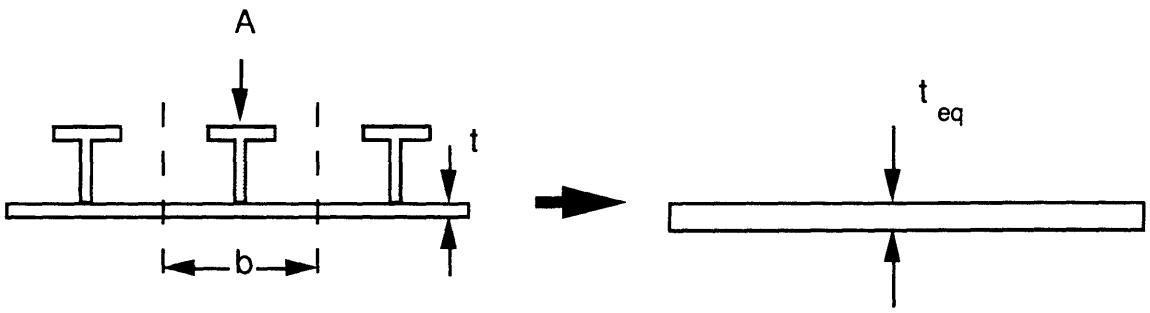

Figure 1-3. Equivalent Thickness Model

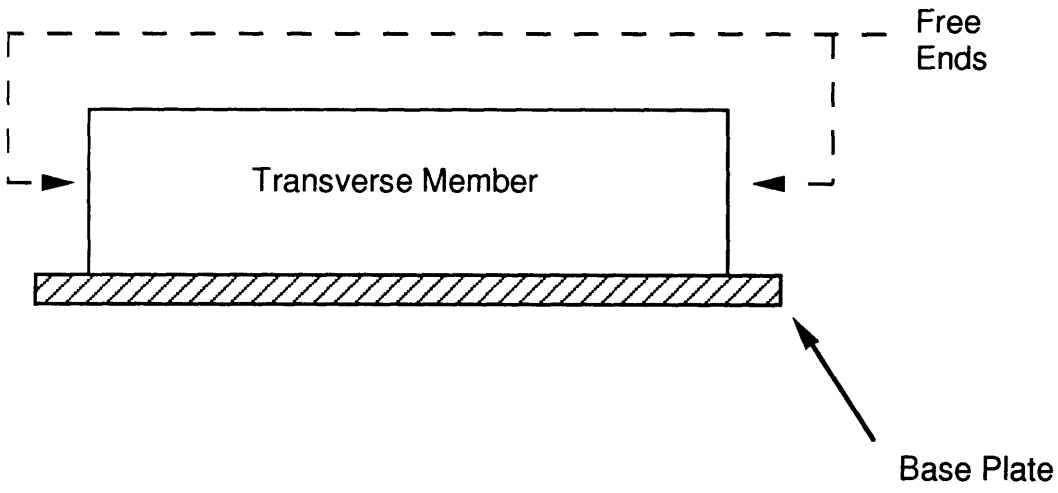

Figure 1-4. End View of Paik's Transverse Stiffened Specimen

2.0 - Experimental Procedures

2.1 Introduction

Chapter 1 described the current status of research into the steady-state grounding resistance of ships. It also identified the goal of this study as investigating the contribution of transverse members of ship structures, including transverse bulkheads and frames, to a ship's grounding resistance. This chapter will describe the methodology used to design experimental procedures as part of the investigation into the contribution of transverse members. Experiments were necessary in order to observe and understand the deformation mechanisms associated with transverse members.

2.2 Model Design Considerations

There are many factors to consider in the design of scaled models for testing. Since ship types and structural designs differ, a representative prototype must be selected. The existing test facilities must also be considered. The type, capacity and loading area of the testing machine place a limit on model size. For small scale testing, existing welding technology is a factor in determining the extent to which structural details can be modeled. Finally, any portion of the ship's structure modeled must include the appropriate boundary conditions.

2.2.1 Representative Ship Geometry

The first step in the process was to identify a representative ship structure to use as a prototype. This was important because the structure of a ship varies as a function of the type of service it performs. An oil tanker is different from a containership which is different from a dry bulk carrier in both service and form.

The structure is typically designed to optimize the cargo carrying capacity and to facilitate rapid loading and unloading. For this study, the type of ship selected was an oil tanker, since the hull rupture of this type of carrier could result in an oil spill. Given the volume of oil carried in a modern tanker, the effects of such a spill could be environmentally catastrophic, especially near the coast. From Yahiaoui et al., (1994) a 140,000 dwt VLCC was selected as having a structure typical of that currently used in the industry.

With a prototype ship selected, the question became one of which section of the ship to model. For simplicity, the model should represent an area where the structure is relatively uniform, such as the parallel midbody area which extends for over 40% of the length of the ship on a typical tanker. Figure 2-1 shows part of the midship section of the prototype VLCC which is representative of the parallel midbody section. The beam of the VLCC is 43.2 meters. Figure 2-1 illustrates both the complexity and variety of structure across the beam of the ship. Another important issue is which portion of the VLCC midship section to model. For simplicity, the central portion of the ship was modeled.

2.2.2 Existing Facilities

It was desired to maximize the use of the existing laboratory facilities during the experimentation phase for simplicity and low cost. The main testing machine was 20,000 lb Instron located in the Remergence Laboratory of the Civil Engineering Department at MIT. A detailed description of the Instron machine, including operating instructions, is included in Appendix A. During his experimental work, Maxwell (1993) designed a testing fixture for his plate cutting experiments on the 20,000 lb Instron machine. Maxwell's testing frame was designed to accommodate several factors, including the ability to withstand

forces generated by cutting through plates up to 2 mm thick. While the use of the existing machine and frame was convenient, it did introduce constraints into the model design. The length and width of the specimen were limited to the frame dimensions and the maximum equivalent plate thickness was limited to 2 mm.

2.2.3 Welding Technology

Another consideration in the specimen design was the type of welding process to be used to provide the mechanical connection between longitudinals, transverses and the base plate of the model. The test frame was designed for a maximum equivalent sheet thickness of 2 mm. Available sheet sizes in this range were 0.749, 1.130 and 1.829 mm. Since the models were to contain more than just plating, the thickness of the base plate could not exceed 1.130 mm. As discussed by Yahiaoui et al., (1994), the use of conventional welding techniques on sheet metal this thickness produces unacceptable levels of distortion over the length of weld required. Electron beam welding (EBW) was selected and used on previous models with good success. The welds were strong and free of distortion.

EBW introduces some constraints. First, the minimum practical weldable thickness was on the order of 0.5 mm. EBW can be used to weld thin foil-like material, but thicknesses of that order are not practical for testing. Second, due to the nature of EBW, only certain types of joints can be fabricated. Figure 2-2 illustrates two methods used in order to weld a longitudinal or transverse member to a plate. The first, EBW essentially fuses the stiffener to the base plate with the EBW gun on the opposite side of the plate. This is different from the conventional method, using rod or wire, which deposits filler metal along both sides of the joint for holding strength. EBW is done in a vacuum chamber,

giving the operator a limited view of the specimen. The combination of these factors effectively limits the complexity of the welded structure.

2.2.4 Boundary Conditions

A final consideration was the design of effective boundary conditions for the specimen. For the prototype VLCC, the transverse frames and bulkheads intersect with longitudinal bulkheads and the skin of the ship. This is shown in Figure 2-1 for a transverse frame. These intersections result in relatively fixed boundary conditions for the transverse member. Thus, when designing the specimens, it was not sufficient to leave the ends of the transverse unsupported. Several prototype designs for brackets to fix the end conditions were developed, but rejected due to complexity and manufacturing expense. Instead, it was decided to use longitudinal members to provide the necessary boundary conditions.

2.3 Scaled Specimen Details

Two types of scaled specimens were designed. The first, a plate with a single transverse member, was designed in order to gain insight into the deformation process as the wedge cuts through the plate. A more complicated second generation specimen was also designed in order to observe and understand the interaction of longitudinal stiffeners with the cutting process. The first sample is referred to as a transverse specimen. The second, which includes longitudinal stiffeners, is referred to as an orthogonally stiffened specimen.

2.3.1 Selection of Scaling Factor

The goals in scaling were to construct a specimen which was geometrically similar to the prototype, could be tested in the existing facilities and could be

fabricated using existing technology. In order to facilitate this, a target scaling ratio of 1:16 was selected. This ratio was driven by the considerations from Section 2.2, as follows. The use of Maxwell's frame limited the gross size of the specimen to 12.25 inches in width by 20 inches in length. Steel sheet thickness were bounded from 0.5 mm (practicality) to 2 mm (frame strength). Available sizes of steel sheet in this range were 0.749, 1.130 and 1.829 mm. Finally, since this work was a part of the overall effort being conducted by the Safe Tanker Program, it was desired to use a scale factor similar to the longitudinally stiffened specimens used by Bracco (1994). This combination of constraints drove the target scale ratio to 1:16.

2.3.2 Level of Detail of Specimen

A typical ship structure is very complex and contains numerous details. Figure 2-1 illustrates this complexity. Numerous stiffening members are present on the transverse frames to prevent buckling. Connections between major structural members are reinforced by brackets to provide additional stiffness. The transverse and longitudinal webs are capped by a flanges, forming I-beam shapes.

Including the correct level of detail in the model is an important issue. Although many items, such as the brackets, are primarily for local effects such as buckling, they still contribute to the overall strength of the hull. The greater volume of material present will increase grounding resistance. However, for the target scale ratio of the specimen, many of these details were not practical because of size considerations. A minimum practical weldable thickness of 0.5 mm was already established.

The issue was resolved by the overall goal of the testing. For these tests, the goal was to understand the contribution of a typical transverse member to

steady-state grounding resistance. With this goal in mind, along with the chosen scale factor, it was neither desirable nor practical to include a high level of detail. As a result, two types of specimens were built. The first included only a transverse web frame without local stiffening or the flange. A second type of specimen added longitudinal stiffeners. It was assumed the height of the rock is such that it never penetrates above the top of the transverse member. If greater specimen detail is desired, the scale ratio should be changed from 1:16 to 1:4 or 1:3.

2.3.3 Transverse Specimen Geometry

With all of the previous considerations, two types of transverse specimens were designed. For clarity during the discussion, the transverse member will be referred to as the transverse frame and the longitudinal support members as the longitudinal supports. The transverse member could be either a frame or bulkhead; the terminology is for convenience. The variable distinguishing the two types of transversely stiffened specimens was the spacing between the longitudinal supports at the ends of the transverse frame to provide a fixed boundary condition. For the first type of specimen, the longitudinal support spacing, S, was equal to the scaled longitudinal stiffener spacing of the prototype VLCC (S=2.1"). An isometric sketch of this narrow specimen is shown in Figure 2-3. A summary of key dimensions and actual scale ratios is included in Table 2-1.

Table 2-1. Transversely Stiffened Specimen Geometry

Member	Actual Dimension	Scaled Dimension	Actual Ratio
Base Plate	0.866"	0.044"	1:19.68
Transverse Frame Depth	98.425"	6.125"	1:16.07
Transverse Web Thickness	0.728"	0.044"	1:16.55
Longitudinal Stiffener Spacing	33.45"	2.1"	1:15.93

All of the members are at the desired scale ratio except for the base plate. Accurately scaling the 24 m distance between the longitudinal bulkheads of the prototype VLCC and using this dimension for the longitudinal support spacing would have resulted in a specimen several feet wide. Since the distance between longitudinal supports was limited by the maximum sample width of 12.25 inches, it was decided that a longitudinal support of the same thickness and height as the transverse frame would provide the desired boundary conditions.

A second type of specimen was designed with a wider spacing between the longitudinal supports. The spacing was set to be three times the scaled spacing between longitudinal stiffeners of the prototype VLCC (S=6.3"). An isometric sketch of this specimen is shown in Figure 2-4. Detailed construction drawings for both types of samples are included in Appendix B.

2.3.4 Orthogonally Stiffened Specimen Geometry

All of the considerations which applied to the transversely stiffened specimen design also applied to the orthogonal specimens. Based on the previously determined scale factor, the specimen was designed to include four longitudinal stiffeners and one transverse member. As before, even though the longitudinal stiffeners on the prototype VLCC have a flange, they were not included on the model because of fabrication difficulties. Figure 2-5 shows an isometric view of the sample. Table 2-2 summarizes the key dimensions and actual scale ratios of the specimen.

Table 2-2. Orthogonally Stiffened Specimen Geometry

Member	Actual Dimension	Scaled Dimension	Actual Ratio
Base Plate	0.866"	0.044"	1:19.68
Transverse Frame Depth	98.425"	6.125"	1:16.07
Transverse Web Thickness	0.728"	0.044"	1:16.55
Longitudinal Stiffener Spacing	33.45"	2.1"	1:15.93
Longitudinal Stiffener Web Depth	20.669"	1.41"	1:14.66
Longitudinal Stiffener Web Thickness	0.453"	0.030"	1:15.1

A key difference for this specimen was that the longitudinal stiffeners were designed as continuous members. Slots were cut in the transverse member just large enough for the longitudinal stiffeners to slide through. The longitudinal stiffeners, supports and transverse frame were electron beam welded to the base plate. The longitudinal stiffeners were then welded to the

transverse frame using the tungsten inert gas (TIG) arc welding process. There were no visible gaps or excessive distortion due to the small length of weld.

2.4 Wedge Selection

The selection of the wedge to be used in the testing was an important consideration in the experimental design. There was little information in the literature or in ship grounding records held by various agencies (U.S. Coast Guard, Det norske Veritas, etc.) which would help determine the geometry of a typical rock a ship might encounter in a grounding situation. Given the lack of such guidance, it was difficult to substantiate any wedge design as being representative of a 'real world' situation. A second consideration was the desire to avoid a wedge with a sharp tip. This type of wedge gives the appearance of mechanical cutting, similar to a machine tool. A narrow and a wide wedge were designed and fabricated.

2.4.1 Wedge Design Parameters

Relevant parameters in the wedge design, as suggested by Wierzbicki et al., (1990), include the sloping angle, α, the spreading angle, β, and the rock height above the ship's bottom, Δ_R. Figure 2-6 illustrates these parameters with respect to a ship. Situations with α less than 15° were assumed to be a part of the so-called soft grounding being studied by a research team in Denmark and were thus not considered. Also, in order to fit the wedge between the top of the specimen and the testing frame, α needed to be greater than approximately 60°. Figure A-1 of Appendix A illustrates the clearance. Smaller values of α create a greater amount of lift, or out-of-plane force during testing. This research was concerned with the in-plane cutting forces. Thus, α was selected to be 65°.

A second range of validity concerns Δ_R. Card (1975) studied 30 oil tanker bottom damage incidents from 1969 to 1973 and concluded that a double bottom height of only 2 m would have prevented oil outflow in 29 of 30 cases. In addition, Card's study indicated the vertical extent of damage was not related to tanker size. Thus, for the wedge design, it was assumed that the top of the rock never extends above the top of the transverse web frame.

Finally, designing a wedge using a value of β as shown in Figure 2-6 would have resulted in a sharp cutting tip. This effect was not desired as discussed in Section 2.4 Thus, β was not included as a design parameter.

2.4.2 Wide Wedge Geometry

The first wedge was designed to be wider than the distance between two adjacent longitudinal stiffeners so that the interaction would be observed. To ensure this, the total wedge width, 2B, was selected to be 3". A prismoid type cutting surface was designed into the cutting surface. Compound angles were machined into a block of steel in order to achieve this shape. Figure 2-7 is a dimensioned isometric view of this wedge. Note that the wedge is designed to cut 2 specimens simultaneously and is thus symmetric. The reason is explained in Section 2.5.2. Detailed construction drawings are included in Appendix B. The wedge was machined from a block of cold finished steel and surface hardened to a depth of 0.030" using a cyanide solution at 1650°F. The hardening was used to prevent the specimens from cutting a grove into the wedge during testing.

2.4.3 Narrow Wedge Geometry

The narrow wedge was designed and constructed in a manner similar to the wide wedge. A wedge width of 2B = 0.5" was selected. The main difference

was that due to the 0.5" width, it was not feasible to machine a prismoid surface of the leading edge. Instead, a radiused surface was used. This type of surface was considered blunt enough to avoid mechanical-type cutting. Figure 2-8 is a dimensioned isometric view of this wedge. Detailed construction drawings are included in Appendix B. This wedge was also surface hardened.

2.5 Testing Apparatus

The experiments were conducted in the Remergence Laboratory of the Department of Civil Engineering at MIT on a 20,000 lb Instron machine. As indicated in Section 2.2, a description of the machine and operating instructions is included in Appendix A. Although both the machine and testing frame were already available, additional modifications were required in order to perform the tests. This section will discuss those changes to the wedge holder and frame.

2.5.1 Wedge Holder Modifications

As discussed by Yahiaoui et al., (1994), while cutting double hull specimens in the testing apparatus, it was apparent that a large moment was being transmitted to the load cell from the wedge via the adapter. The specimen had to be offset because the adapter could not fit through the top of the frame. There was concern that the moment could be large enough to damage the load cell. In order to correct the problem, the adapter was modified. Figure 2-9 shows the old and new configurations.

Two types of adapters were fabricated. The first, shown in Figure 2-10, held the large wedge and is the same as that used by Yahiaoui et al., (1994) and Bracco (1994). A second adapter was needed to hold the narrow wedge. The narrow wedge holder from Yahiaoui et al., (1994) was modified so that the

wedge holder would not contact either the side supports or the transverse frame. This holder is shown in Figure 2-11.

2.5.2 Frame Modifications

During planning of the tests, it was apparent that due to the geometry of the specimens, it would be necessary to test two specimens simultaneously. This would equilibrate the out-of-plane cutting forces on the load cell developed by the wedge sloping angle. For the double hull specimen testing, Yahiaoui et al., (1994) had designed and fabricated a spacer which was inserted in the testing frame. The same spacer was used for these tests. It provided a constant separation between the supports for the two specimens. Figure 2-12 illustrates the testing frame with spacer. Note that for clarity the longitudinal supports are not shown. A drawback of this testing arrangement is that is not possible to measure the lift, or out-of-plane force.

A second modification was required to reinforce the longitudinal supports used to provide the boundary conditions. During testing of the longitudinally stiffened specimens, Yahiaoui et. al., (1994) noticed a significant back and forth pivoting of the longitudinal members as the wedge passed by. In order to avoid this, brackets were designed to reinforce the longitudinal supports and help maintain them as a rigid boundary. Figure 2-13 illustrates the placement of the brackets. Appendix B contains detailed construction drawings for the brackets.

2.6 Electron Beam Weld Strength

In some of the tests on UDSH and longitudinally stiffened plate models conducted by Yahiaoui et al., (1994) and Bracco (1994), it was observed that the welds did not fail even when subjected to a severe degree of bending. As a

result, there was some concern that EBW produces welds which are too strong as compared to full scale ship welds.

McClintock (1994) has suggested several failure modes for welds in ship structure. The modes are shown in Figure 2-14. McClintock has devised a test, the Lazy-T, to investigate the web folding mode of failure. In order to quantify the strength of the electron beam welds used in the construction of these specimens, Lazy-T tests were performed using the 0.029" thick steel sheet. The details and results of these tests are included in Appendix C.

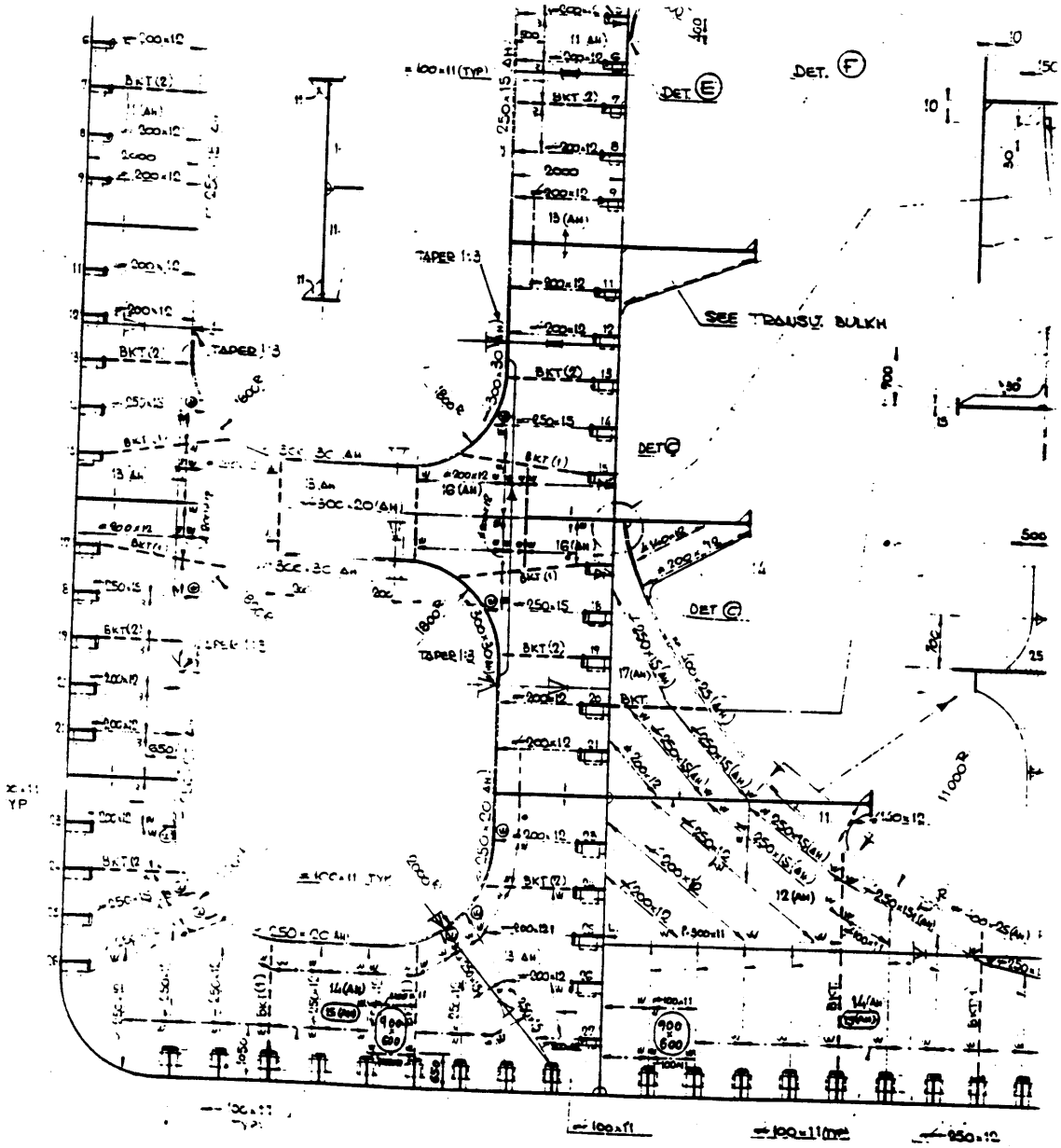

Figure 2-1. VLCC Midship Section

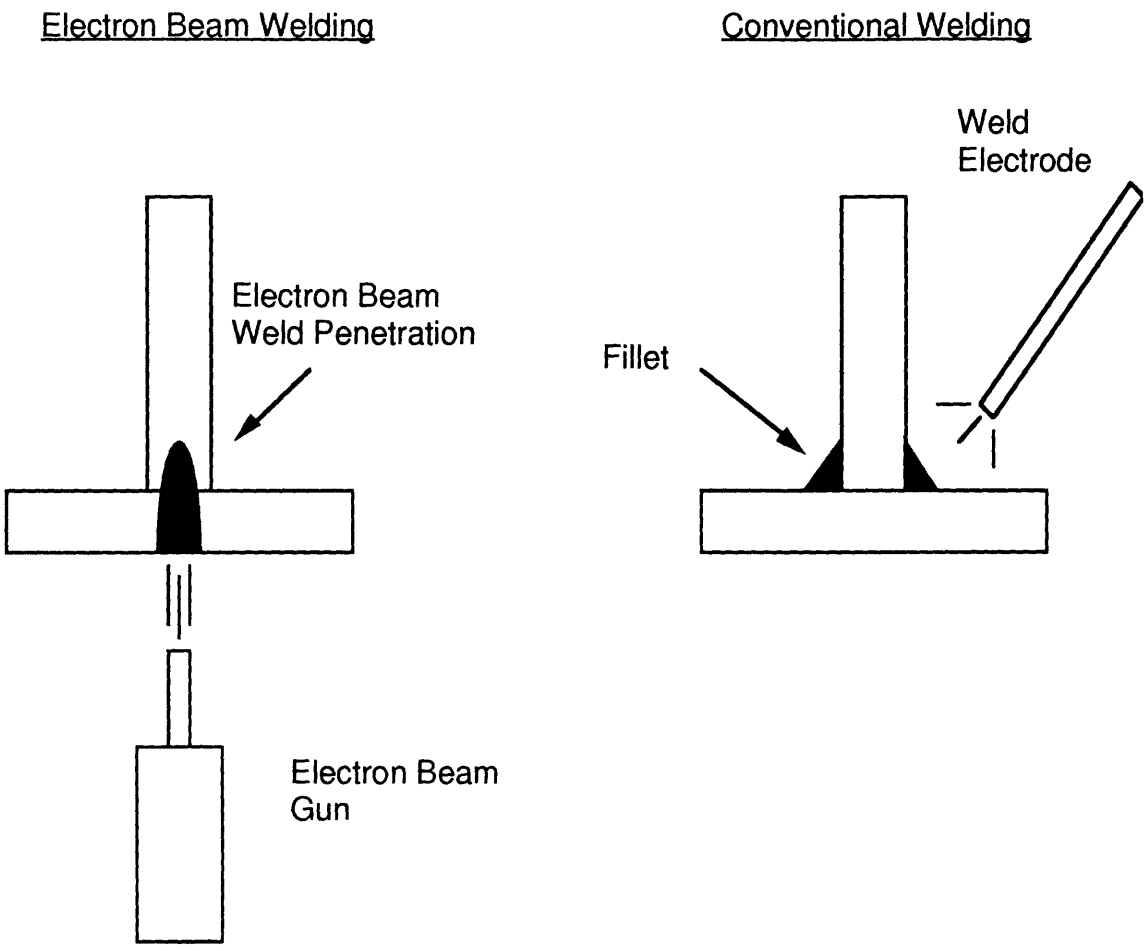

Figure 2-2. Welding Technique Comparison

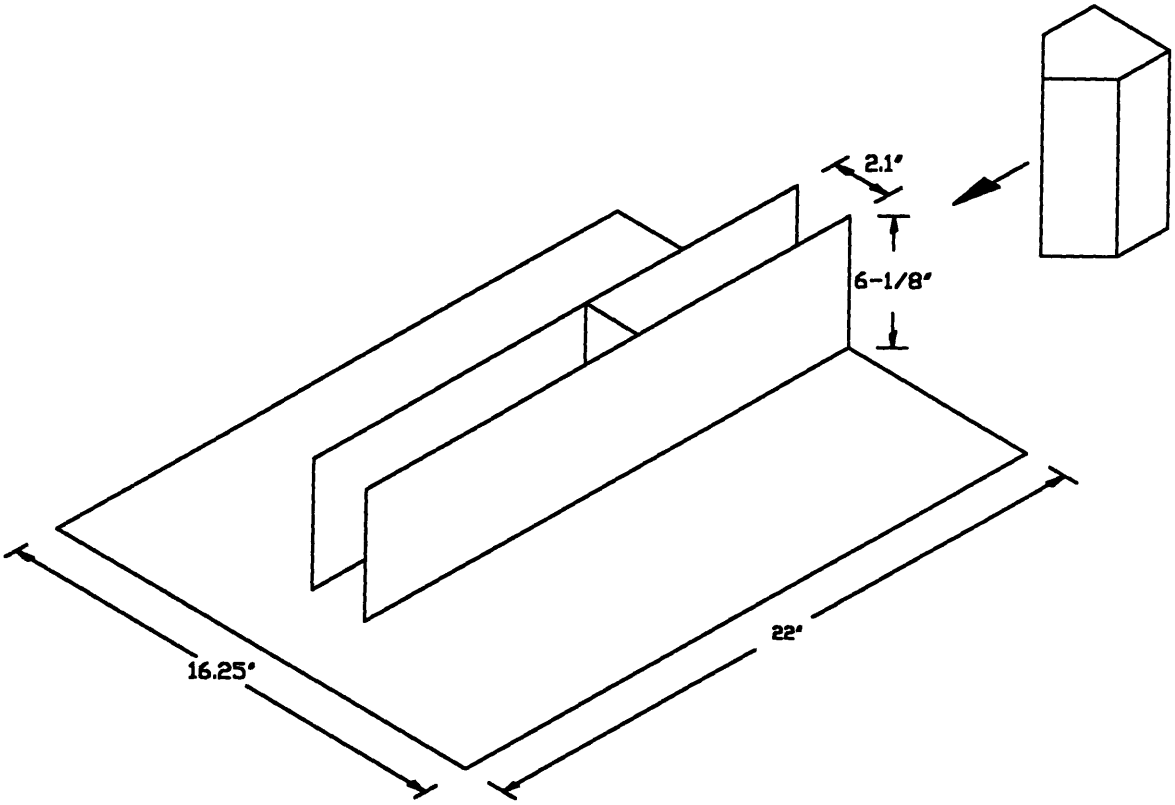

Figure 2-3. Isometric Sketch of Narrow Transverse Specimen

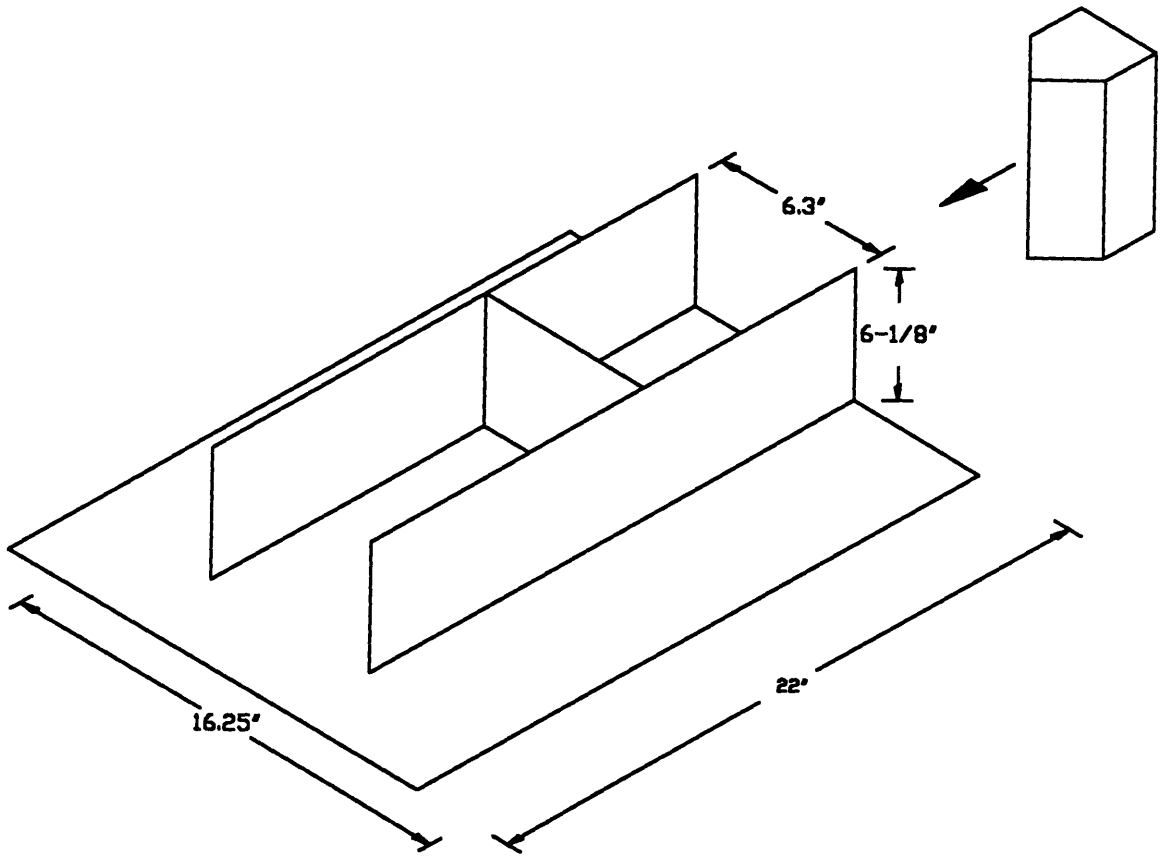

Figure 2-4. Isometric Sketch of Wide Transverse Specimen

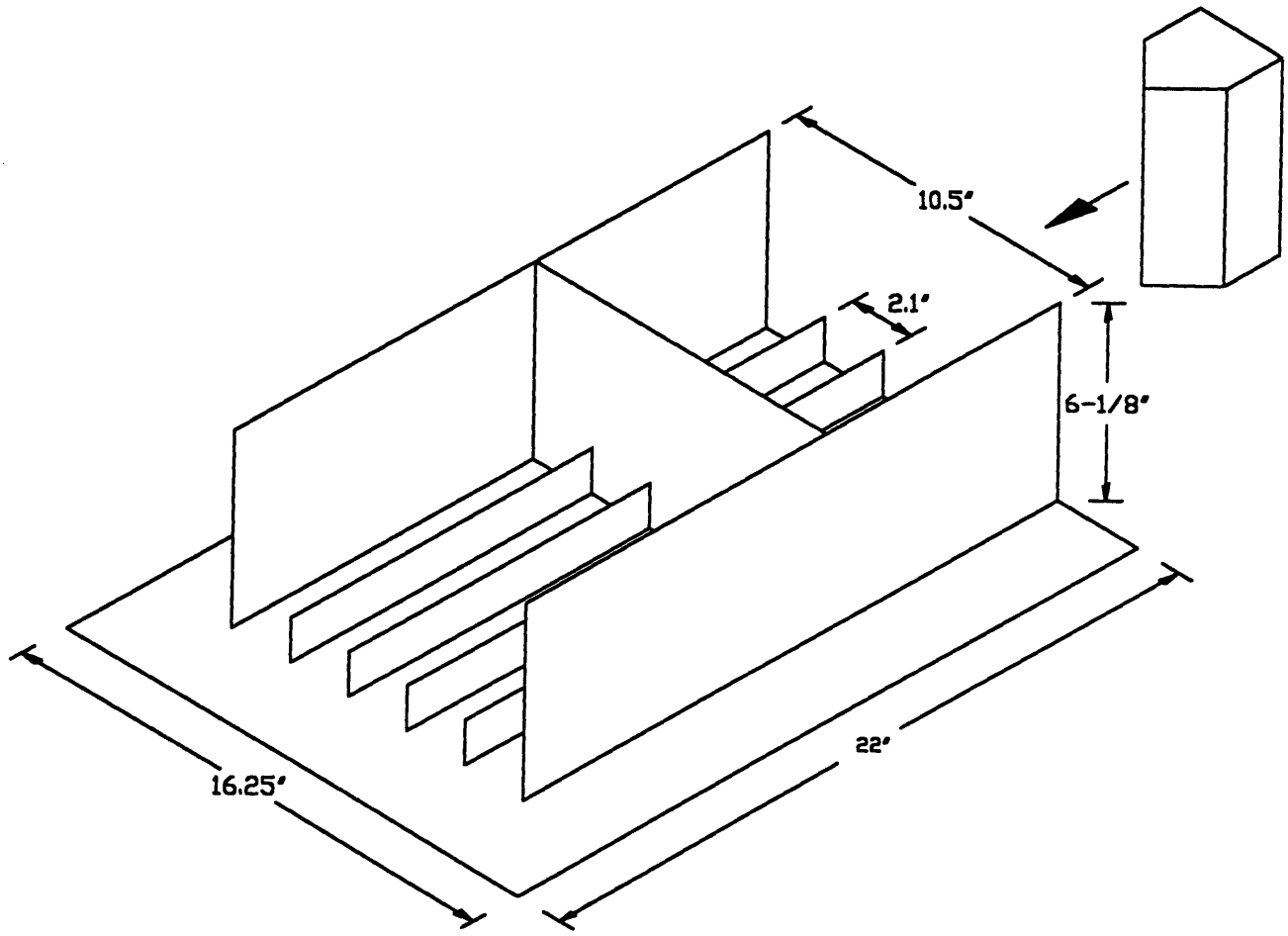

Figure 2-5. Isometric Sketch of Orthogonally Stiffened Specimen

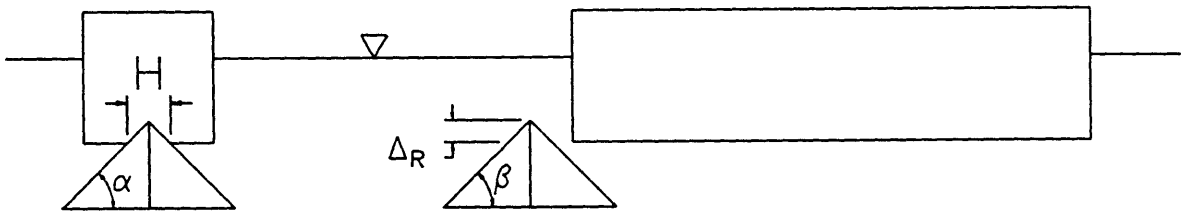

Figure 2-6. Rock Geometry Parameters

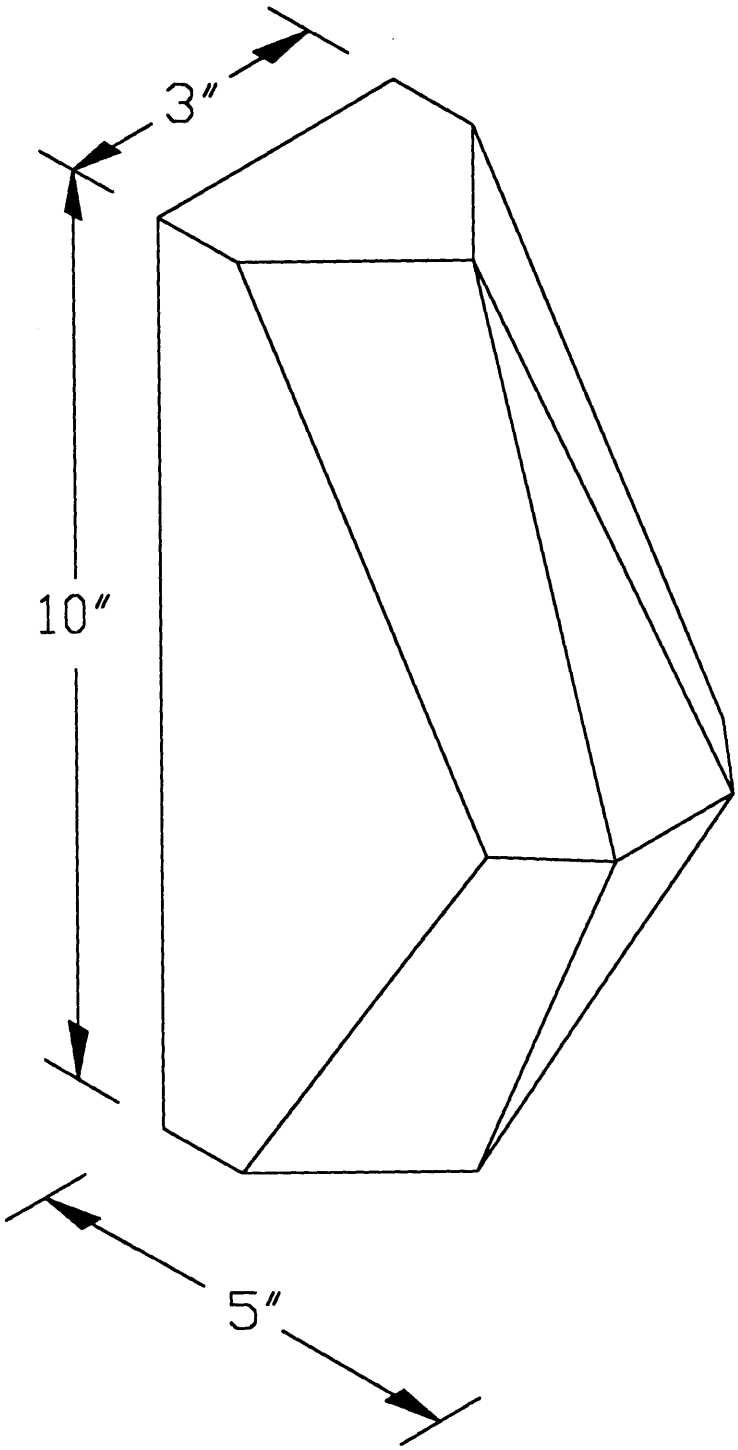

Figure 2-7. Isometric Sketch of Wide Wedge

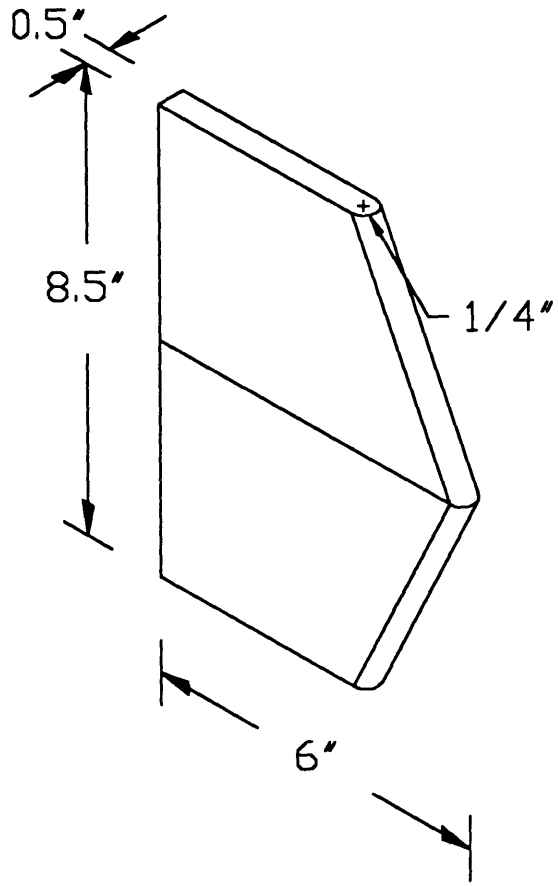

Figure 2-8. Isometric Sketch of Narrow Wedge

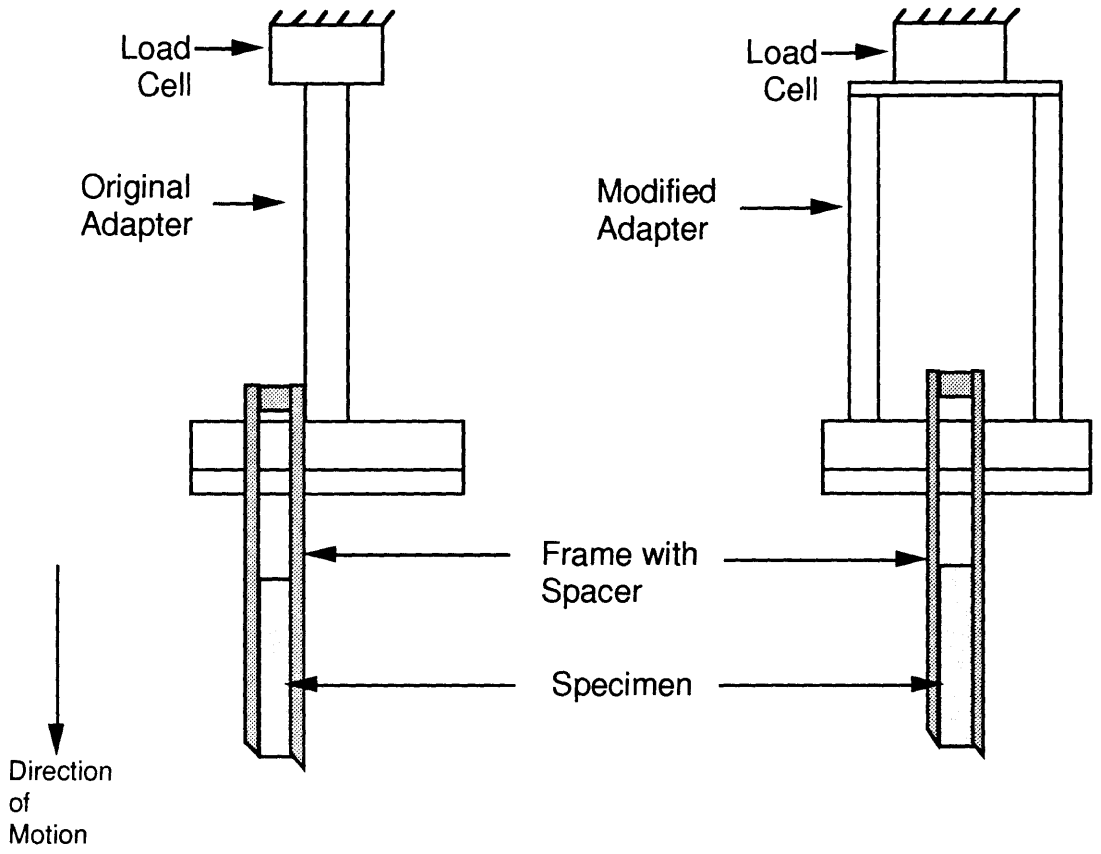

Figure 2-9. Wedge Adapter Modifications
(Yahiaoui et al. (1994))

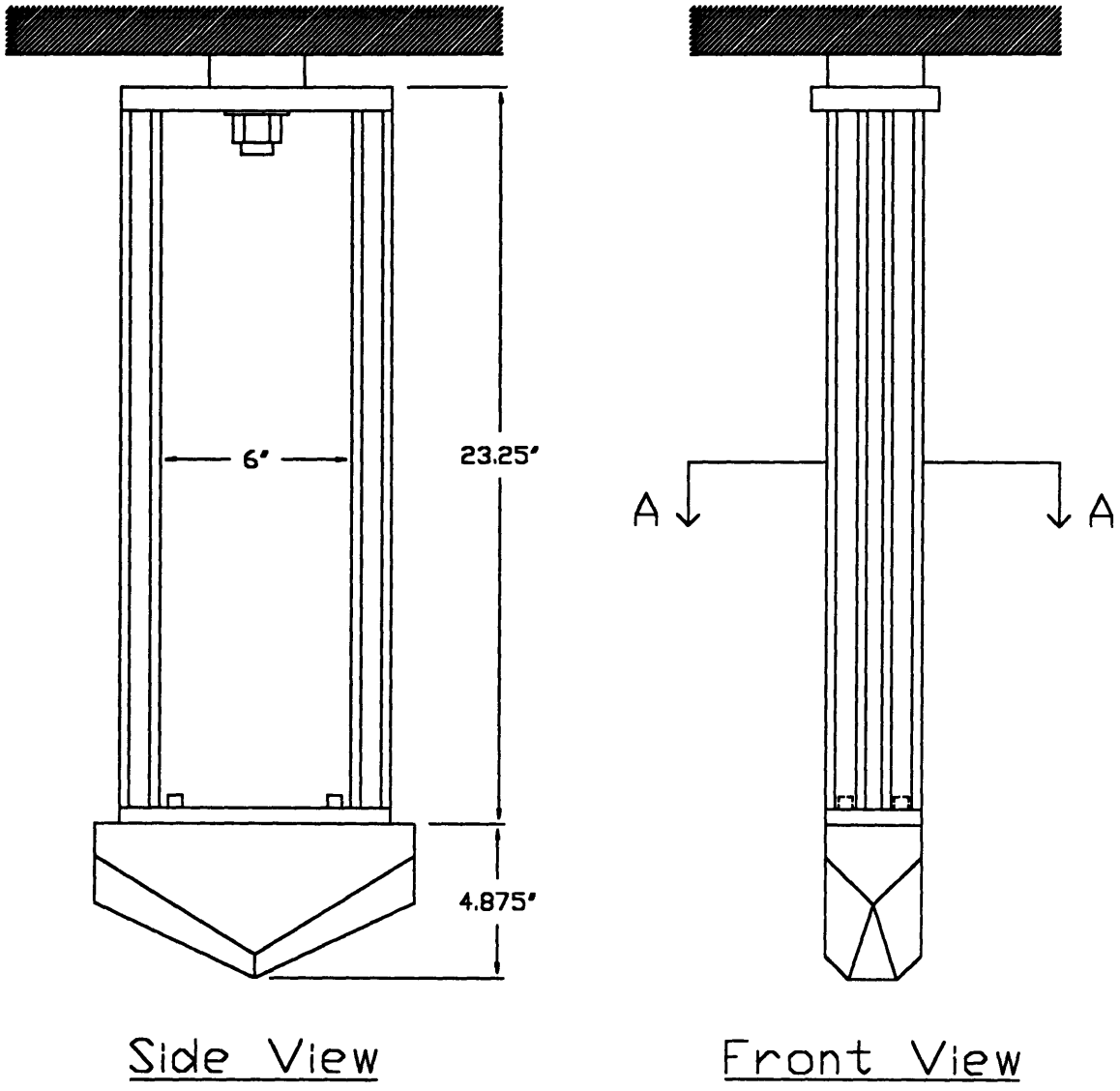

Figure 2-10. Wide Wedge Holder

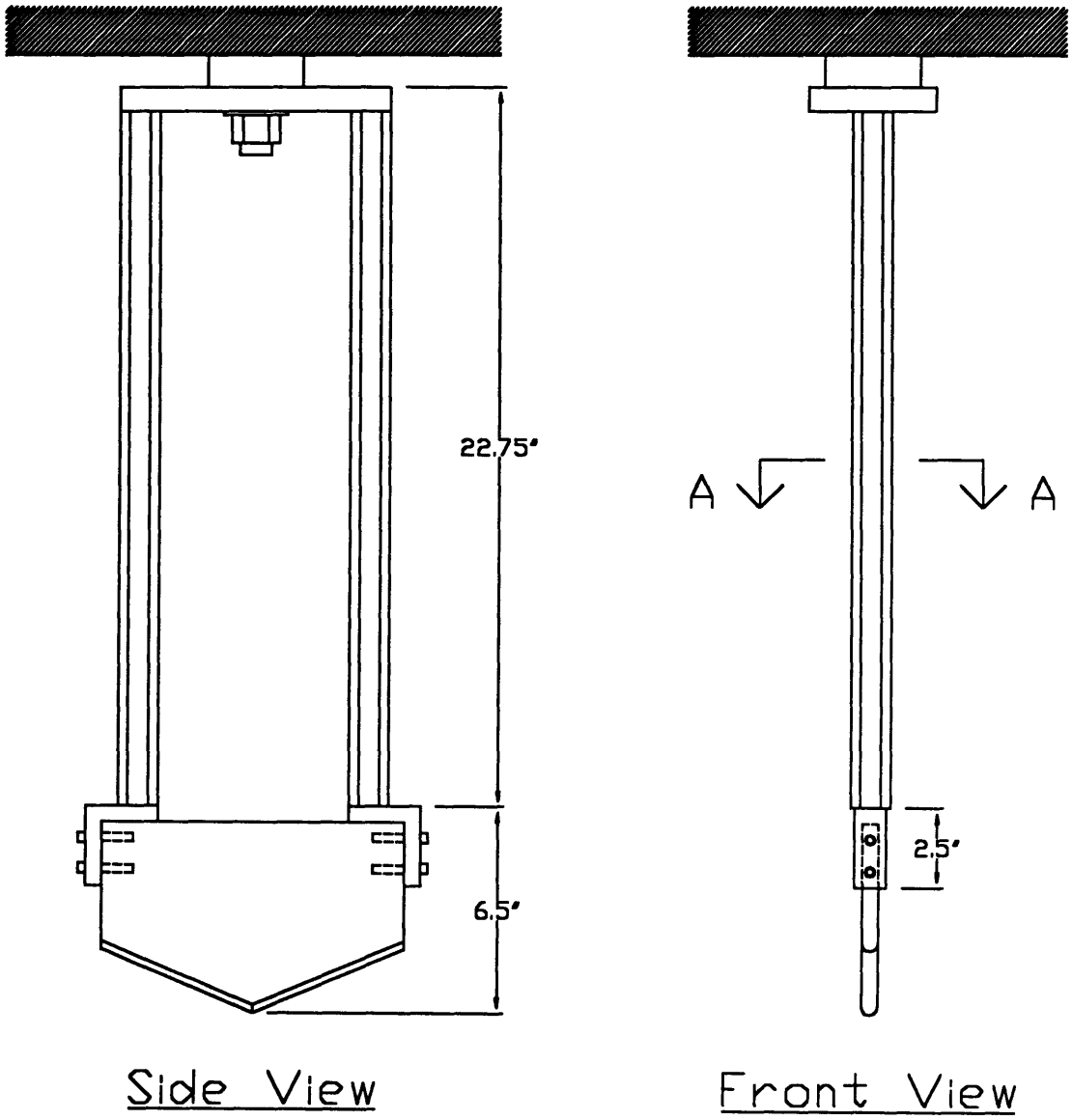

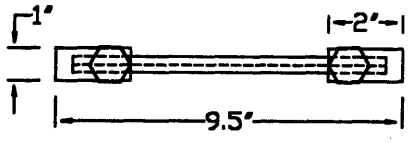

Figure 2-11. Narrow Wedge Holder

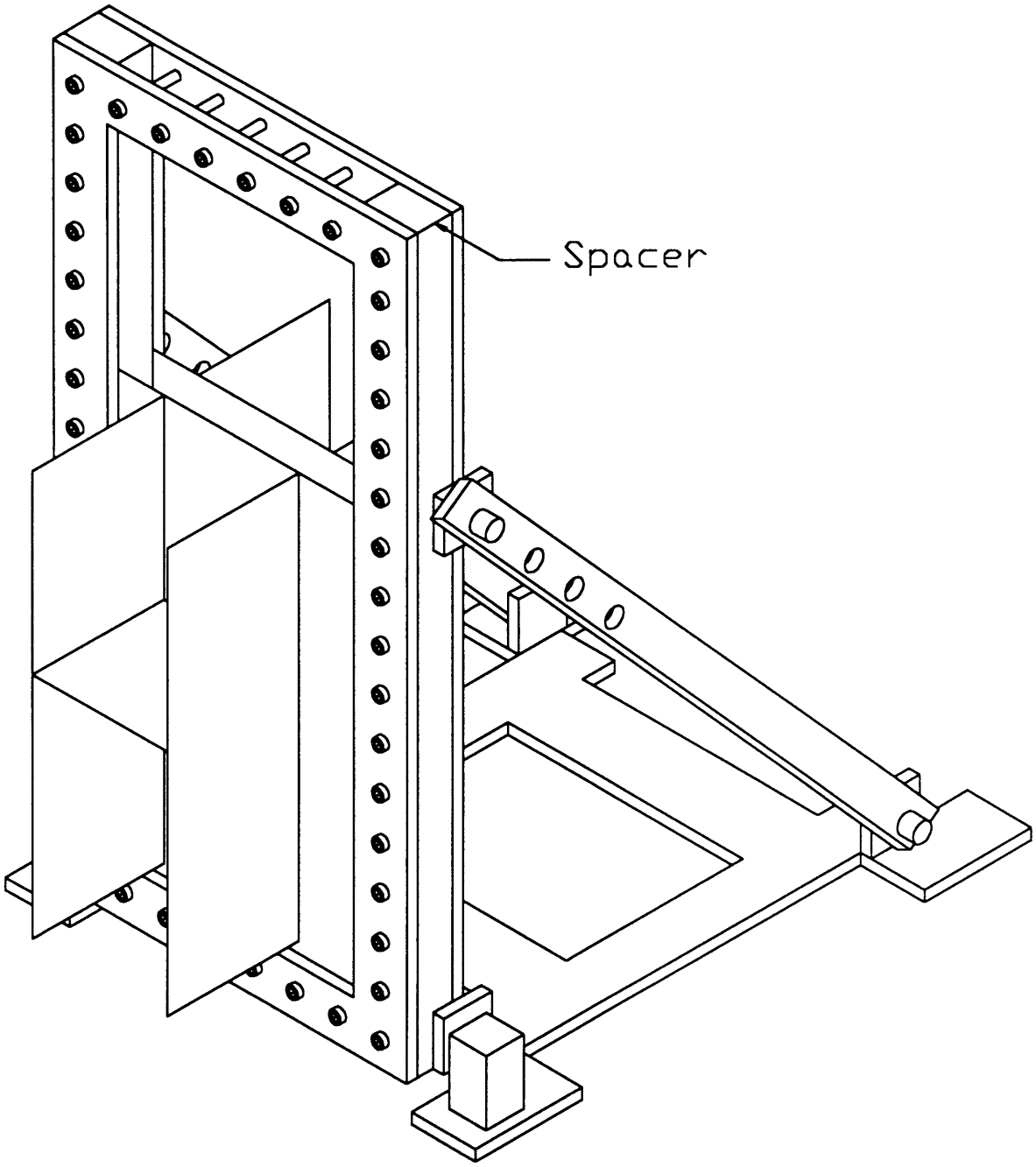

Figure 2-12. Test Frame with Spacer

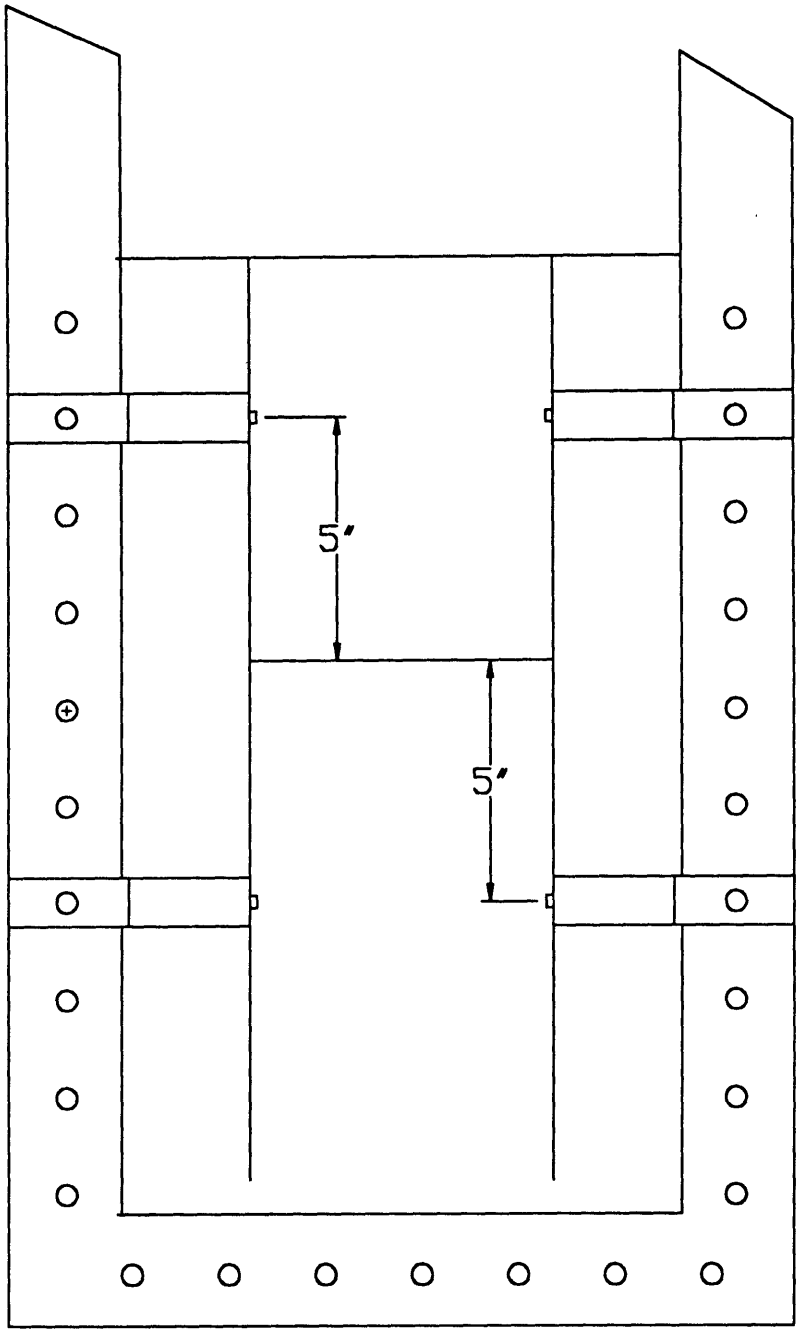

Figure 2-13. Longitudinal Support Bracket Placement

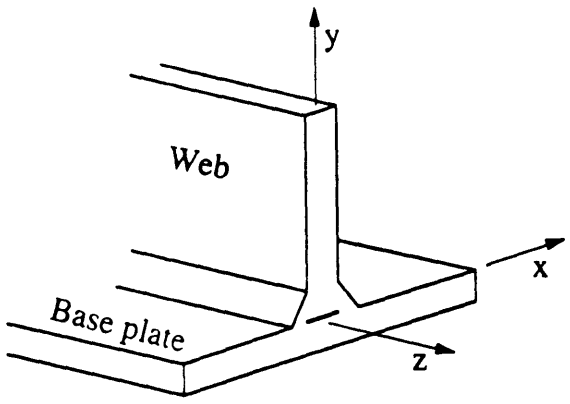

Coordinate axes for a T-joint

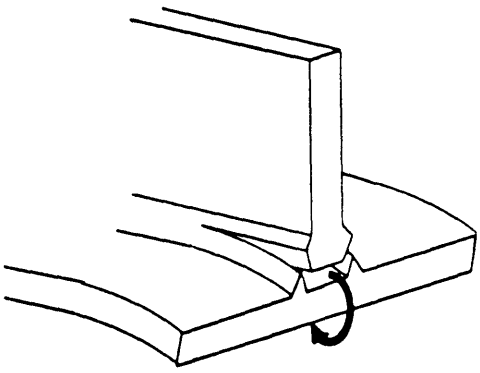

(a) Tearing

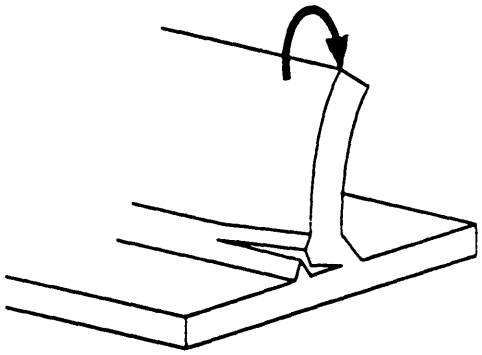

(b) Web folding

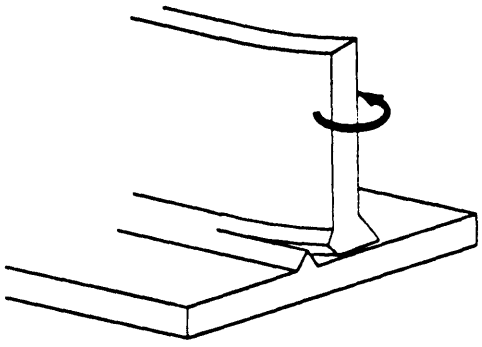

(c) Web bending

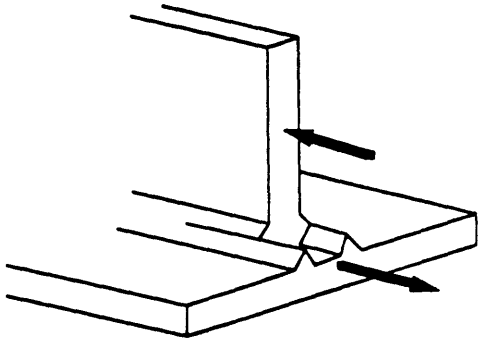

(d) Longitudinal shearing

Figure 2-14. Weld Failure Modes
(McClintock (1994))

3.0 - Experimental Results

This section provides the detailed results of the four sets of experiments conducted on the transversely stiffened specimens. Two tests were conducted on the narrow transversely stiffened specimens (S = 2.1 inches) using the narrow wedge (B = 0.25 inches), a B/S ratio of 0.119. Two additional tests were conducted on the wide transversely stiffened specimens (S = 6.3 inches) using the wide wedge (B = 1.5 inches), a B/S ratio of 0.238. All tested specimens were precut by a distance of approximately 12.7 mm. Selected photographs of the damaged specimens are included after force-displacement plots to visually indicate the deformation. The orthogonally stiffened specimens were not tested due to fabrication delays.

Note that an experiment consisted of testing two specimens in parallel as discussed in Section 2.5.2. The total force for both specimens is plotted versus displacement. As such, the force-displacement plots represent an averaging effect. The discussion of deformation and fracture modes focuses on one of the specimens, after which any differences of behavior of the mirrored specimen are noted.

3.1 Narrow Specimen Test Results (B/S = 0.119)

Two sets of experiments were performed on this type of specimen. There was a slight difference in testing procedure. During test #2, the wedge progress was stopped at several points to facilitate observation and measurement of the damage, but the results from both tests were similar.

3.1.1 Test #1 - Narrow Specimen

This discussion follows the force-displacement curve illustrated in Figure 3-1. The discussion is keyed to the points listed on the graph. Points marked by the letters D, F, I, J, K, and N are reserved for discussion of the wide specimen tests.

1. As the wedge was pushed down into the precut, the force started to rise rapidly from A to B. Two cracks were initiated at the corners of the precut and began propagating ahead of the wedge. They quickly converged to a single crack.

2. Prior to reaching B, the entire wedge face was engaged with the plate. The flaps from the precut began to come in contact with the parallel faces of the wedge. Once contact began, the force leveled off as indicated from B to C.

3. At C, the flaps ceased to contact the wedge, as indicated by the slight drop in force from C to E.

4. From E to G, the wedge was pushed through the plate in an apparent steady-state cutting mode. A slight rise in the overall force was evident over this range.

5. When the wedge was approximately 10-15 mm away from the transverse frame (G), the force rose sharply. The base plate began to fold as the wedge contacted it, coinciding with the slight drop in force (H).

6. The wedge continued to press into the transverse frame, causing the force to continue to rise sharply. At the peak value of force (L), two cracks appeared at the edges of the wedge and the force dropped suddenly. The wedge continued to advance, folding the material ahead of it, with cracks diverging from the side.

7. At M, the weld connecting the transverse frame to the base plate on one side of the cut broke off cleanly, resulting in a sharp drop in force. The same weld on the other side of the cut held fast throughout the test. From M, material began to fold back and forth ahead of the wedge in the so-called concertina mode. The force would rise and fall as material was folded over, but the overall trend of the force was to decrease with the length of cut. Concurrent with the material folding, the transverse frame continued to tear away from the longitudinal support along the weld up to the top of the joint. It was also pushed out of the way of the advancing wedge.

8. At O, the effect of the transverse frame had diminished such that the process was essentially pure concertina folding. Approximately 7/8 of the transverse frame was torn from the longitudinal support along the weld joint on both sides.

The mirrored specimen deformed and fractured somewhat differently. Both sides of the transverse frame remained attached to the base plate throughout the experiment. The transverse frame was also torn from the longitudinal support, but only over 3/4 of the weld joint length. Finally, the mirrored specimen transitioned back to a central cutting mode when the length of cut was approximately 250 mm.

Two photographs from Test #1 are presented in Figure 3-2. The photographs clearly show that this specimen had transitioned back to steady-state cutting at the end of the test. As shown, the transverse frame was torn along one side and folded out of the way of the wedge.

3.1.2 Test #2 - Narrow Specimen

The results of this experiment from A to G was almost identical to that of Test #1.

1. As shown in Figure 3-3, there was an initial increase in force (A-B) as the cutting process began, followed by a long steady-state cutting process (E-G).

2. The force started to rise sharply when the wedge was approximately 11 mm away from the transverse frame (G).

3. There is a slight kink in the rising force trace which occurred when the wedge contacted the transverse and a fold in the base plate started (H).

4. The force dropped off with cracks running from the edges of the wedge at L. Material ahead of the wedge began to fold in the concertina mode.

5. At M, the entire weld connecting the transverse frame to the base plate broke. The break also extended up 1/4 the length the weld joint with the frame and one of the longitudinal supports. The material ahead of the wedge continued to fold in the concertina mode. Simultaneously, the transverse frame continued to tear away from the longitudinal support at the weld on one side

and was pushed out of the way by the advancing wedge. It pivoted about the weld joint with the other longitudinal support.

6. At O, the concertina mode was observed.

The mirrored specimen deformed somewhat differently. The weld between the bottom plate and the transverse failed on one side of the cut but remained intact on the other. The transverse frame was torn from the longitudinal support for 3/4 of the joint length on same side of the cut where the bottom joint failed completely On the other side of the cut, the tear extended only 1/4 the length of the joint. The central separation mode was observed for this specimen at O.

Photographs from Test #2 are shown in Figure 3-4. The concertina folding ahead of the wedge and the progressive tearing of the transverse frame from the longitudinal supports is clearly shown. The frame is completely torn from the support on one side. This occurred during the sudden weld break. Also, the stretching of the transverse frame about the wedge face is visible.

3.2 Wide Specimen Test Results (B/S = 0.238)

Two sets of tests were performed on this type of model. The results from both tests were similar.

3.2.1 Test #3 - Wide Specimen

This discussion follows the force-displacement plot shown in Figure 3-5.

1. There was an initial rise in force as the wedge contacted the plate at A. This was followed by a drop in force at D as a longitudinal crack was formed ahead of the wedge. The force then rose and finally leveled off at E.

2. From E to F there was a moderate increase in force as the cut flaps contacted the longitudinal supports. The flaps remained in contact during the test. An additional rise in force was observed from F to G as the flaps were bent parallel to the longitudinal supports.

3. When the wedge was about 15 mm away from the transverse, (G), the force began to rise sharply. As the wedge progressed to H, the crack split into two diverging cracks, resulting in a force drop. The cracks fanned out, stopping when they reached the frame about halfway to the longitudinal supports, then the force level started to rise again at I.

4. At J, the wedge contacted the transverse frame and both the transverse frame and the base plate started to fold along the contact line. After the first fold was completed at K, the force rose to the peak value at L. At L, cracks began at the edges of the wedge, causing the force level to drop. Popping was heard as segments of weld broke. The transverse frame was completely separated from the bottom plate. Approximately 7/8 of the transverse frame was torn from the longitudinal supports on both sides. After the test, the longitudinal supports were observed to have bent in about 10 mm on each side near the joints with the transverse frame.

5. From M, concertina folding was continued with N indicating a local peak. The force level continued to oscillate with a definite downward trend.

Similar damage was observed on the mirrored specimen. The joint between the transverse frame and the longitudinal support was intact on one side, but 7/8 of the length was torn on the other side. The joint between the bottom plate and the transverse frame detached completely on one side of the cut, but remained intact on the other side. The bottom and longitudinal support joints were intact on the same side.

Two photographs representative of the damage are shown in Figure 3-6. The diverging concertina folding ahead of the wedge is clearly visible as is the bending of the longitudinal supports. The imprint of the wedge into the transverse frame is seen, indicating the stretching which occurred.

3.2.2 Test #4 - Wide Specimen

This discussion follows the force-displacement plot shown in Figure 3-7. The initial portion of this test was very similar to Test #3.

1. From A, there was an initial increase in force as the cutting process began, followed by a long, slow increase in cutting force with the cut flaps in contact with the longitudinal supports (E-G).

2. The force started to rise sharply at G when the wedge was approximately 10-15 mm away from the transverse member. There was a slight drop in force at H as the crack diverged. The force level quickly rose from I as the cracks fanned and reached the frame about halfway to the longitudinal supports.

3. At J, the wedge contacted the frame and material began to fold over. As the fold was completed, the force rose again.

4. The force reached the peak value at L and cracks began to appear at the edges of the wedge. The sound of weld popping was apparent as the force began to decrease rapidly past M. The joint between the bottom plate and the transverse frame detached on one side of the cut but remained intact on the other. As the wedge progressed, the frame was torn from the longitudinal support for 7/8 of the weld joint length.

5. The concertina mode continued from M with a local peak at N.

The mirrored specimen had somewhat different damage characteristics. The frame was completely detached from the bottom plate on both sides. It was also completely detached from the longitudinal support on one side. The other side was torn over 7/8 of its length. The concertina mode was observed until the end of the test.

Figure 3-8 contains two photographs illustrating some of the deformation observed. The joint between the transverse frame and longitudinal support is completed detached on one side. The concertina folding is seen to be veering to the opposite side. As with Test #3, the longitudinal supports are bent in at the transverse frame and an imprint of the wedge face is visible on the transverse frame.

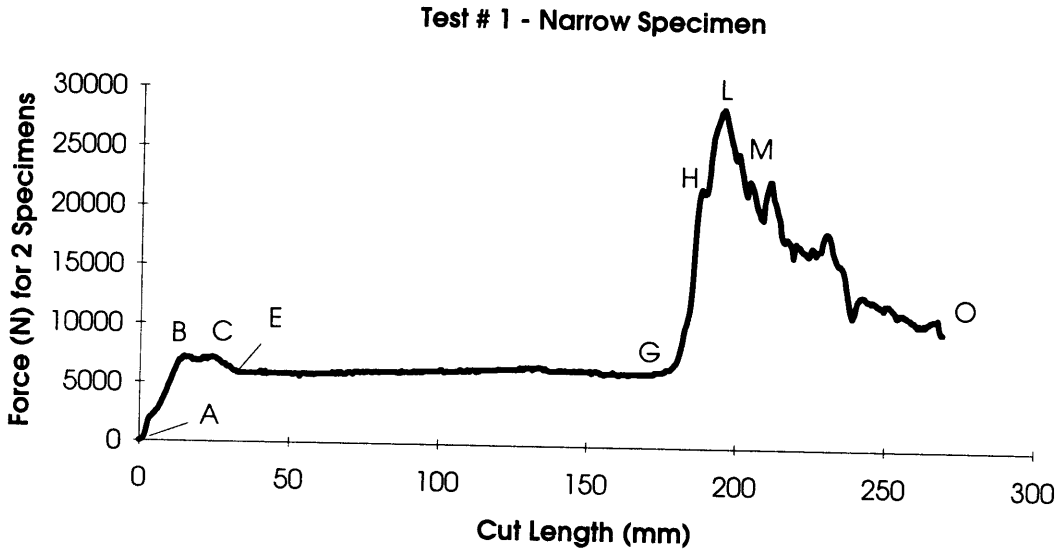

Figure 3-1. Test #1 Force-Displacement Plot
(B/S = 0.119)

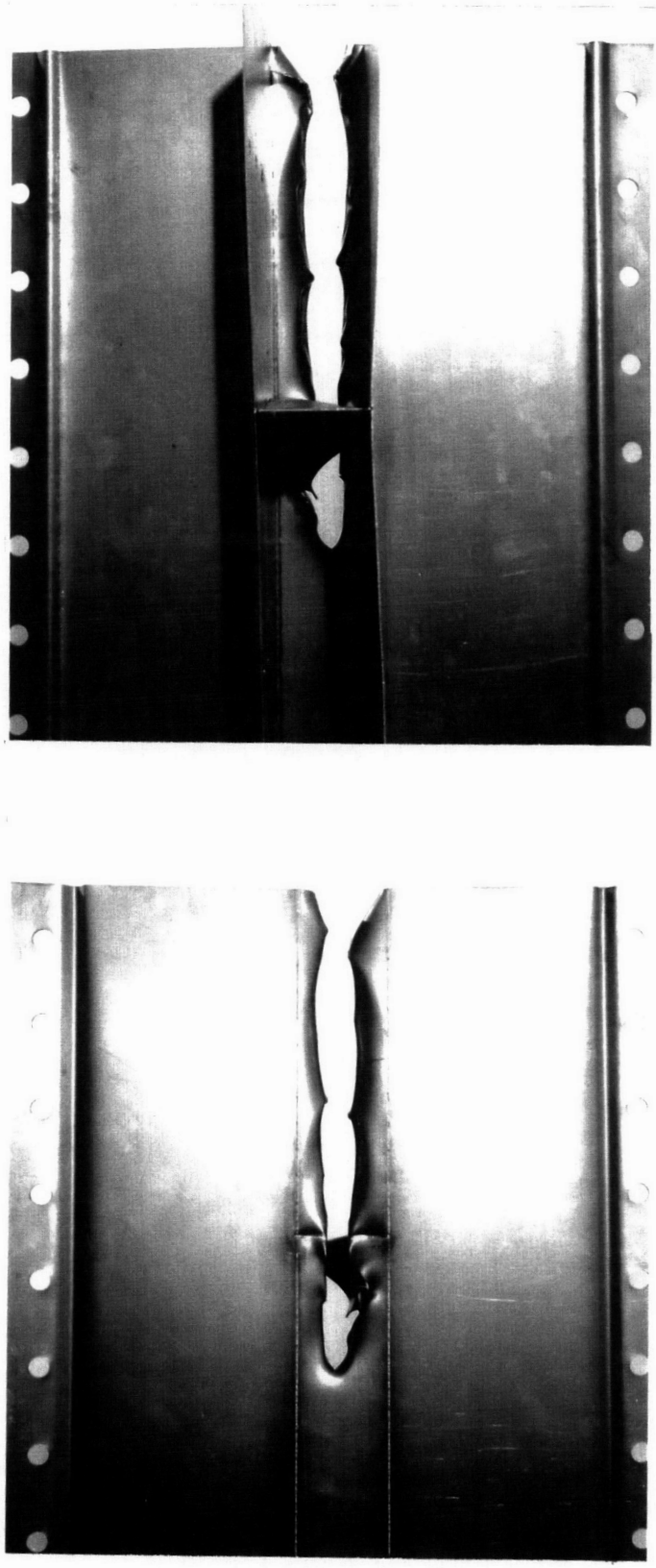

Figure 3-2. Test #1 Photographs

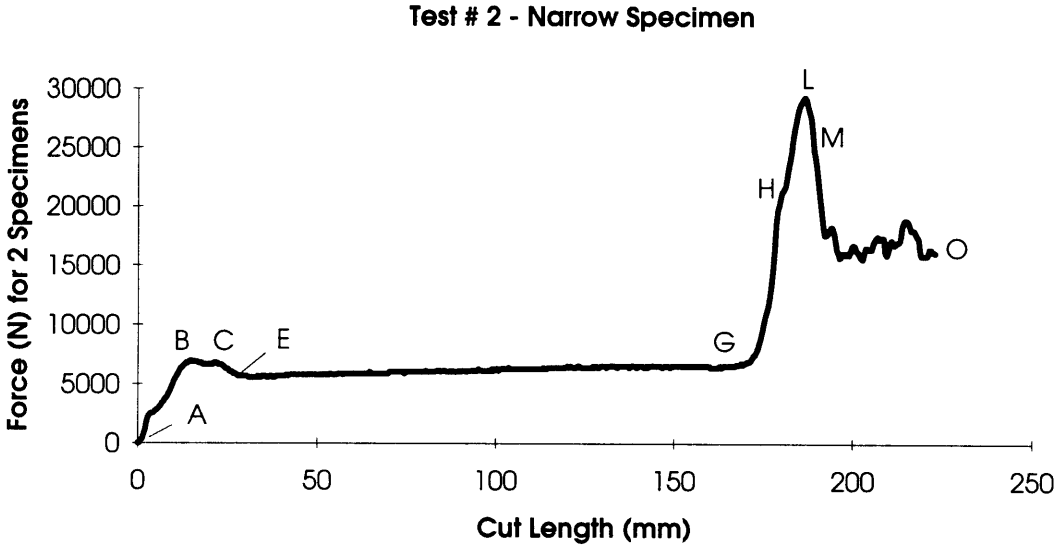

Figure 3-3. Test #2 Force-Displacement Plot
(B/S = 0.119)

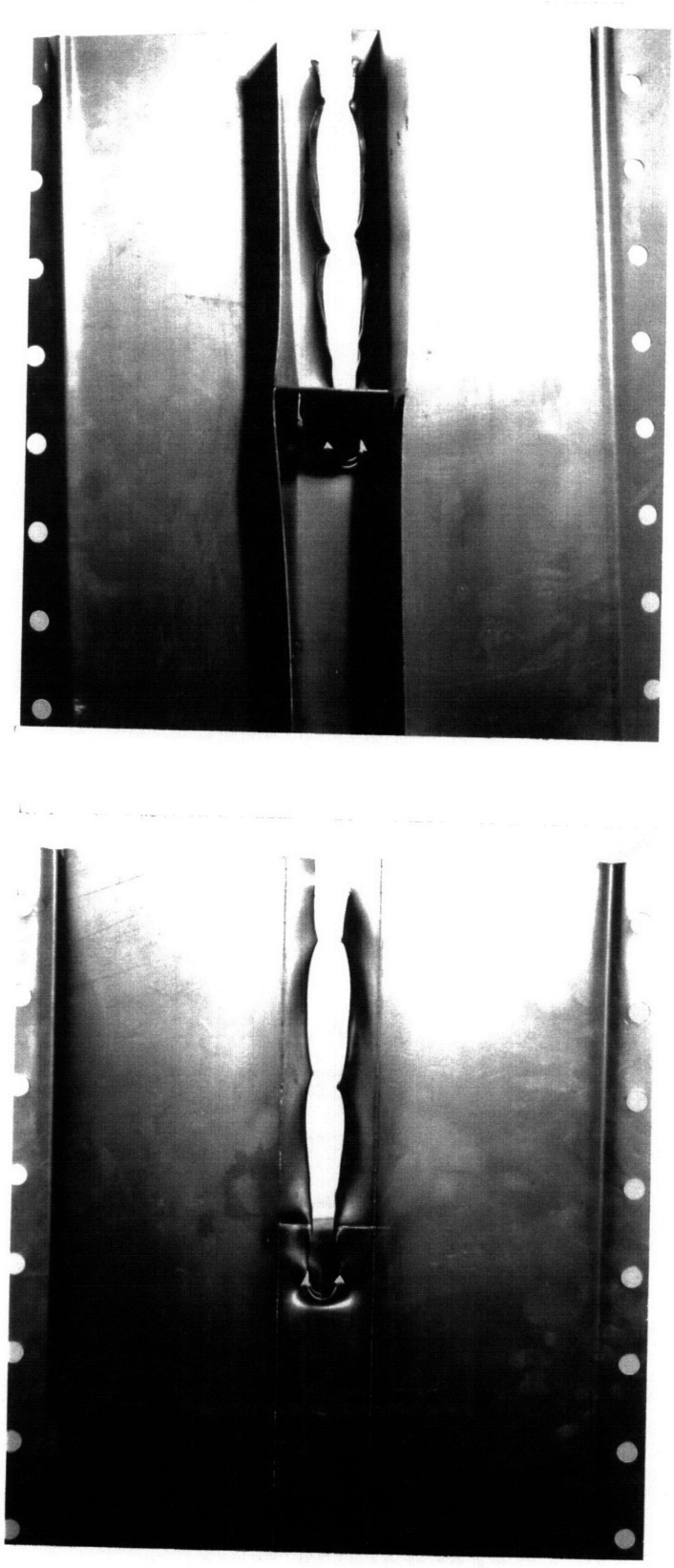

Figure 3-4. Test #2 Photographs

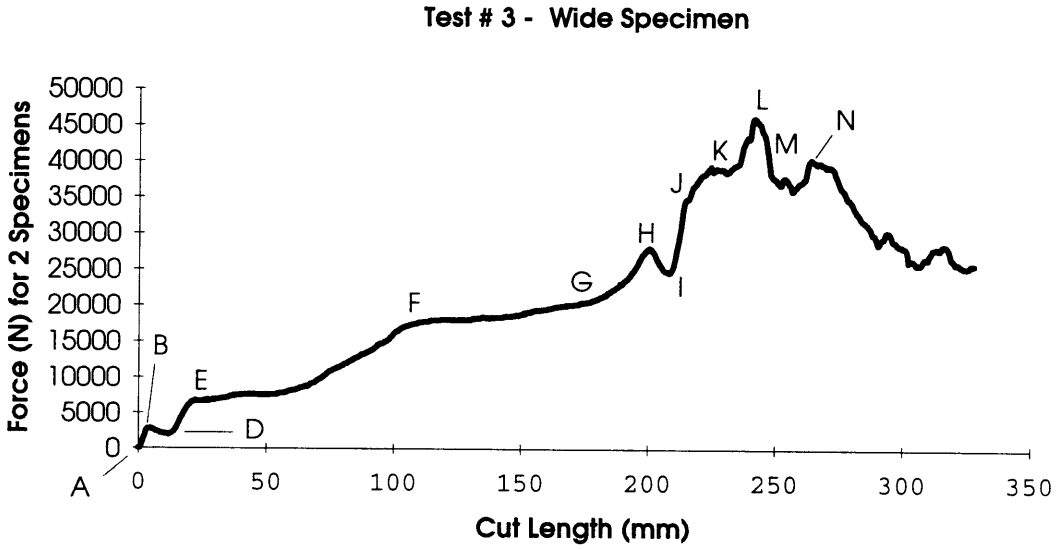

Figure 3-5. Test #3 Force-Displacement Plot
(B/S = 0.238)

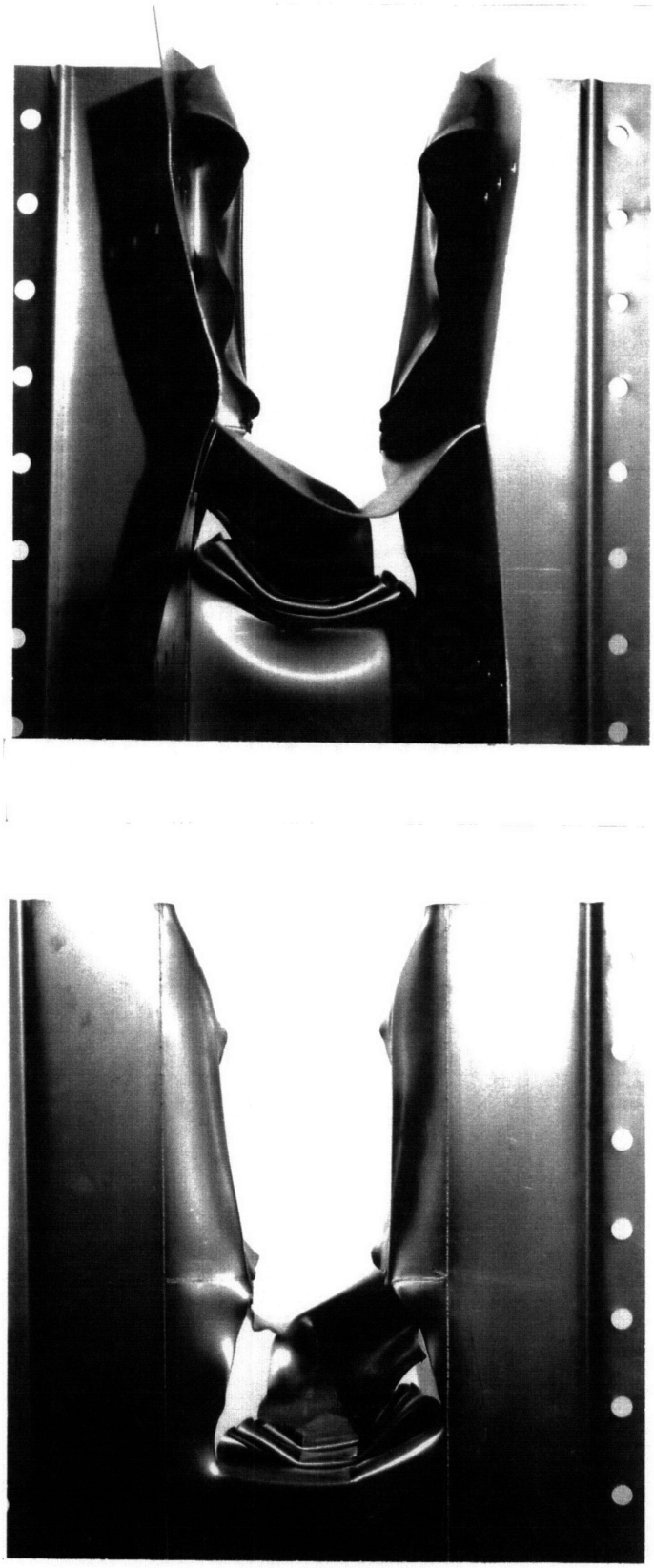

Figure 3-6. Test #3 Photographs

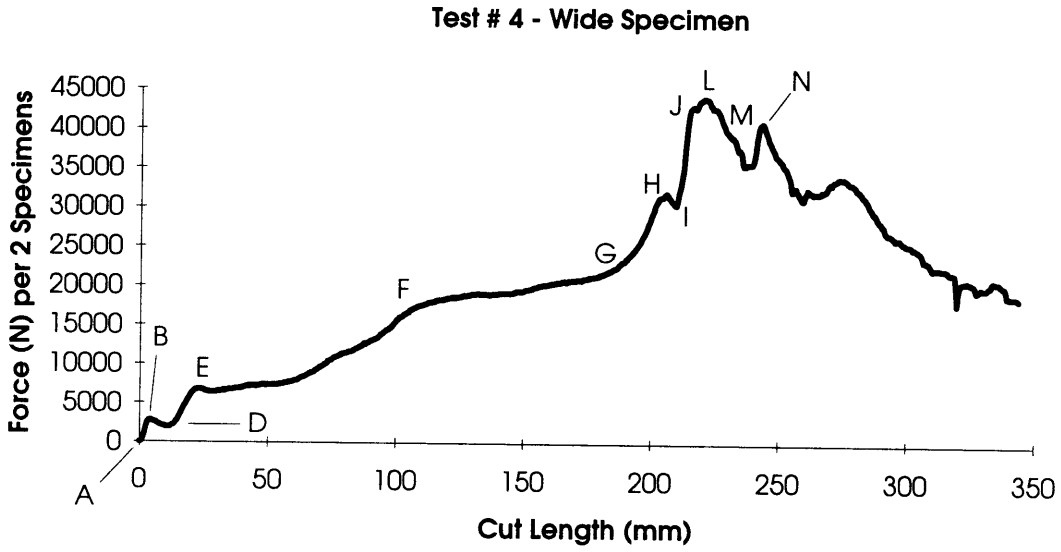

Figure 3-7. Test #4 Force-Displacement Plot
(B/S = 0.238)

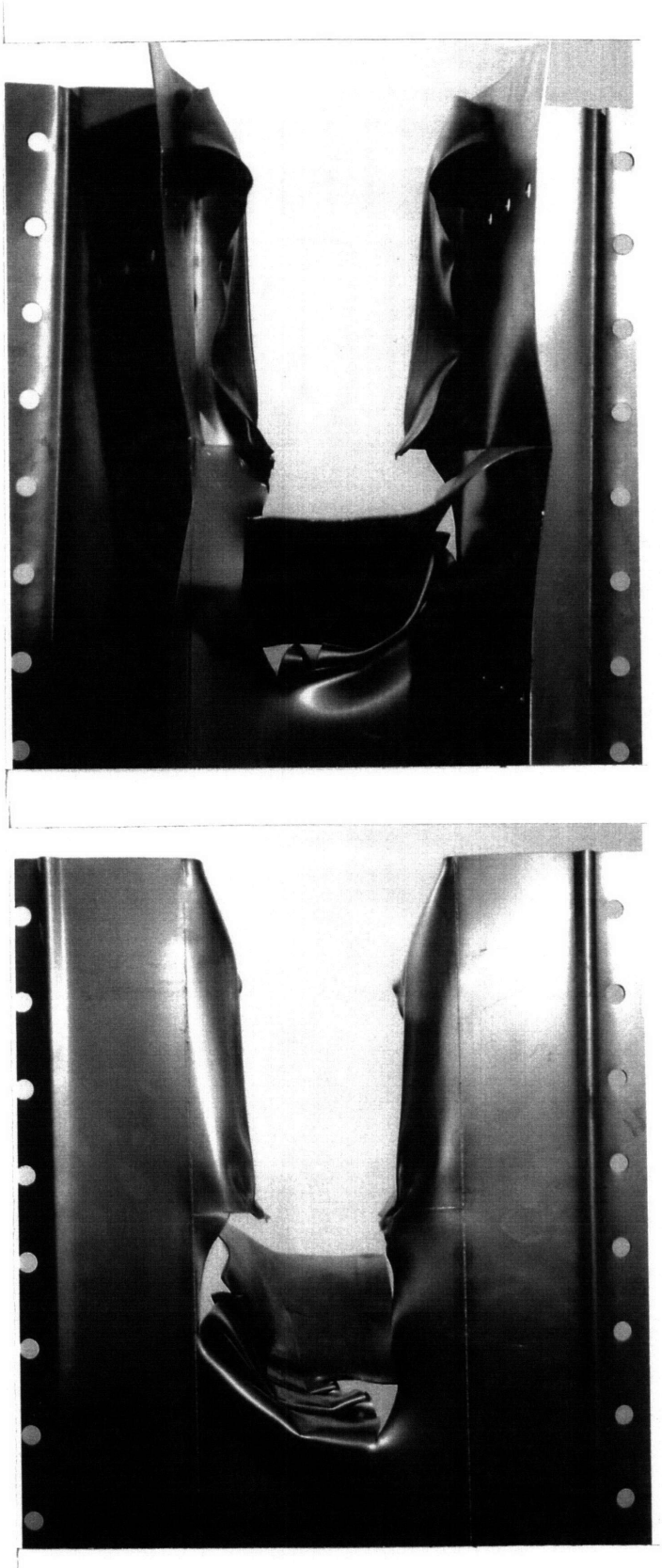

Figure 3-8. Test #4 Photographs

4.0 Analytical Models and Discussion

In the previous chapter, the results of the experiments were presented. This chapter takes the next step by developing a set of analytical models for the transversely stiffened plate cutting problem. The entire process was separated into distinct phases and a different model was developed for each. Once developed, the analytical models were compared to the experimental data. Finally, a simplified version of the analytical model was developed for the purpose of predicting ship damage and compared to the experimental data and a simple theory from the literature.

4.1 Problem Definition

An approximate solution to the transversely stiffened plate cutting problem was developed by equating the rate of external work to the rate of internal plastic work for an assumed deformation field. The upper bound theorem for the limit load, with a given geometry and no friction, as stated by Calladine (1985) is:

"If an estimate of the plastic collapse load of a body is made by equating the internal rate of dissipation of energy to the rate at which external forces do work in *any* postulated mechanism of deformation of the body, the estimate will be either high, or correct."

Defining F_p as the plastic resisting force, $\dot{\Delta}$ as the rate of indentation or wedge velocity, $\dot{W}_b$ as the rate of bending work and $\dot{W}_m$ is the rate of membrane work, the rate of work of external forces is equated to the rate of internal plastic work mathematically as;

$$F_p \dot{\Delta} = \dot{W}_b + \dot{W}_m, \tag{4.1}$$

In a plane stress condition where $M_{\alpha\beta}$, $N_{\alpha\beta}$, and $\dot{K}_{\alpha\beta}$, $\dot{\varepsilon}_{\alpha\beta}$ denote respectively the tensors of plastic bending moments and membrane forces and corresponding strain rates; $M_0 = \sigma_0 t^2 / 4$ is the fully plastic bending moment with a flow stress of σ_0 and a plating thickness of t; $\dot{\phi}^{(i)}$ is the rate of rotation of the "i-th" hinge line and ℓ_i is the length of the hinge line, $\dot{W}_b$ and $\dot{W}_m$ are defined as;

$$\dot{W}_b = \int_S M_{\alpha\beta} \dot{K}_{\alpha\beta} \, dS + \sum_{i=1}^{n} M_o \dot{\phi}^{(i)} \ell_i \tag{4.2}$$

$$\dot{W}_m = \int_S N_{\alpha\beta} \dot{\varepsilon}_{\alpha\beta} \, dS \qquad \alpha , \beta = 1 , 2. \tag{4.3}$$

The summation in equation (4.2) is performed over *n* hinge lines and represents the contribution of the discontinuous deformation field. An upper bound for Fp is obtained provided a kinematically admissible velocity field, $\dot{u}_\alpha (x , y)$ can be constructed which is compatible with the kinematic boundary conditions (wedge motion $\dot{\Delta}$) and the strain rate field ($\dot{K}_{\alpha\beta}$, $\dot{\varepsilon}_{\alpha\beta}$, $\dot{\phi}$) .

The solution to the transversely stiffened plate problem was broken down into several stages. The pre-frame stage starts at the initiation of the cut and ends when the effects of the transverse frame are first noticed. The frame interaction stage includes all effects associated with the transverse frame. It is further broken down into 4 phases: stiffening, pre-rupture, post-rupture and decay. Finally, the post-frame stage starts from the point where the transverse frame effects are insignificant and lasts until the end of the test. Table 4-1 lists

the solution stages, identifies the section each stage is developed in and notes the mechanism used to model the stage.

Table 4-1. Summary of Transverse Member Solution Stages

Stage	Phase	Section	Mechanism
Pre-frame	---	4.2	Steady-state Cutting
Frame Interaction	Stiffening	4.3.1 4.3.2	• Diverging Crack • Web Girder Crushing
	Pre-rupture	4.4.1 4.4.2	•Corner Element Crushing • Membrane Stretching & Concertina Tearing
	Rupture	4.4.3	Membrane Stretching, Concertina Tearing & Local Tearing
	Decay	4.4.4	Bending, Concertina Tearing & Local Tearing
Post-frame	---	4.5	Concertina Tearing

For all models, the material is assumed to be rigid-plastic and non-hardening. Coupling between membrane and bending stresses is not taken into account. It was assumed that regions experiencing high bending stresses have negligible membrane stresses. Conversely, regions developing high membrane stresses have negligible bending stresses. Figure 4-1 illustrates the

difference between the assumed and actual interaction curve for bending and membrane stresses.

4.2 Pre-Frame Stage

Zheng and Wierzbicki (1994) derived a simplified solution for the steady-state plate cutting process. This equation was presented as equation (1.4) and is used to define the cutting portions used in these tests. The equation is restated as;

$$\frac{F}{M_o} = (4 \frac{B}{t} \sin\theta \tan\theta + 3\pi)(1 + \mu \cot\theta). \qquad (1.4)$$

In situations were either the plate is tilted or the wedge face is sloped (γ is the tilt angle or complementary to the wedge sloping angle), equation (1.4) is corrected by using the projected wedge angle θ';

$$\tan\theta' = \tan\theta \cos\gamma. \qquad (1.4a)$$

Figure 4-2 illustrates the simplified cutting model used. The expression appears to be based on progressive folding of material at a hinge rather than the flow of material through a given hinge.

4.3 Stiffening Model

There were three observed mechanisms which provided stiffening during the transverse frame cutting process. As the wedge approached to within seven to ten time the plating thickness of the transverse frame (G on Figures 3-1, 3-3, 3-5 and 3-7), the force started to rise during all four experiments. The crack ahead of the wedge was observed to diverge as this occurred. A second observed

mechanism was the drop in force as the wedge touched the transverse frame (H on Figures 3-1, 3-3, 3-5 and 3-7). The drop was of short duration. Finally, the peak load observed during the experiments (L on Figures 3-1, 3-3, 3-5 and 3-7) was beyond what could be predicted by the models developed in this thesis. After studying the results, it was concluded the peak force was due to the crushing of the corner elements. This section discusses two of these mechanisms. The effects of the third mechanism is discussed qualitatively in Section 4.4.1.

4.3.1 Crack Splitting Model

When the wedge was a distance equal to ηt from the transverse member, where η varies from 7-10 and t is the plating thickness, the force was observed to rise sharply. This was followed by the divergence of the crack ahead of the wedge as discussed in Section 3.2 Two separate models were considered for the stiffening mechanism. The first considers the membrane and bending forces involved in the process, while the second considers the bending and local tearing forces. Figure 4-3 illustrates the geometry used as a basis for both models. The cracks extend from the intersection between the transient and steady-state cutting flaps as shown.

4.3.1.1 Combined Membrane and Bending Model

The model begins when the wedge is a distance of ηt from the transverse frame. As the wedge advances, the plate flap undergoes bending and stretching. The hinge line is assumed to be along the transverse member. As the flap is bent out of plane, there is stretching across the gap with the remainder of the plate. The stretched zone is indicated by the shaded area. The flap is assumed to remain rigid throughout the deformation process,

touching the wedge face at a single point. A circular wedge is assumed. Although the wedge advances at a constant rate, the rate of rotation of the flap increases exponentially as the point of tangency travels around the face of the wedge. This mode is exhausted when ω , the angle between the flap and the base plate, reaches 90 degrees.

4.3.1.1.1 Rate of Membrane Work in the Flap

The rate of membrane work in the flap was derived by considering the critical strain to rupture, ε_{cr}. Without consideration of this parameter, the rotation of ω through 90 degrees would result in excessive strains. Instead, as shown in Appendix E.2, the integration was performed to the point where ε_{cr}. was reached. The corresponding rate of membrane work in the flap is;

$$\dot{W}_{m-flap} = \frac{1}{6}\,\sigma_0\, t\, B^2\, f(\Delta)\,\dot{\Delta}\,\frac{\varepsilon_{cr}^3[1-\sin\theta]}{\sin^2\theta[1-\cos\omega]^{3/2}}\ . \qquad (4.4)$$

where

$$f(\Delta) = \frac{B\cos\theta^*}{\sqrt{(\eta t-\Delta)^2+2B(\eta t-\Delta)(B+\eta t-\Delta)}}\,\frac{1}{2\sqrt{\sin\theta^*-\sin\theta}\sqrt{1-\sin\theta^*}}, \qquad (4.5)$$

$$\theta^* = \sin^{-1}\left(\frac{B}{B+\eta t-\Delta}\right), \qquad (4.6)$$

$$\omega = \cos^{-1}\left[\frac{\sqrt{1-\sin\theta^*}}{\sqrt{1-\sin\theta}}\right], \qquad (4.7)$$

and Δ is the increment of wedge advancement.

4.3.1.1.2 Rate of Bending Work in the Flap

The rate of bending work, $\dot{W}_b$, in general consists of work dissipated by the continuous deformation field and the discontinuous deformation field. In this model, the deformation field consists of only rigid plate elements and stationary plastic hinges. Thus, the first term on the right hand side of equation (4.2) is not applicable to the calculations. As shown in the derivation in Appendix E.3, the rate of bending work in the flap is;

$$\dot{W}_{b-flap} = 2M_0\dot{\Delta}f(\Delta)\frac{B}{\sin\theta} \quad . \tag{4.8}$$

4.3.1.1.3 Total Membrane/Bending Force

Defining the external rate of work as;

$$\dot{W}_{ext} = F_T\,\dot{\Delta} \tag{4.9}$$

and equating the rate of internal work to the rate of external work as in equation (4.1) yields;

$$\dot{W}_{ext} = \dot{W}_{b-flap} + \dot{W}_{m-flap} \quad . \tag{4.10}$$

Substituting equations (4.4), (4.8) and (4.9) in equation (4.10) yields the following normalized expression for the sum membrane and bending force in the flap;

$$\frac{F_M}{M_0} = [\frac{2B^2(1-\sin\theta)}{3t\sin^2\theta}\frac{1}{(1-\cos\omega)^{3/2}} + \frac{2B}{\sin\theta}]f(\Delta). \tag{4.11}$$

4.3.1.2 Combined Bending and Tearing Model

This model was computed as an alternative to the membrane and bending model. The geometric parameters and contribution of bending rate of work are the same for both models. The difference arises from considering the rate of local tearing work along the flap edge instead of the rate of membrane work. This method does not consider critical strain to rupture.

4.3.1.2.1 Rate of Local Tearing Work in the Flap

The rate of local tearing work is defined using the specific work to fracture, R^*, as;

$$\dot{W}_t = R^* t \dot{\Delta} \ . \tag{4.12}$$

In general, R^* is not a material parameter but depends upon the plate thickness as determined by carefully planned and interpreted tests. According to Atkins (1991), the value of R^* varies from 300-1000 N/mm depending on the thickness and mode of fracture. The rate of local tearing work, as derived in Appendix E.5, is;

$$\dot{W}_t = \frac{2R^* tB}{\sin\theta} g(\Delta)\dot{\Delta} \ , \tag{4.13}$$

where

$$g(\Delta) = \frac{B}{\sqrt{(\eta t - \Delta)^2 + 2B(\eta t - \Delta)(B + \eta t - \Delta)}}. \tag{4.14}$$

4.3.1.2.2 Total Tearing/Bending Force

Substituting equation (4.13) for equation (4.4) in equation (4.10) results in the following expression for normalized tearing/bending force;

$$\frac{F_T}{M_0} = \frac{2B}{\sin\theta}[f(\Delta) + \frac{4R^*}{\sigma_0 t} g(\Delta)]. \qquad (4.15)$$

Figure 4-4 compares the normalized force-deflection plots for the membrane, bending and tearing force components. As shown, the value of each curve approaches infinity as Delta* approaches a value of 1, indicating the stiffening effect as the wedge approaches the transverse frame.

4.3.2 Web Girder Crushing Model

During the experiments, it was observed that the deformation of the transverse frame - base plate unit was similar to the crushing of a web girder. In this case, the transverse frame serves as a flange and the base plate below the transverse serves as a web. The web girder crushing problem was previously solved by Culbertson-Driscoll (1992) and subsequently modified by Choi, Wierzbicki & Culbertson-Driscoll (1994). In the modified solution by Choi et al., a model was constructed using constant depth hinges. The constant hinge depth model was adopted and modified to the particulars of the transverse frame case.

4.3.2.1 Model Description

Figure 4-5 illustrates the undeformed and deformed cases of the model. As the wedge contacts the transverse member, the transverse and base plate both undergo bending and stretching deformation. The decay mechanism involves

four plastic hinge lines as indicated in Figure 4-5. As the wedge progresses, the middle hinge line moves out of plane, and the base plate and transverse member are subjected to an in-plane stretch. Stretching is indicated by the shaded area.

The first hinge line forms at the connection between the transverse member and the base plate. From experimental observation, it was postulated that the second and third hinge lines were formed at predetermined distance H, where H is the wavelength of a concertina fold. Defining b as the wedge width and t as the plate thickness, H is found according to Wierzbicki (1993), (1994) as;

$$H = 0.56\, b^{2/3}\, t^{1/3}. \tag{4.16}$$

The fourth hinge line varies as a function of the wedge indentation as shown in Figure 4-5. The extent of the plastic damage zone, ζ , is assumed to equal the half-width of the wedge, B. This assumption is based on experimental observation. With H and ζ known, the hinge angles α and β are uniquely determined for a particular wedge width and plating thickness. The magnitude of the stretching of the transverse member due to membrane action is assumed equal to the base plate in order to ensure material continuity at the weld joint.

4.3.2.2 Rate of Membrane Work

Defining $\overline{N_0} = \sigma_0 t_f$ and $N_0 = \sigma_0 t_p$ as the fully plastic membrane force per unit length for the flange (transverse) and the web (base plate) respectively; t_f and t_p as the thickness of the flange and web respectively, the rates of membrane work of the web and flange, as derived in Appendix F.2, are given as;

$$\dot{W}_{m\text{-}web} = 4\,N_0\,H\,[-\frac{\Delta}{4\zeta}\sqrt{\Delta^2+\zeta^2} + \frac{\zeta\,\sin\phi_0\,(\cos\alpha\,\cos\Phi-\cos\beta)}{2\,(\cos\alpha\,\sin\phi_0-\cos\beta\,\sin\theta_0)^2}]\dot{\Phi} \quad (4.17)$$

and

$$\dot{W}_{m\text{-}flange} = -\frac{\overline{N_0}\,\rho\,\zeta\,\Delta}{\zeta}\sqrt{\Delta^2+\zeta^2}\,\dot{\Phi}\,, \quad (4.18)$$

The remaining geometric parameters are defined in Figure 4-5.

4.3.2.3 Rate of Bending Work

For the web girder crushing model, the deformation consists of only rigid plate elements and stationary plastic hinges. Thus, only the discontinuous portion of equation (4.2) is considered. The rates of bending work of the web, flange and due to the indenter effect, as derived in Appendix F.3, are given as;

$$\dot{W}_{b\text{-}web} = -2\,\zeta\,M_0\,\dot{\Phi}\,[\frac{C_3-C_4\cos\Phi-\cos^2\Phi}{\cos\alpha\,\sin\Phi\,\sqrt{C_1+C_2\cos\Phi-\cos^2\Phi}}], \quad (4.19)$$

$$\dot{W}_{b\text{-}flange} = -2M_0\dot{\Phi}(\frac{\Delta^2+\zeta^2}{\zeta})\,[\frac{\rho(1+\rho^2)}{\rho^2+(1+\rho^2)\psi^2} + \frac{\rho^2+2\rho^2\psi^2+(1+\rho^2)\psi^4}{[\rho^2+(1+\rho^2)\psi^2]\sqrt{\rho^2+\rho^2\psi^2-\psi^4}}]\,\frac{t_f^2}{t_p^2}\,, \quad (4.20)$$

and

$$\dot{W}_{b-ind} = M_0 b_1 \dot{\Delta}[\frac{4}{\sqrt{4\Delta H-\Delta^2}} + \frac{2\rho}{(\rho^2+\psi^2)\zeta}], \quad (4.21)$$

where

$$C_1 = \sin^2\alpha - \cos^2\beta\,, \qquad C_2 = 2\cos\alpha\cos\beta$$

$$C_3 = \cos^2\alpha + \frac{\cos\alpha\cos\beta}{\cos\phi_0} + 1, \quad C_4 = \frac{\cos^2\alpha}{\cos\phi_0} + \cos\alpha\cos\beta. \tag{4.22}$$

4.3.2.4 Rate of External Work

The external work rate, as derived in Appendix F.4, is given as;

$$\dot{W}_{ext} = F_p\dot{\Delta} = -F_p\dot{\Phi}\frac{\Delta^2+\zeta^2}{\zeta}. \tag{4.23}$$

4.3.2.5 Crushing Force

Equating the external to the internal rate of work as in equation (4.1) yields;

$$\dot{W}_{ext} = \dot{W}_{b\text{-}web} + \dot{W}_{b\text{-}flange} + \dot{W}_{m\text{-}web} + \dot{W}_{m\text{-}flange} + \dot{W}_{b\text{-}ind}. \tag{4.24}$$

Substituting equations (4.17), (4.18), (4.19), (4.20) and (4.21) into equation (4.24) and normalizing with respect to M_0 results in the following load-deflection relationship in dimensionless form;

$$\begin{aligned}\frac{F_p}{M_0} = \frac{1}{1+\psi^2}\Bigg[&\frac{2(C_3 - C_4\cos\Phi - \cos^2\Phi)}{\cos\alpha\sin\Phi\sqrt{C_1 + C_2\cos\Phi - \cos^2\Phi}} - 8H^*\frac{\sin\phi_0(\cos\alpha\cos\Phi - \cos\beta)}{(\cos\alpha\sin\phi_0 - \cos\beta\sin\theta_0)^2}\Bigg] \\ &+ 2t^{*2}\Bigg[\frac{\rho(1+\rho^2)}{\rho^2+(1+\rho^2)\psi^2} + \frac{\rho^2+2\rho^2\psi^2+(1+\rho^2)\psi^2}{\rho^2+(1+\rho^2)\psi^2}\frac{1}{\sqrt{\rho^2+\rho^2\psi^2-\psi^4}}\Bigg] \\ &+ 4H^*\sin\theta_0(1+t^*\rho\zeta^*) + b_1^*\Bigg[\frac{4}{\sqrt{\Delta^*(4-\Delta^*)}} + \frac{2t^{*2}\rho}{(\rho^2+\psi^2)\zeta^2}\Bigg]\end{aligned}, \tag{4.25}$$

where the nondimensionalized quantities are defined as;

$$\psi = \frac{\Delta^*}{\zeta^*} = \frac{\Delta}{\zeta}, \quad \Delta^* = \frac{\Delta}{H}, \quad \zeta^* = \frac{\zeta}{H}, \quad H^* = \frac{H}{t_p}, \quad t^* = \frac{t_f}{t_p}, \quad b_1^* = \frac{b_1}{H}. \qquad (4.26)$$

This model is subject to a physical limitation which occurs when either the first hinge angle reaches 90 degrees if $\alpha \leq \beta$ or when the third hinge angle reaches 90 degrees. At this limit, the degree of freedom for the indentation is exhausted. Figure 4-6 is a dimensionalized plot of equation (4.24) using parameters from the narrow specimens (B/S=0.119). Figure 4-7 is a dimensionalized plot of equation (4.24) using parameters from the wide specimens (B/S=0.238).

The graphs indicate an infinite value at zero indentation because a rigid plastic material assumption was used. In reality, the peak load is defined by the ultimate strength of the web girder. Thus, the crushing force rises linearly from zero to the ultimate strength, then decays as depicted by the crushing model graphs.

By itself, the web girder solution inadequately describes the frame interaction process. The physical limitation limits the depth of indentation to 3 mm on the narrow specimen and 15 mm on the wide specimen. Experimentally, the decay occured over 30 mm on the narrow specimen (Test #1) and over 60 mm on the wide specimen (Test #3). Nor does the model help predict the peak load. The calculated ultimate strength of the narrow web girder model is on the order of 15,000 N (for 2 specimens), approximately 50% of the peak value of force observed. The web girder crushing model does help to explain the slight drop in force observed at H in Figures 3-1, 3-3, 3-5 and 3-7. Once contact is made and the ultimate strength reached, there is a rapid drop in force as shown in Figures 4-6 and 4-7. However, this rapid drop is offset by an additional stiffening mechanism, corner element crushing.

4.4 Transverse Frame Interaction Model

Prior to the development of the interaction model, a stiffening mechanism due to corner crushing is discussed. Then, ignoring the effects of corner crushing, a model is developed which separates the process through which the wedge passes through the transverse frame into three phases. Phase I starts when the wedge contacts the frame and ends when the material in the frame ruptures. Phase II includes the progressive tearing of the frame away from the longitudinal support members. Finally, Phase III describes the transition as the wedge-frame interaction is concluded.

4.4.1 Corner Element Crushing

As the wedge touches the transverse member and continues to advance, there is an additional obstruction in its path. For a circular face wedge, the remaining base plate to the sides of the wedge combines with the transverse frame to form a corner element as depicted in Figure 4-8. In order for the wedge to advance, both corner elements must be progressively crushed. The crushing of corner elements has been studied by Wierzbicki and Abramowicz (1983), Abramowicz and Wierzbicki (1989) and Wierzbicki, Recke, Abramowicz and Gholami (1994). The force required to crush one is characterized by a steep force-deformation curve. Figure 4-9 illustrates the general shape of such a curve qualitatively.

Solution of the corner element problem is needed to provide an estimate of the peak force as the wedge passes through the transverse member. Such a solution is complicated, however, and is beyond the scope of this thesis. Instead, the approach will be to predict the total amount of energy required. This is the subject of Section 4.4.

4.4.2 Phase I - Pre-rupture of Transverse Frame

Figure 4-10 is a simplified model of the wedge-frame interaction. As the wedge presses into the frame, the frame progressively stretches into a shape compatible with the wedge face. The face of the wedge is assumed to be sloped such that the displacement of the frame due to the wedge varies from δ at the base plate to zero at the top of the wedge. The displacement of the wedge from the point where contact was initiated is denoted as δ. In addition, the total width of the stretched zone is assumed equal to the wedge width, 2B.

4.4.2.1 Critical Strain to Rupture

Considering the in-plane component of strain along the y-axis as negligible, the strain in the stretched area is calculated as;

$$\varepsilon = \frac{1}{2}\left(\frac{dw}{dy}\right)^2. \tag{4.27}$$

The maximum slope occurs at the intersection of the base plate and the frame, or;

$$\left(\frac{dw}{dy}\right)_{max} = \frac{\delta}{B}. \tag{4.28}$$

Setting the maximum strain equal to the critical strain to rupture and solving for the critical displacement to rupture yields;

$$\delta_c = B\sqrt{2\varepsilon_c}. \tag{4.29}$$

4.4.2.2 Rate of Membrane Work in the Transverse Frame

Defining $N_0 = \sigma_0 t_f$ as the fully plastic membrane force in the transverse frame, dS=dxdy and $\dot{\varepsilon}$ as the velocity strain, the rate of membrane work in the transverse frame is;

$$\dot{W}_{frame} = \int_S N_0 \dot{\varepsilon} ds. \tag{4.30}$$

From Figure 4-10, w is seen to vary as a function of both x and y. Using the geometry from Figures 4-10 and 4-11, the displacement function is;

$$w(x,y) = \delta(1 - \frac{x}{\xi})(1 - \frac{y}{B}). \tag{4.31}$$

From equation (4.27), the velocity strain calculated as;

$$\dot{\varepsilon} = \frac{dw}{dy}\frac{d\dot{w}}{dy}. \tag{4.32}$$

Differentiating equation (4.31) yields;

$$\frac{dw}{dy} = -\frac{\delta}{B} + x\tan\gamma, \tag{4.33}$$

and

$$\frac{d\dot{w}}{dy} = -\frac{\dot{\delta}}{B}. \tag{4.34}$$

Substituting equations (4.33) and (4.34) into equation (4.32) results in the following expression for the rate of membrane work in the frame;

$$\dot{W}_{m-frame} = 2N_0 \frac{\delta\dot{\delta}}{B^2} \int_0^B \int_0^{\xi} (1 - \frac{x}{\xi}) dxdy. \tag{4.35}$$

Evaluating the integral yields;

$$\dot{W}_{m-frame} = \frac{N_0 \delta^2 \dot{\delta}}{B \tan\gamma}. \tag{4.36}$$

4.4.2.3 Membrane Force in the Transverse Frame

The rate of external work on the frame is;

$$\dot{W}_{ext} = F_{frame}\dot{\delta}. \tag{4.37}$$

Equating internal and external work rates yields the membrane force in the transverse frame during Phase I;

$$F_{frame-1} = \frac{N_0 \delta^2}{B \tan\gamma}. \tag{4.38}$$

4.4.2.4 Total Force During Phase I

In addition to the frame, there is also a force due to the wedge passing through the base plate during Phase I. From experimental observation, the force is due to the concertina folding and tearing of the base plate. From Wierzbicki (1994), the mean force required to drive a wedge through a thin plate of thickness t_p in the concertina mode is;

$$F_C = 4\sigma_0 t_p^{5/3} b^{1/3} + \frac{8}{3} R^* t_p . \tag{4.39}$$

Summing equations (4.38) and (4.39), the total force during Phase I is;

$$F_{T-I} = \frac{N_0\delta^2}{B\tan\gamma} + 4\sigma_0 t_p^{5/3} b^{1/3} + \frac{8}{3} R^* t_p . \qquad (4.40)$$

Since the width of the concertina fold is increasing during the process, b is calculated as the average of the wedge width, 2B, and the longitudinal stiffener spacing, S. Equation (4.40) is valid for displacements of $\delta < \delta_c$.

4.4.3 Phase II - Post-rupture of Transverse Frame

After rupture, the wedge continues to press into the frame with cracks extending up along the edges of the wedge from the base plate to a distance of ξ as shown in Figure 4-10. During this process, there are contributions from continued stretching in the frame, the tearing of the frame from the longitudinal stiffeners and from the concertina tearing of the base plate.

4.4.3.1 Rate of Membrane Work in the Frame

The expression for the rate of membrane work is the same as equation (4.35) of Phase I, except the integration limits in the x-direction are different. Letting ξ_c denote the height of the membrane zone when rupture occurs as shown in Figure 4-11, the rate of membrane work in the transverse frame is;

$$\dot{W}_{m-frame} = 2N_0 \frac{\delta\dot{\delta}}{B^2} \int_0^B \int_{\xi_c}^{\xi} (1 - \frac{x}{\xi}) dx dy . \qquad (4.41)$$

Integrating and simplifying yields;

$$\dot{W}_{m-frame} = \frac{N_0 \delta_c^{\,2} \dot{\delta}}{B \tan\gamma}. \tag{4.42}$$

4.4.3.2 Membrane Force in the Transverse Frame

Equating internal and external work rates yields the membrane force in the transverse frame during Phase II;

$$F_{frame-II} = \frac{N_0 \delta_c^{\,2}}{B \tan\gamma}. \tag{4.43}$$

4.4.3.3 Rate of Local Tearing Work in Transverse Frame

Defining γ as the angle complementary to the sloping angle depicted in Figure 2-6, the rate of local tearing work as defined in equation (4.12) is;

$$\dot{W}_{tear} = 2R^* t_f \frac{\dot{\delta}}{\tan\gamma}. \tag{4.44}$$

Equating this with the external rate of work results in a force contribution due to transverse tearing of;

$$F_{tear} = \frac{2R^* t_f}{\tan\gamma}. \tag{4.45}$$

4.4.3.4 Total Force During Phase II

Summing equations (4.39), (4.43) and (4.45), the total force during Phase II is;

$$F_{T-II} = \frac{N_0 \delta_c^{\,2}}{B \tan\gamma} + 4\sigma_0 t_p^{\,5/3} b^{1/3} + 2R^* t_p \left(\frac{4}{3} + \frac{1}{\tan\gamma}\right). \tag{4.46}$$

Phase II continues until the top of the wedge makes contact with the transverse frame, or from $\delta_c \le \delta \le \delta_c + L\tan\gamma$.

4.4.4 Phase III - Decay of Transverse Frame Interaction Effects

Phase II ended at the point where the top of the wedge contacted the transverse frame. Beyond this point, the wedge simply pushes the transverse frame out of its path with no additional membrane force.

4.4.4.1 Rate of Bending Work in the Transverse Frame

As shown in Figure 4-11, the bending will occur about a hinge line of width 2B at a distance ξ_b above the top of the wedge. The hinge line must lie above the stretched zone because of the curvature induced by the wedge. The frame is treated as a rigid plate element. The rate of bending work in the frame, from equation (4.2) is;

$$\dot{W}_{b-frame} = 2BM_0\dot{\theta}. \tag{4.47}$$

From geometry;

$$\dot{\theta} = \frac{\dot{\delta}}{\xi_b}. \tag{4.48}$$

Substituting equation (4.48) into equation (4.47) yields the rate of bending work in the frame;

$$\dot{W}_{b-frame} = 2BM_0\frac{\dot{\delta}}{\xi_b}. \tag{4.49}$$

4.4.4.2 Bending Force in the Transverse Frame

Equating the rate of bending work, equation (4.49), with the rate of external work on the frame, equation (4.37), yields the bending force in the transverse frame;

$$F_{b-frame} = \frac{Bt_f^2\sigma_0}{2\xi_b}. \tag{4.50}$$

4.4.4.3 Total Force During Phase III

In addition to the bending of the transverse frame, there are also contributions from tearing of the frame along the edges of the wedge during bending as well as concertina tearing in the base plate. Summing equations (4.39), (4.45) and (4.50) yields the total force during Phase III;

$$F_{T-III} = \frac{Bt_f^2\sigma_0}{2\xi_b} + 4\sigma_0 t_p^{5/3} b^{1/3} + 2R^* t_p\left(\frac{4}{3} + \frac{1}{\tan\gamma}\right). \tag{4.51}$$

4.5 Post-frame Stage

It was apparent from the experiments that after the wedge passed through the transverse frame, the material continued to deform in the concertina tearing mode. Thus, for modeling purpose, the post-frame behavior is assumed to be described by the concertina tearing model given in equation (4.39). However, as noted in Section 3.1, for both of the narrow specimen tests, one of the mirrored narrow specimens transitioned back to steady-state cutting during the post-frame stage. Thus, a more complete description of the stage is that the cutting force is bounded by the concertina tearing and steady-state cutting solutions, equations (4.39) and (1.4).

4.6 Comparison of Analytical Models to Experimental Results

This section compares the analytical models developed in Sections 4.2 through 4.5 to the experimental results. Overall, the models provide a good prediction of the observed force levels even though corner element crushing was not considered in the frame interaction model.

4.6.1 Comparison with Narrow Specimens (B/S=0.119)

Figures 4-12 and 4-13 compare the predicted force levels of the analytical models presented in Sections 4.2 through 4.5. to the experimental results for the narrow specimens. The steady-state cutting portion force is estimated to within 5% by equation (1.4) for both Tests #1 and #2. Phase I is treated as a step increase in force for both tests. Since Phase I is considered to start at the point of wedge contact with the transverse frame, a delay is apparent as compared to the experimental force rise. As discussed in Section 4.3.3, the frame interaction model predicts only 80% of the peak force, but remains at that level beyond the observed decay.

For Test #1 , the transition between Phase III and concertina tearing appears to occur at approximately the same displacement where the transition occured experimentally. The trend of the cutting force can be seen heading below the level predicted by the concertina tearing model, equation (4.39). Part of the reason for this is that the mirrored specimen transitioned back to steady-state cutting. This illustrates steady-state cutting and concertina providing bounds on the force level during the post-frame stage.

For Test #2, the observed force was seen to drop suddenly due to weld breakage. This test was stopped short of the end of Phase II. The force level is still above that predicted by concertina tearing because there is still additional force required to push the frame out of the way even though there was widespread weld breakage.

4.6.2 Comparison with Wide Specimens (B/S=0.238)

Figures 4-14 and 4-15 compare the predicted force levels of the analytical models presented in Sections 4.2 through 4.5 to the experimental results for the wide specimens. As shown, equation (1.4) overestimates the 'steady-state' cutting process by approximately 25% for both tests. Part of the overestimation is due to the interference between the cut flaps and the longitudinal stiffeners described in Section 3.2. For the geometry of wedge used in Tests #3 and #4, the steady-state cutting model predicts a higher force level than concertina tearing. Thus, the onset of Phase I is treated as a step decrease in force. As with the narrow specimens, since Phase I ignores the initial stiffening before wedge contact, the curve appears shifted compared to the experimental results for both tests. Although corner element crushing was not included, Phase II predicts a peak force 10% less than that observed experimentally for both tests. However, the decay during Phase III is much steeper and more sudden than that observed experimentally.

For Test #3 , the force level during the post-frame stage is approximately twice that predicted by concertina tearing, but is seen as declining. In contrast, the post-frame force level in Test #4 is shown to be leveling off at a value which is 10% more than that predicted by concertina tearing.

4.7 Comparison of Damage Prediction Model to Experimental Results

This section provides a simplified version of the frame interaction model which would be suitable for use in a computer program which predicts ship grounding damage. It is referred to as the transverse model. As a benchmark, a comparison with the raking force model of Kuroiwa et al., (1992), equation (1.10), was also made. For illustrative purposes, the damaged area of the transverse frame was included. The frame effect was assumed to start at the point of wedge contact with the frame and last over a distance equal to the height of damage on the frame. In essence, the effect was the same as doubling the damaged area over a length equal to the wedge height. It is denoted as Kuroiwa Equivalent.

4.7.1 Transverse Frame Model

For the purpose of damage prediction with a computer, the frame interaction model presented in Section 4.4 can be simplified. Phases I and III are very steep, occurring over a short displacement. Thus, their effects can be ignored with little error. As before, the pre-frame stage is described by Zheng and Wierzbicki's steady-state cutting model, equation (1.4). The transverse model starts at the point of wedge contact with the transverse frame and ends at a distance equal to $\delta = \delta_c + L\tan\gamma$ later. The force level is described by equation (4.46). Finally, the post-frame model is described by Wierzbicki's concertina tearing solution, equation (4.39). The combination of all three components, equations (1.4), (4.39), and (4.46) represents a damage prediction model.

4.7.2 Comparison to the Narrow Specimens

Figures 4-16 and 4-17 depict force level comparisons with Tests #1 and #2. The accuracy of the analytical force level predictions is similar to that described in Section 4.6.2. The Kuroiwa Equivalent model predicts only 30% of the observed peak force level for both tests.

It is difficult to assess the accuracy of the predictions by inspection because of the variation in force with cut length observed experimentally. **In addition, for a ship damage prediction program, a total work comparison is more useful.** Thus, the work per cut length was computed for the experimental and predicted curves. For brevity, the contributions of the steady-state cutting, transverse frame, and concertina tearing models are referred to as the damage model The comparison was started at the point where experimental data indicated steady-state cutting.

Figures 4-18 and 4-19 depict the results for Tests #1 and #2 respectively. For Test #1 , the work level predicted by the damage model at the end of the cut is 5% more than the experimental level. The work level predicted by the Kuroiwa model is 35% less than that observed experimentally at the same point. For Test #2, the damage model overestimates the work level at the end of the cut by 10%. Part of the discrepancy for this test is due to the large weld failure which occured during Test #2 as described in Section 3.2. The work level predicted by the Kuroiwa model at the end of the cut is 30% less than that observed experimentally for Test #2.

4.8.2 Comparison to the Wide Specimens

Figures 4-20 and 4-21 depict force level comparisons with Tests #3 and #4. The accuracy of the force level predictions for the three phases is similar to that

described in Section 4.6.1. The Kuroiwa Equivalent model over-predicts the peak force level by 30% for both tests.

The work per cut length comparisons provide additional insight. Figures 4-22 and 4-23 depict the results for Tests #3 and #4 respectively. For both Tests #3 and #4, the work level predicted by the combined model at the end of the cut is 5% more than the experimental level. Similarly, the work level predicted by the Kuroiwa model at the end of the cut is 50% more than that observed experimentally.

It can be concluded that the present computational model provides an excellent correlation with tests as far as the total plastic work dissipated over the length of the cut is concerned. In addition, the length of the cut is approximately equal to the prototype VLCC frame spacing scaled 1:16. Thus, the tests and model represent a cycle of a rock passing through a plating/frame unit.

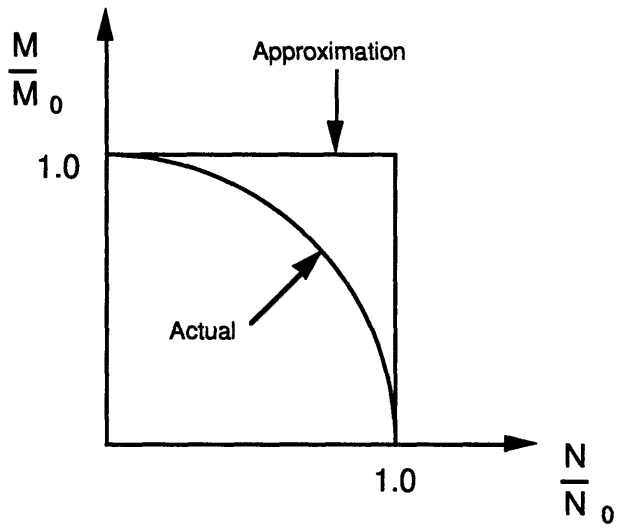

Figure 4-1. Membrane-Bending Interaction Curve Approximation

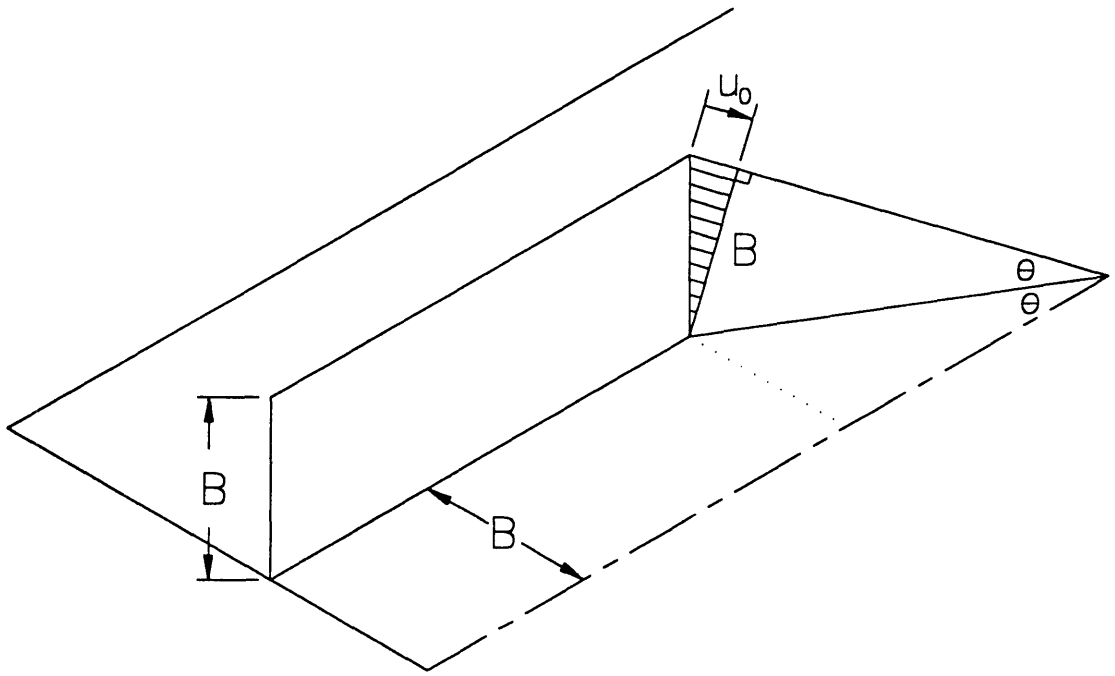

Figure 4-2. Steady-State Cutting Model
(Zheng & Wierzbicki (1994))

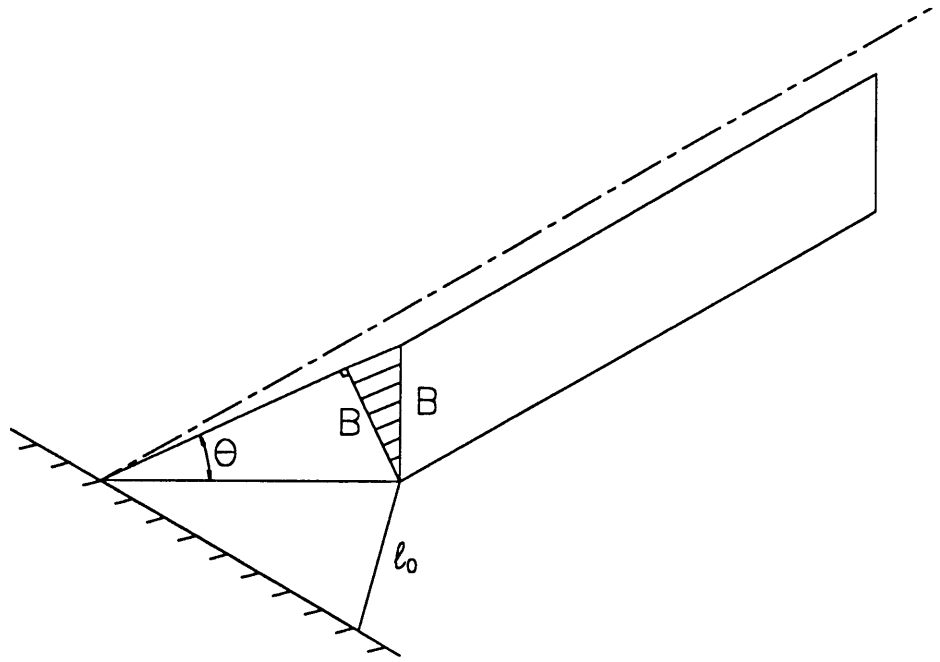

Undeformed

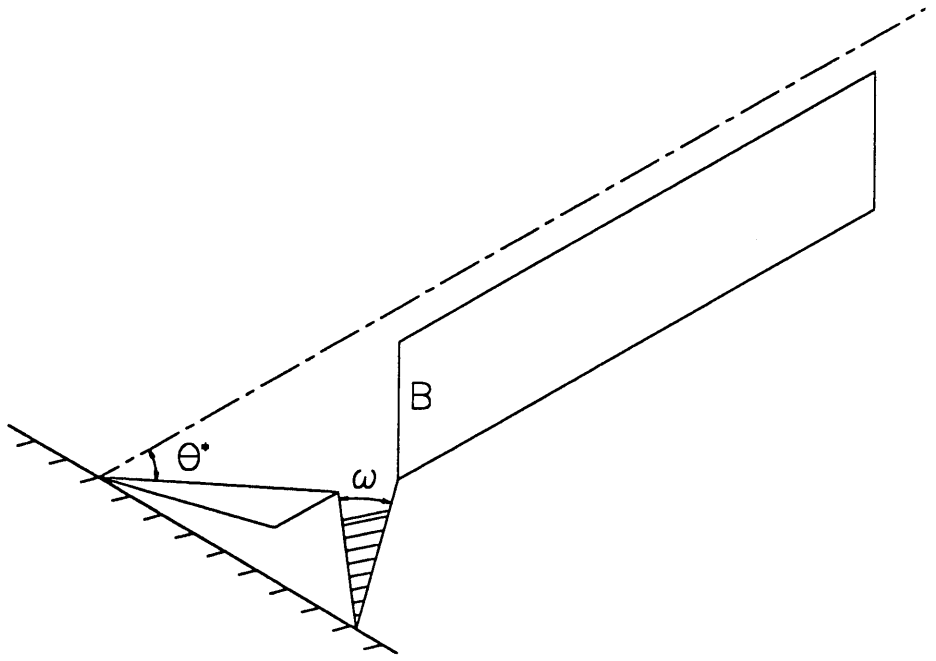

Deformed

Figure 4-3. Crack Splitting Model

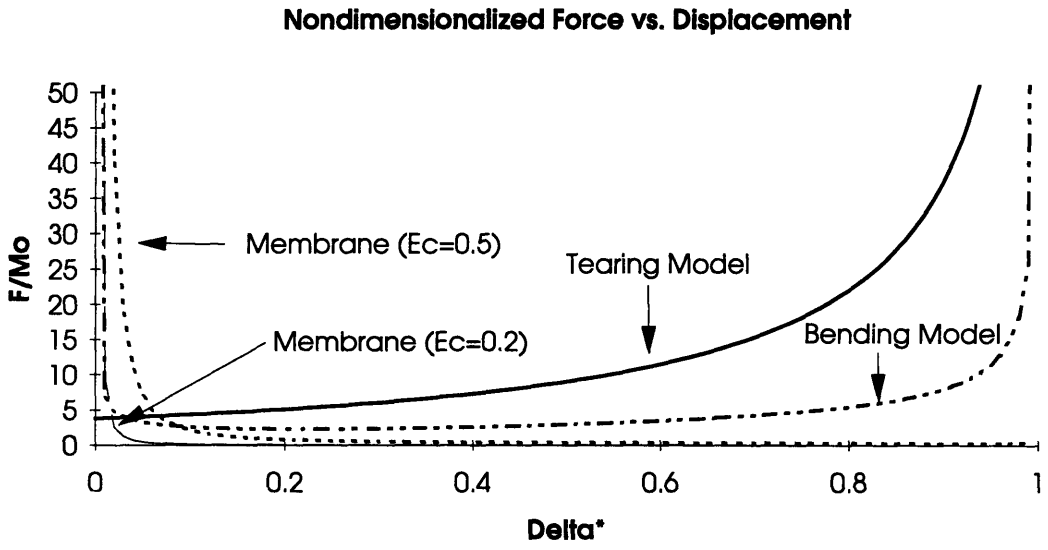

Figure 4-4. Force-Displacement Plot for Crack Splitting Model Components ($\sigma_0 = 270$ MPa)

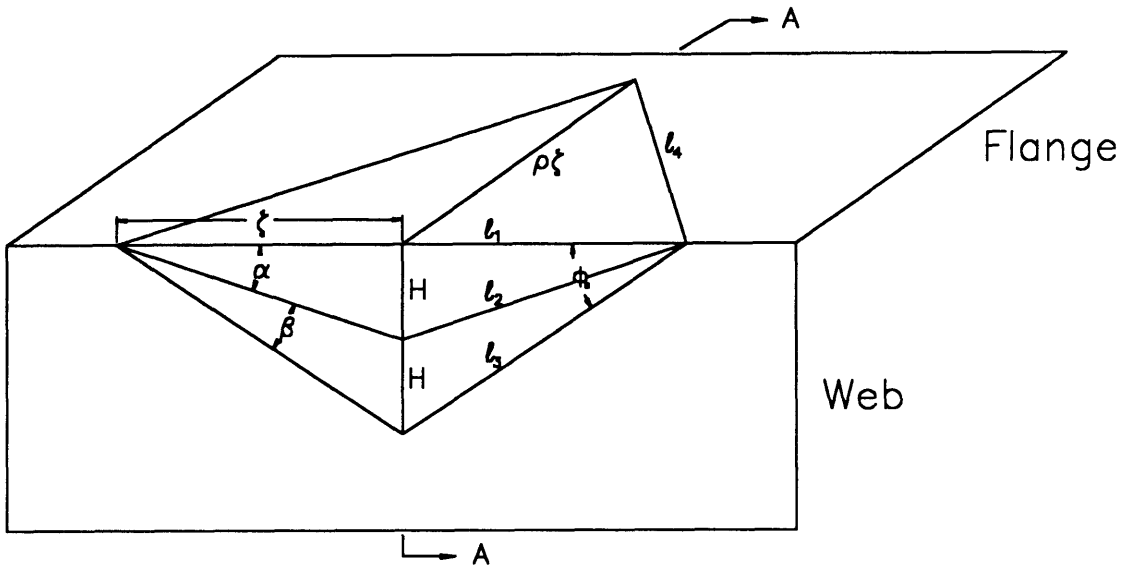

Undeformed

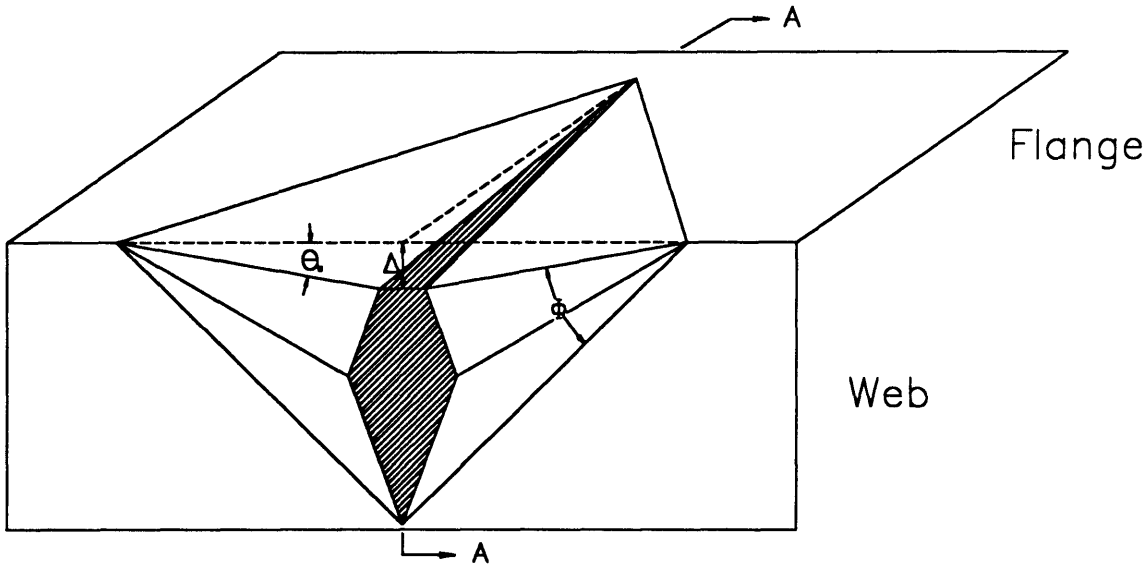

Deformed

Figure 4-5. Web Girder Crushing Model

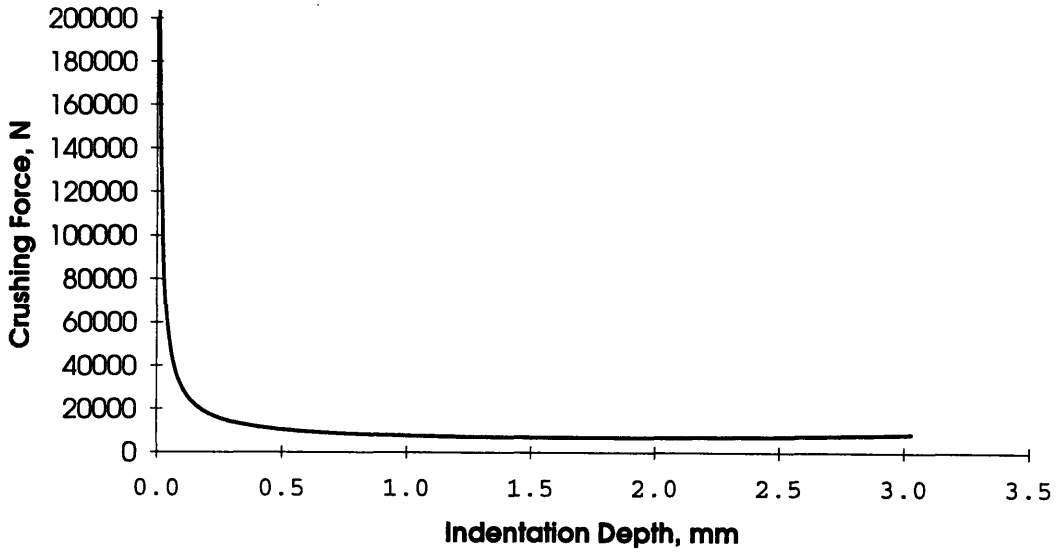

Figure 4-6. Web Girder Load-Deformation Plot for the Narrow Specimen (B/S=0.119, b_1=4.23 mm, $\sigma_0 = 270$ MPa)

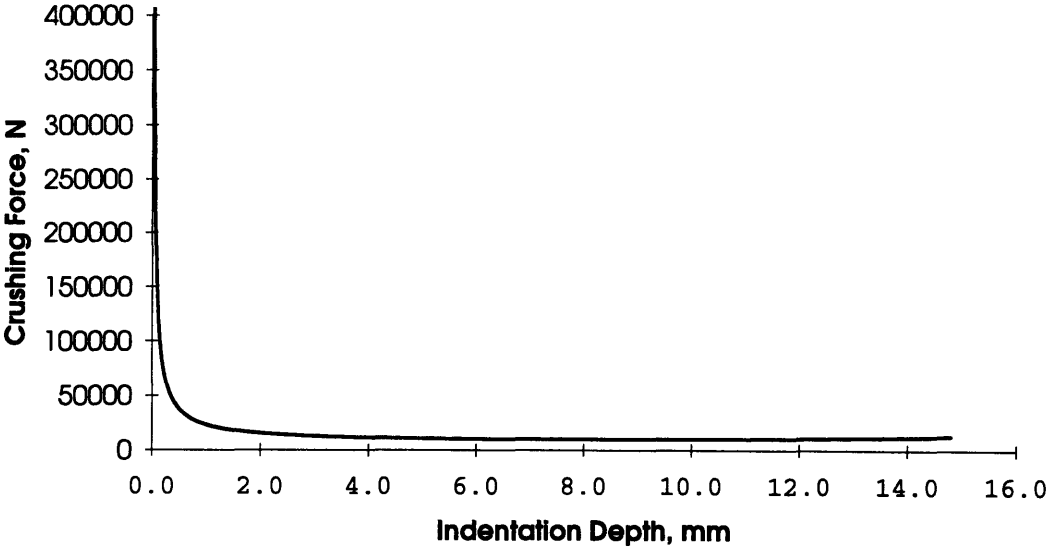

Figure 4-7. Web Girder Load-Deformation Plot for the Wide Specimen (B/S=0.238, b_1=25.4 mm, $\sigma_0 = 270$ MPa)

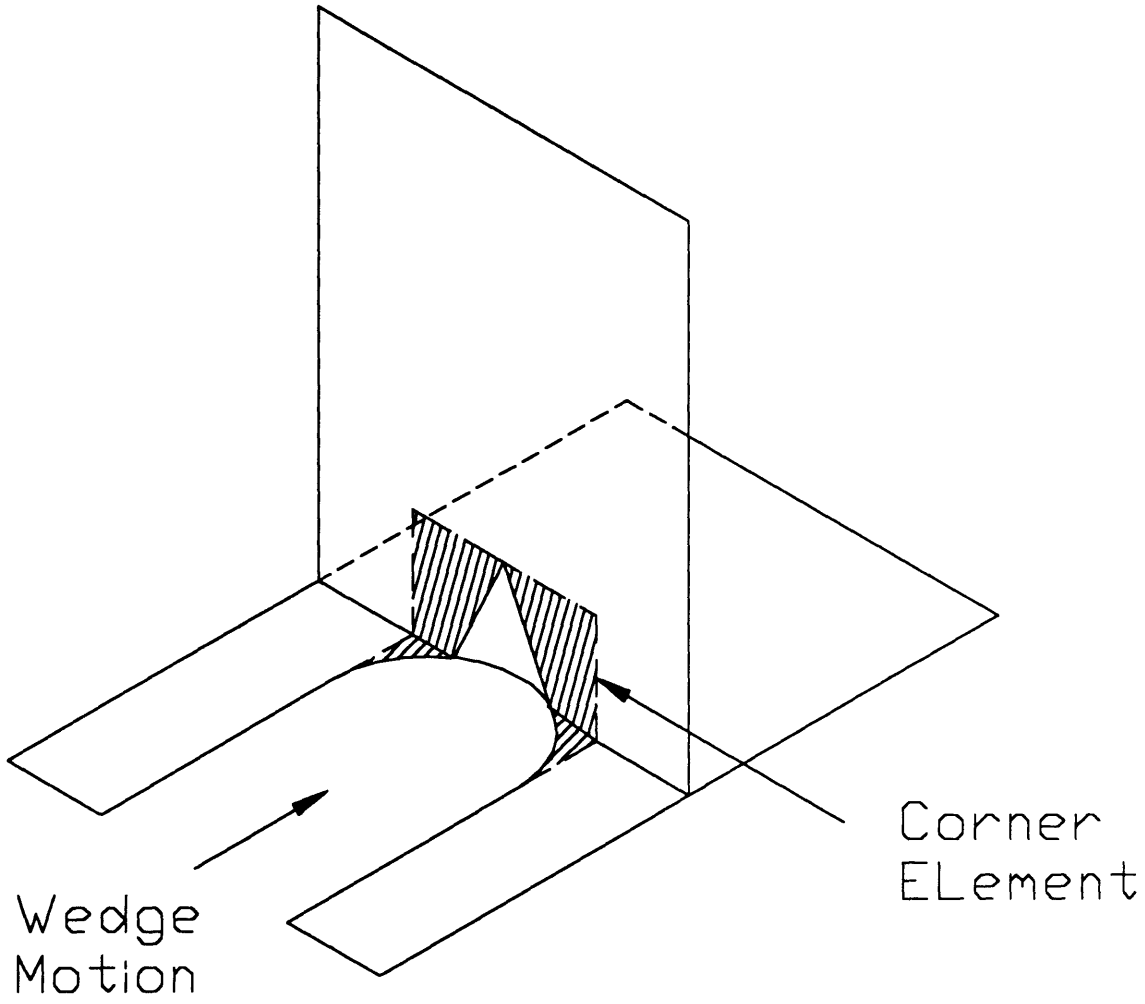

Figure 4-8. Corner Element Crushing Model

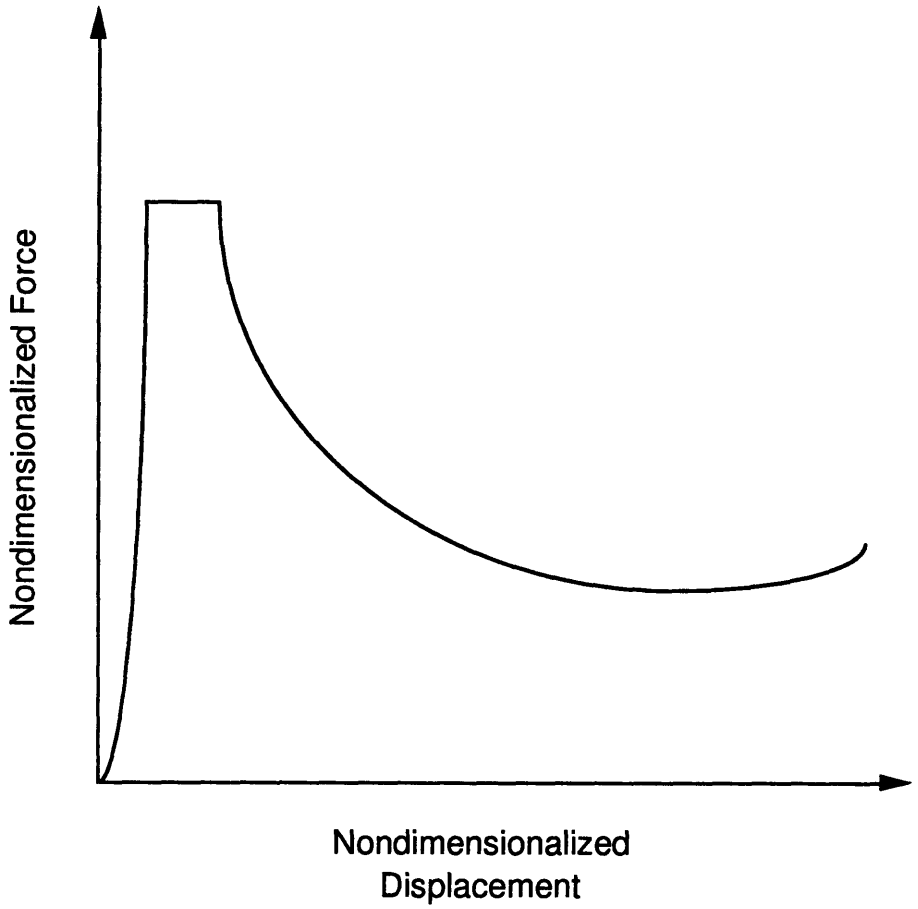

Figure 4-9. Qualitative Corner Element Crushing Load-Deformation Plot

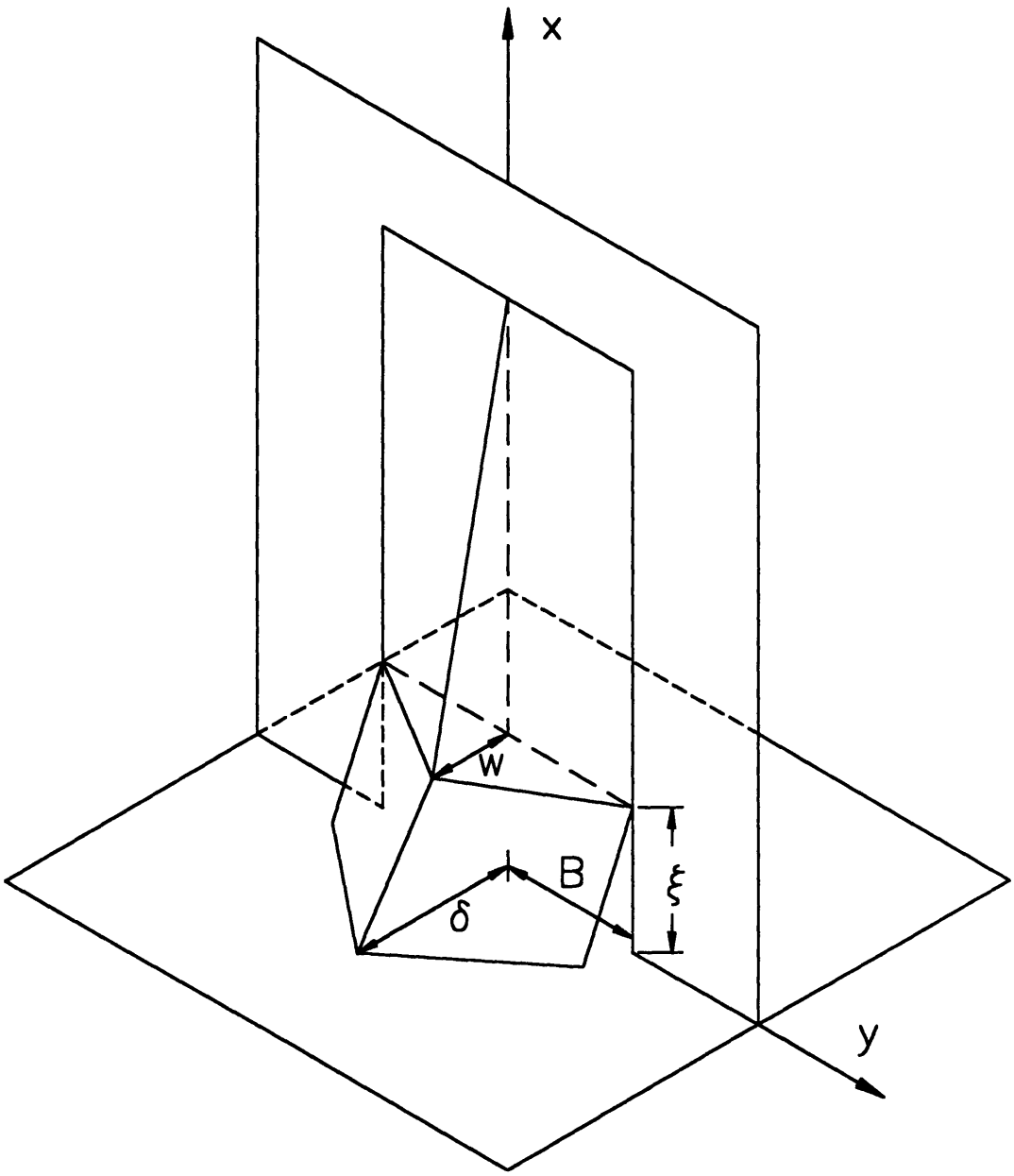

Figure 4-10. Isometric Sketch of the Frame Interaction Model

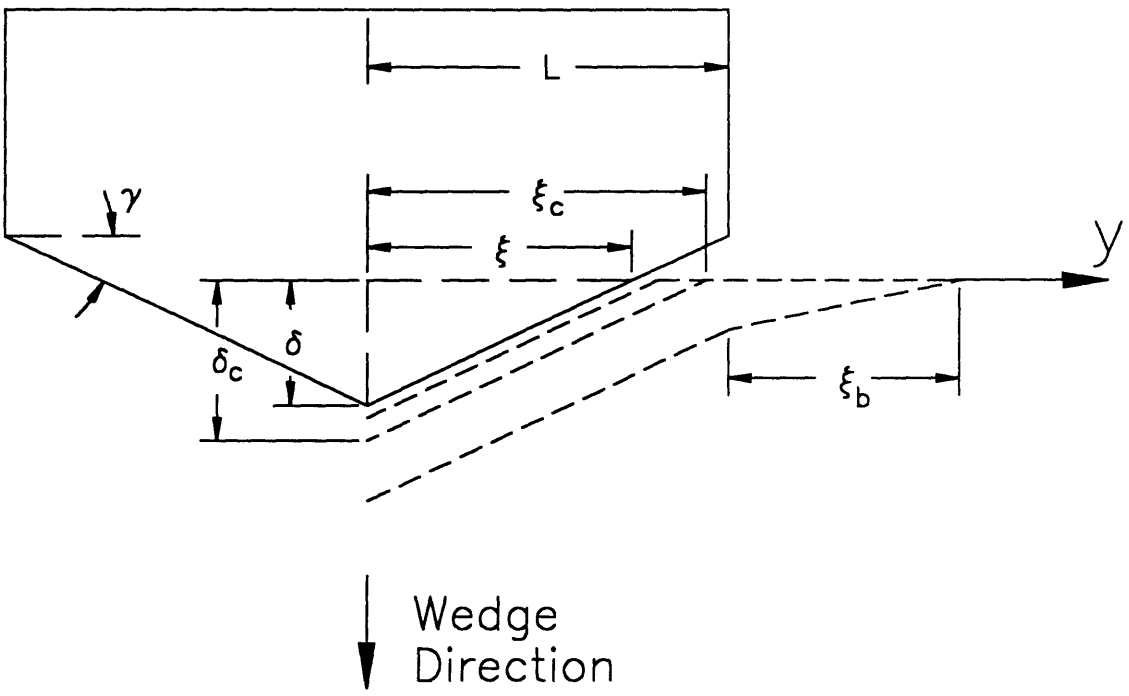

Figure 4-11. Side View of Frame Interaction Model

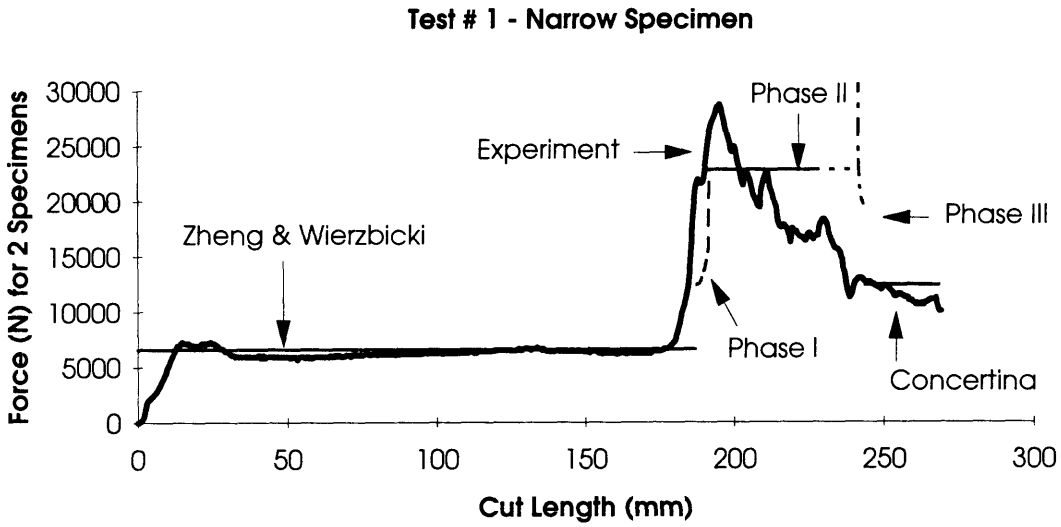

Figure 4-12. Analytical Model Comparison to Test # 1
(B/S=0.119, $\sigma_0 = 270$ MPa)

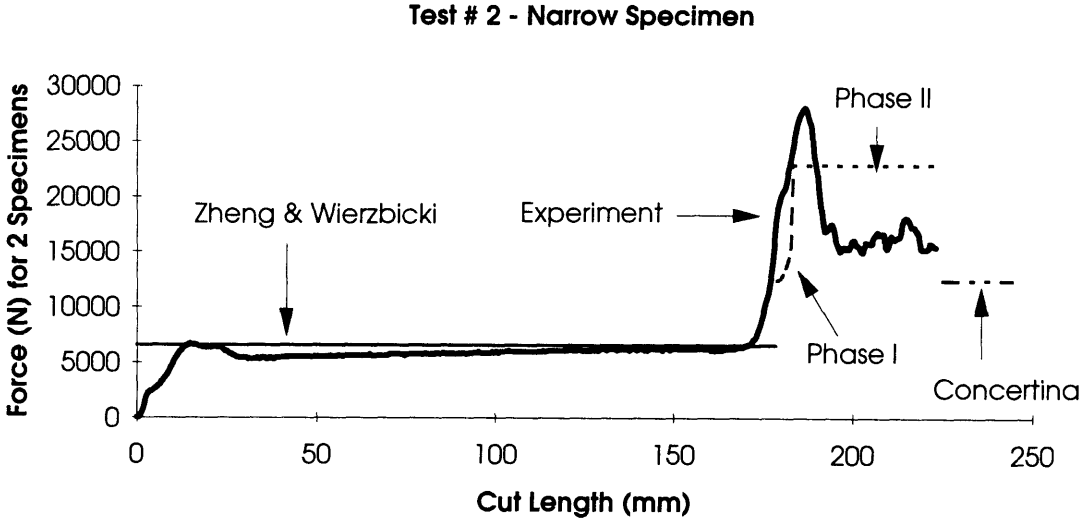

Figure 4-13. Analytical Model Comparison to Test # 2
(B/S=0.119, $\sigma_0 = 270$ MPa)

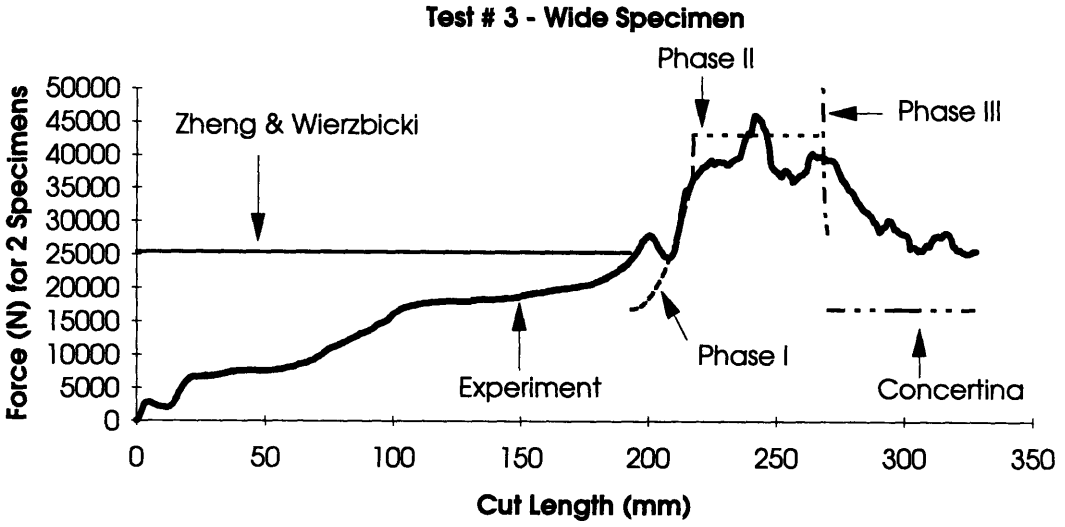

Figure 4-14. Analytical Model Comparison to Test # 3
(B/S=0.238, $\sigma_0 = 270$ MPa)

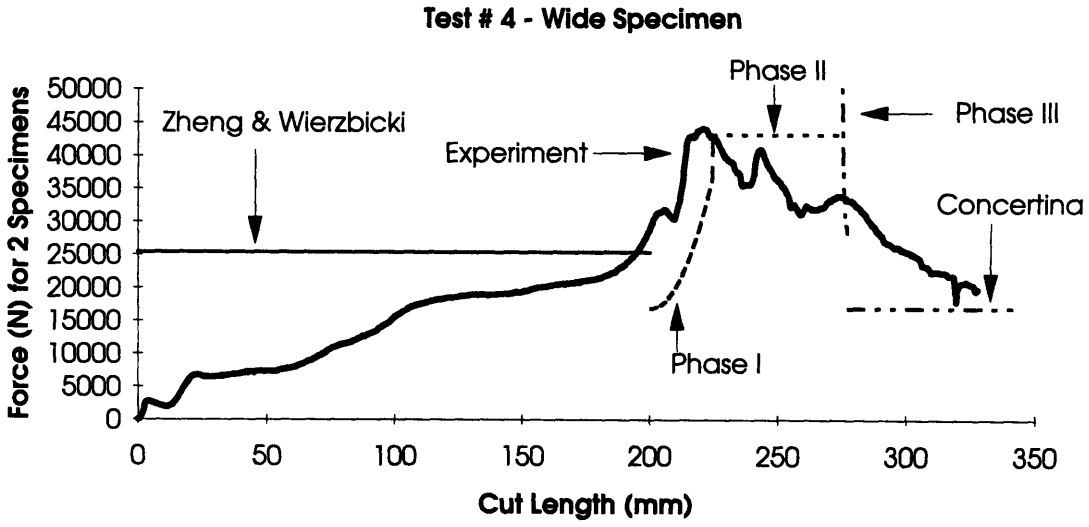

Figure 4-15. Analytical Model Comparison to Test # 4
(B/S=0.119, $\sigma_0 = 270$ MPa)

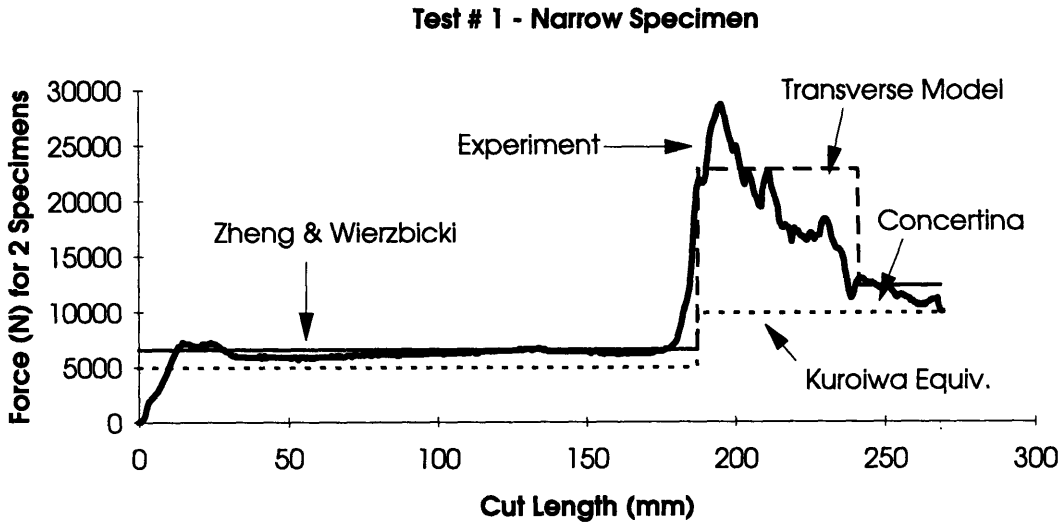

Figure 4-16. Damage Prediction Model Force Comparison to Test # 1 (B/S=0.119, $\sigma_0 = 270$ MPa, $\sigma_Y = 215$ MPa)

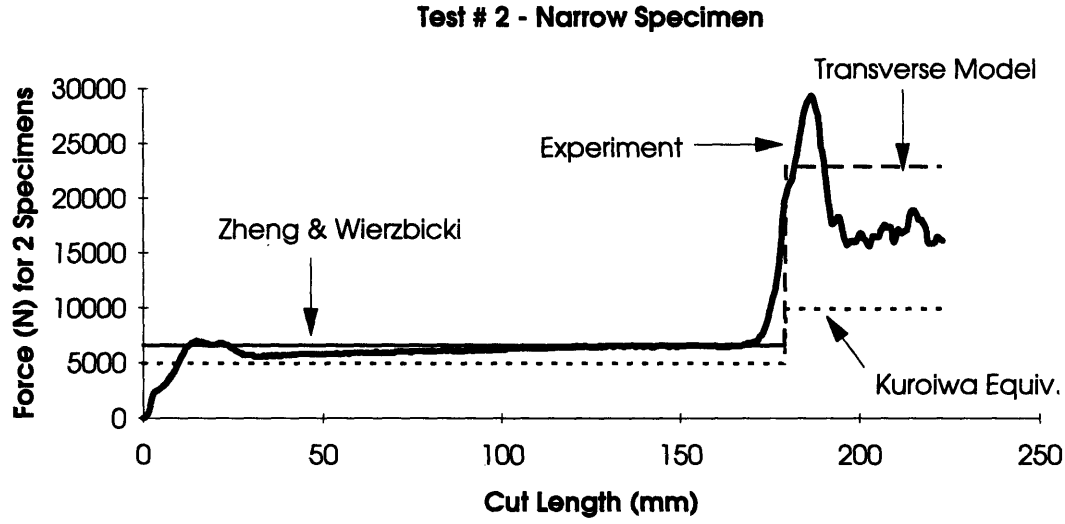

Figure 4-17. Damage Prediction Model Force Comparison to Test #2 (B/S=0.119, $\sigma_0 = 270$ MPa, $\sigma_Y = 215$ MPa)

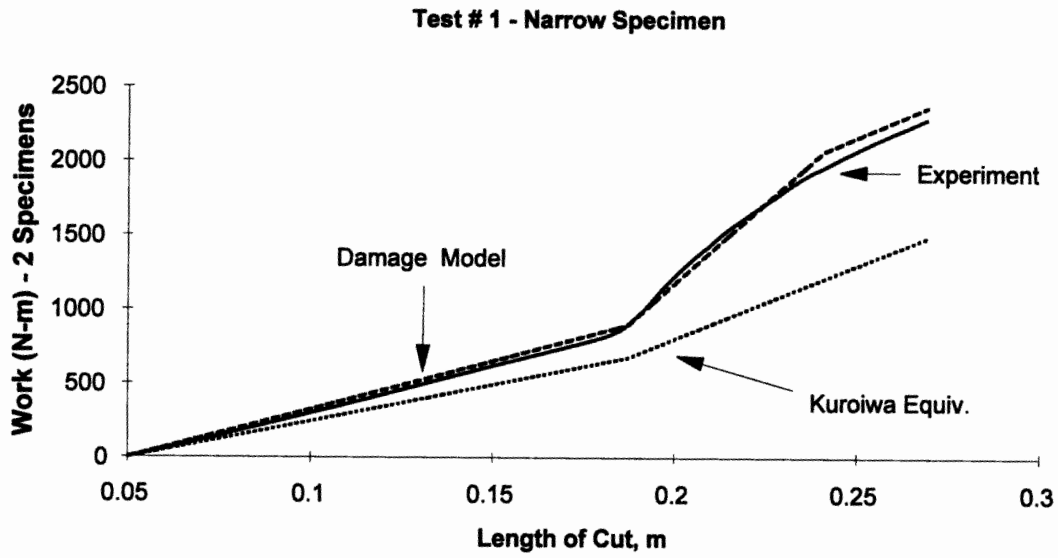

Figure 4-18. Damage Prediction Model Work Comparison to Test # 1

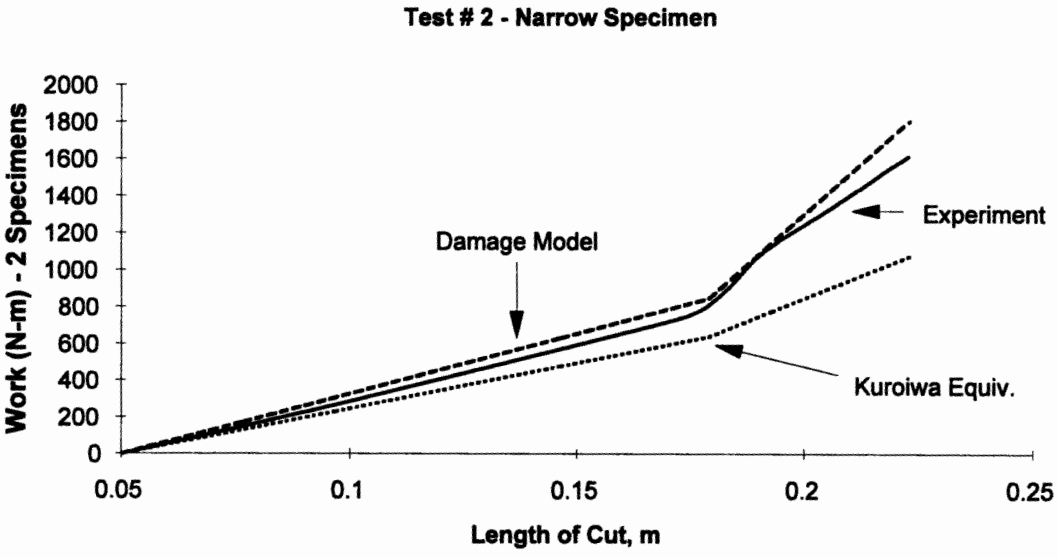

Figure 4-19. Damage Prediction Model Work Comparison to Test # 2

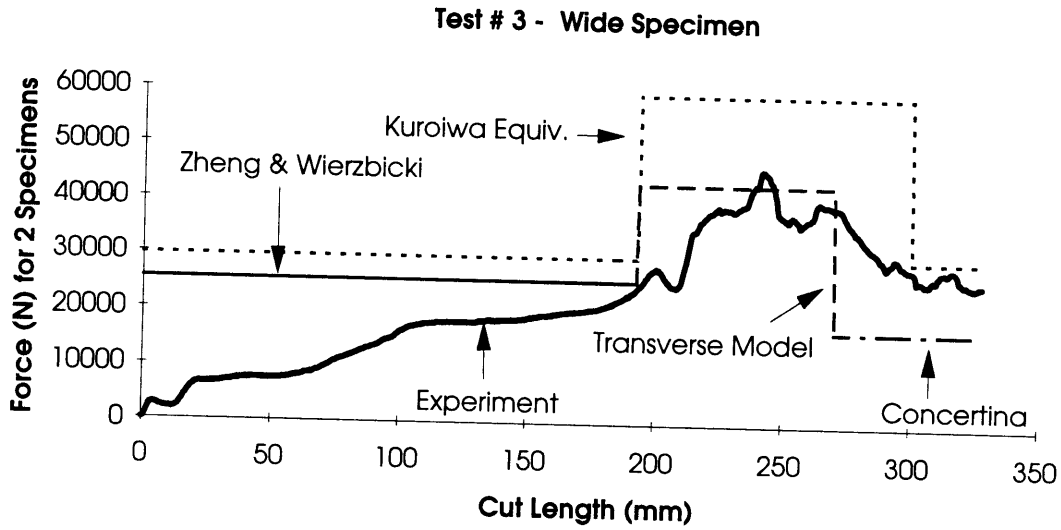

Figure 4-20. Damage Prediction Model Force Comparison to Test # 3 (B/S=0.238, $\sigma_0 = 270$ MPa, $\sigma_Y = 215$ MPa)

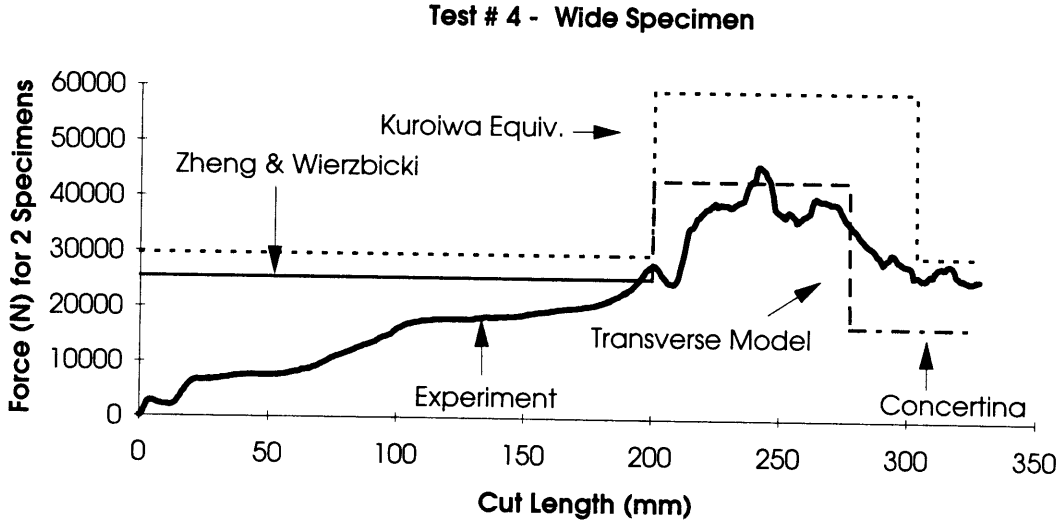

Figure 4-21. Damage Prediction Model Force Comparison to Test #4 (B/S=0.238, $\sigma_0 = 270$ MPa, $\sigma_Y = 215$ MPa)

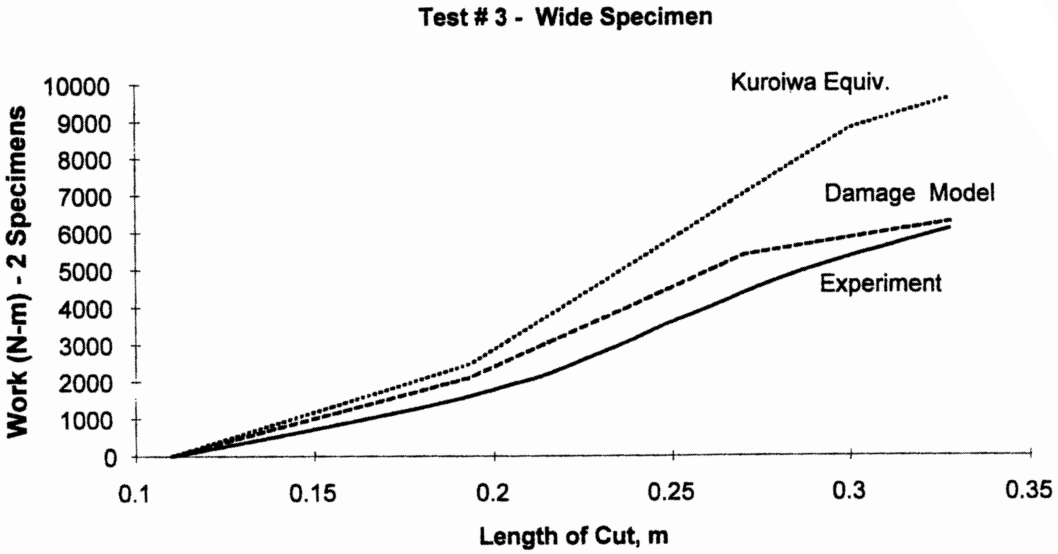

Figure 4-22. Damage Prediction Model Work Comparison to Test # 3

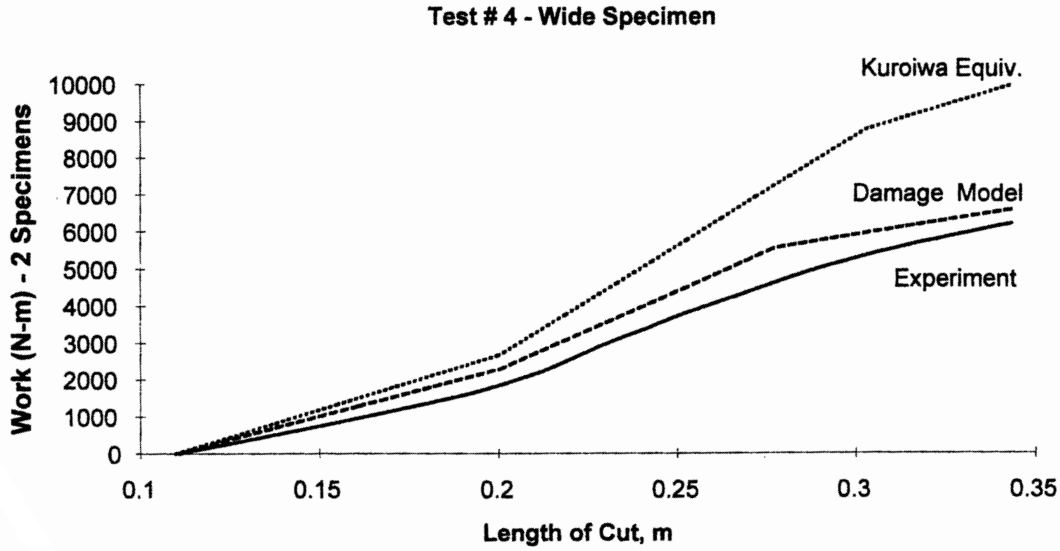

Figu 4-23. Damage Prediction Model Work Comparison to Test # 4

5.0 - Conclusions and Recommendations

5.1 Conclusions

The experimental design of the specimens and testing apparatus was a success. A ship structure was modeled on a small scale (1:16), including details such as a transverse frame and its associated longitudinal supports. The inclusion of transverse stiffening with reasonable boundary conditions represented an advance in the study of plate cutting mechanics.

Two types of specimens were tested: a narrow specimen with a ratio of wedge half width to support spacing of B/S = 0.119 and a wide specimen with a B/S of 0.238. The narrow and wide transversely stiffened specimen tests provide a basis for decomposing the steady-state grounding process into several stages. These include the pre-frame , the frame interaction and the post-frame stages.

(1) For the narrow specimen, the pre-frame phase cutting force level was predicted by Zheng and Wierbicki's steady-state cutting model to within 5%. The wide specimen pre-frame phase cutting force level was calculated by Zheng and Wierbicki's steady-state cutting model with 10% error.

(2) A sudden rise in force occurred as the wedge approached within seven to ten times the plating thickness of the transverse member for both types of specimens. This marked the start of the frame interaction stage. A stiffening model, applicable for circular wedge faces, was developed which showed the steep rise in force.

(3) The magnitude of peak force was shown to be a result of a number of factors, the most important being the compression of corner elements.

(4) A three-phase model of the frame interaction stage was developed which neglected the initial stiffening and peak load effects, . The phases were: pre-rupture, rupture and decay. The model underestimated the narrow specimen peak load by 20% and the wide specimen peak load by 5%.

(4) The post-decay period was bounded by concertina tearing and steady-state cutting.

The frame interaction stage model was further simplified for use in a ship damage prediction computer program. The simplification was accomplished by ignoring the effects of the pre-rupture and decay phases, and extending the rupture phase from the point of wedge contact with the transverse frame to the end of the interaction. It is referred to as the transverse model. The transverse model was coupled with the steady-state cutting and concertina tearing models to form a damage prediction model.

The accumulated work per length of cut predicted by the damage prediction model was compared to that **observed experimentally with excellent results**. For the narrow specimens, the combined model predicted the observed work level to within 10% at the end of the cut. For the wide specimens, the damage model predicted the observed work level to within 5% at the end of the cut. In contrast, a raking force prediction model based upon the volume of damage material was shown to underestimate the work at the end

of the cut by 20% for the narrow specimen and overestimate the work by 50% for the wide specimen, even though the volume of the damaged transverse member was included.

5.2 Suggestions for Future Work

There is much additional work to be done with both the experimental and theoretical aspects of the transversely stiffened plate.

(1) The analytical model for the stiffening due to crack divergence is valid for a wedge with a circular face with a radius to wedge width ratio of 0.5. This should be expanded to include additional types of wedge geometry (i.e. sharp wedge). Additional experiments with different types of wedge geometry should be done to support this.

(2) Additional work is required to predict the peak force as the wedge passes through the corner element. Including the corner element crushing contribution is a logical first step in the process.

(3) Similarly, the decay phase of the frame interaction model was a simple approximation. A more detailed modeling of this phase may improve the overall accuracy of the frame interaction model force level prediction.

(4) Conduct tests on the orthogonally stiffened transverse specimens in order to observe the effect the inclusion of longitudinal stiffeners has on the observed deformation modes.

(5) The scaling laws developed for the small-scale testing must be validated for the case of full size ships. Different scaling laws hold in tension and bending, as well as for crack initiation and steady growth. In addition, material properties vary with thickness.

References

Abramowicz, W. and T. Wierzbicki. 1989. "Axial Crushing of Multicorner Sheet Metal Columns." *Journal of Applied Mechanics* 56:113.

Akita, Y. and K. Kitamura. 1972. "A Study on Collision of Elastic Stem to a Side Structure of Ships." *Journal of Society of Naval Architects of Japan* 131 : 307-317.

Bracco, M.D. 1994. *A Study of the Wedge Cutting Force Through Longitudinally Stiffened Plates: An Application to Grounding Resistance of Single and Double Hull Ships* M.Sc. Thesis, Department of Ocean Engineering, M.I.T.

Card, J.C. 1975. "Effectiveness of Double Bottoms in Preventing Oil Outflow From Tanker Bottom Damage Incidents." *Marine Technology* 12 : 60-64.

Calladine, C. 1985. *Plasticity for Engineers.* Chichester, England: Ellis Horwood Ltd.

Choi, S., T. Wierzbicki, and J. Culbertson-Driscoll. 1994. *Crushing Strength of Web Girders.* Technical Report No. 23, Joint MIT-Industry Program in Tanker Safety.

Jones, N., W.S. Jouri, and R.S. Birch. 1984. "On the Scaling of Ship Collision Damage." *Proceedings of 3rd International Congress on Marine Technology.* pp. 287-294 Athens International Maritime Association of East Mediterranean. Phivos Publishing Co. Greece.

Jones, N, and W.S. Jouri. 1987. "A Study of Plate Tearing for Ship Collision and Grounding Damage." *Journal of Ship Research* 31 : 253-268.

Kuroiwa, T., Y. Kawamoto and T. Yuhara. 1992. "Study on Damage of Ship Bottom Structures due to Grounding." *Conference on Marine Safety and Environment/Ship Production*, June 1-4. Delft, The Netherlands.

Lu, G. and C.R. Calladine. 1990. "On the Cutting of a Plate by a Wedge." *International Journal of Mechanical Sciences* 32 : 293-313.

Maxwell, L.M. 1993. *Effect of Rock Geometry on the Failure Mode of Plates and the Forces in Grounding Experiments.* M.Sc. Thesis, Department of Ocean Engineering, M.I.T.

McClintock, F.A. 1994. *Fully Plastic Mechanics for Welded T-Joints.* Technical Report No. 26, Joint MIT-Industry Program in Tanker Safety.

Minorsky, V.U. 1959. "An Analysis of Ship Collisions with Reference to Protection of Nuclear Power Plants." *Journal of Ship Research* 3 : 1-4.

Paik, J.K. 1994. "Cutting of a Longitudinally Stiffened Steel Plate by a Rigid Wedge." Accepted for publication in *Journal of Ship Research.*

Vaughn, H. 1977. "Damage to Ships Due to Collision and Grounding." Det norske Veritas, DnV 77-345.

Vaughn, H. 1978. "Bending and Tearing of Plate with Application to Ship-Bottom Damage." *The Naval Architect* May: 97-99.

Vaughn, H. 1980. "The Tearing Strength of Mild Steel Plate." *Journal of Ship Research* 24 : 96-100.

Wierzbicki, T. 1993. *Concertina Tearing of Metal Plates.* Technical Report No. 12, Joint MIT-Industry Program in Tanker Safety.

Wierzbicki, T. 1994 *Concertina Tearing of Metal Plates: Improved Solution and Comparison with Experiments.* Technical Report No. 22, Joint MIT-Industry Program in Tanker Safety.

Wierzbicki, T. and W. Abramowicz. 1983. "On Crushing Mechanics of Thin-walled Structures." *Journal of Applied Mechanics* 5: 727-734.

Wierzbicki, T., E. Rady, D. Peer, and J.G. Shin. 1990. *Damage Estimates in High Energy Grounding of Ships.* Technical Report No. 1, Joint MIT-Industry Program in Tanker Safety.

Wierzbicki, T., L. Recke, W. Abramowicz and T.Gholami. 1994. "Stress Profiles in Thin-walled Prismatic Columns Subjected to Crush Loading, Part I Compression." Accepted for publication in *Computers and Structures.*

Wierzbicki, T., L. Recke, W. Abramowicz and T.Gholami. 1994. "Stress Profiles in Thin-walled Prismatic Columns Subjected to Crush Loading, Part II Bending." Accepted for publication in *Computers and Structures.*

Wierzbicki, T. and P.F. Thomas. 1993. "Closed Form Solution for Wedge Cutting Force Through Thins Metal Sheets." *International Journal of Mechanical Science* 35 : 209-229.

Woisin, G. 1982. "Comments of Vaughn: The Tearing of Mild Steel Plates." *Journal of Ship Research* 26 : 50.

Yahiaoui, M., M. Bracco, P. Little, and K. Trauth. 1994. *Experimental Studies on Scale Models for Grounding.* Technical Report No. 18, Joint MIT-Industry Program in Tanker Safety.

Zheng, Z. and T. Wierzbicki. 1994. *A Theoretical Analysis of a Steady-State Wedge Cutting Through Metal Plates.* Technical Report No. 19, Joint MIT-Industry Program in Tanker Safety.

Appendix A - Testing Equipment Information

A.1 Testing Equipment Description

The Instron machine used for all testing was a 20,000 lb, screw-driven, universal testing machine. A 386 personal computer with a National Data Acquisition software package was used to process the output data from the tests. Figure A-1 depicts the Instron machine and computer set-up. The cross-head speed for all tests was set at 1 inch per minute. A sampling rate of 40 samples per minute was used by the software package. The 40 samples were subsequently averaged and recorded to provide a single data point each second

A.2 Testing Instructions

The following is a sequence of instructions to be followed in order to use the equipment for testing.

1. Turn of the machine and allow it to warm up for at least 30 minutes prior to testing. The machine is turned on by flipping the AMPLIDYNE and MAIN POWER switches to ON. In addition, ensure the front panel settings are:

   a. Load Cell: CT-G
   b. Marker Control: MANUAL
   c. Zero Suppression Control: OUT (both)
   d. Range: 10
   e. X-Y Chart Drive Amp: OFF
   f. Limit Cycle: OFF

g. Cycle Control: Manual.

2. Ensure the voltmeter is set to AC with the scale on 10 V. It should be plugged into the receptacle labeled '1 Hz Filter' above the control panel. This is the same receptacle the data acquisition wire is connected to.

3. Check the calibration of the machine as follows:

a. Adjust the pen control until the chart recorder pen is in the middle of the chart. Press the ZERO button. Adjust the balance control until there is no movement of the pen when the ZERO button is pressed. At that point, adjust the pen control until the pen trace is at the right edge of the chart paper scale.

b. Set the full scale load to 500. Press the CALIBRATION button. The pen should travel to the left edge of the chart paper scale. Adjust the calibration control until pressing the CALIBRATION button provides the full scale deflection of the chart pen. When achieved, recheck the zero.

c. Set the full scale load to 1000. Press the CALIBRATION button. The chart pen should deflect to half scale. Adjust as needed. Recheck the zero and adjust as required.

d. Set the full scale load to 2000. Press the CALIBRATION button. The chart pen should deflect to one-quarter scale. Adjust as needed. Recheck the zero and adjust as required.

e. Set the full scale load to 5000. Press the CALIBRATION button. The chart pen should deflect to one-eighth scale. Adjust as needed. Recheck the zero and adjust as required.

f. Set the full scale load to 10000. Press the CALIBRATION button. The chart pen should deflect to one-tenth scale. Adjust as needed. Recheck the zero and adjust as required.

4. Adjust the pen control so the chart pen is on the left edge of the chart paper scale. Record the corresponding 'zero' voltmeter reading. Press the CALIBRATION button Record the corresponding 'full scale' voltmeter reading.

5. Set up the data acquisition software:

a. Open dos_data_aq located in the NI-DAQ window. The screen will indicate: BOARD: Number 1, BOARD USED: Lab-PC. From the toolbar across the top, select INSTRUMENTS. Under this, select STRIP CHART AND DATA LOGGER. You now have the data acquisition control screen.

b. Set the values for YMAX and YMIN to 0.1 and -0.5 respectively. These can be adjusted on subsequent tests if the screen scale is inadequate. Click OK.

c. Ensure that CONSECUTIVE is selected.

d. Click on SAVE TO FILE. The dot next to it should illuminate green.

e. Click CHAN SETUP. In the new window, change "CHANNEL 0" to "LOAD CELL". Click OK.

f. Change SAMPLE RATE to 40. Change AVERAGE to 40. Click the box next to the word AVERAGE.

6. You are ready for testing. Ensure the cross-head speed is set to 1 inch per minute. Double check to ensure everything is tightened. Click on the START/STOP button on the computer screen, then press UP on the Instron machine.

7. When the test is complete, push STOP on the Instron machine and press ENTER on the keyboard. Type in an appropriate file name and click OK to save

the data to a file. Click on RETURN and select QUIT from the toolbar to end the application.

8. Disassemble the testing apparatus as required.

9. Import the testing data into Microsoft WORD.

a. Start the WORD application

b. Select OPEN under the FILE menu

c. Change back to the root directory (C:\).

d. Choose NIDAQDOS, then DAQWARE.

e. List files of type *.txt.'

f. Select the file name the data is saved under. Click OK when the CONVERT window comes up.

10. Process the data.

a. Delete the top few lines and all the extra zeroes except for one.

b. Under the EDIT menu, choose SELECT ALL.

c. Under the TABLE menu, choose CONVERT TEXT TO TABLE

d. Mark the right-hand column and choose DELETE under the TABLE menu.

e. Choose SELECT ALL, then COPY under the EDIT menu

f. Exit WORD but do not save the changes!

11. Import the data into Microsoft EXCEL.

a. Start the EXCEL application.

b. Under the FILE menu, select OPEN. Choose the file TEMPLATE.XLS.

c. Locate the cursor on the first zero in the data column. Select PASTE from the EDIT menu.

d. Modify the graphs and entering arguments in the spreadsheet as appropriate.

e. Save the file under a new name.

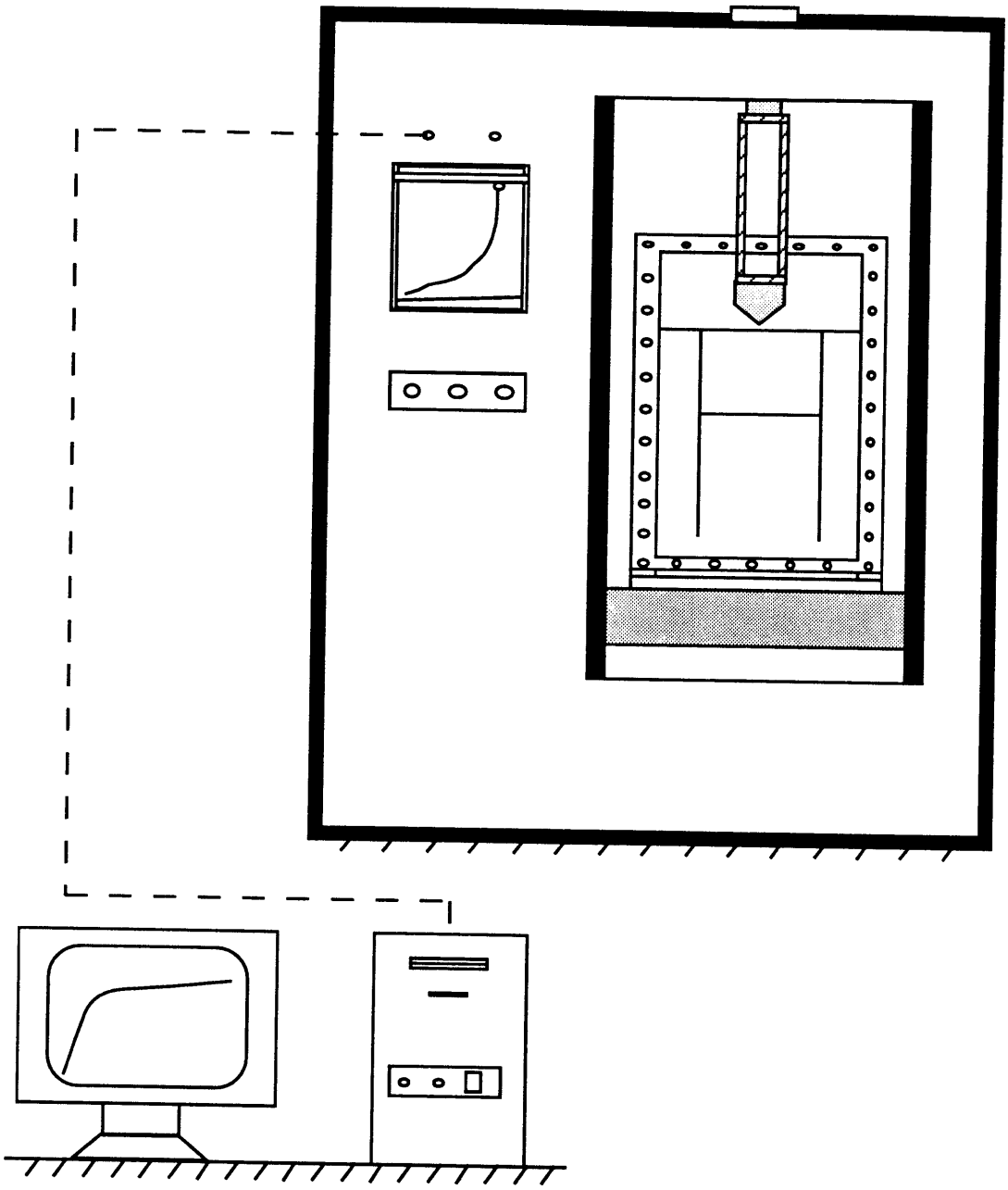

Figure A-1. Testing Machine and Data Acquisition Unit

Appendix B - Experimental Fabrication Details

B.1 General Information

This appendix provides detailed information on the fabrication of the specimens and wedges used in the experiments described in this thesis. All specimens were constructed from ASTM A366 steel. Unless otherwise noted, welds were done using the electron beam welding (EBW) process by the *Applied Energy Company* of Winchester. MA. The fillet welds on the orthogonally stiffened specimens were done by the Nuclear Engineering Shop at MIT.

The wedges were machined from cold finished mild steel and surface hardened to a depth of 0.030 inches using a cyanide solution at 1650°F. The surface hardening was done by *Bomak Corporation* of Woburn, MA. The longitudinal support brackets were constructed from 1 inch x 6 inch 6061-T6 aluminum stock. All machine work was done by Mr. Arthur Rudolph of the Civil Engineering Machine Shop at MIT.

B.2 Construction Drawings

Construction drawings for the specimens, wedges and brackets are included in this appendix.

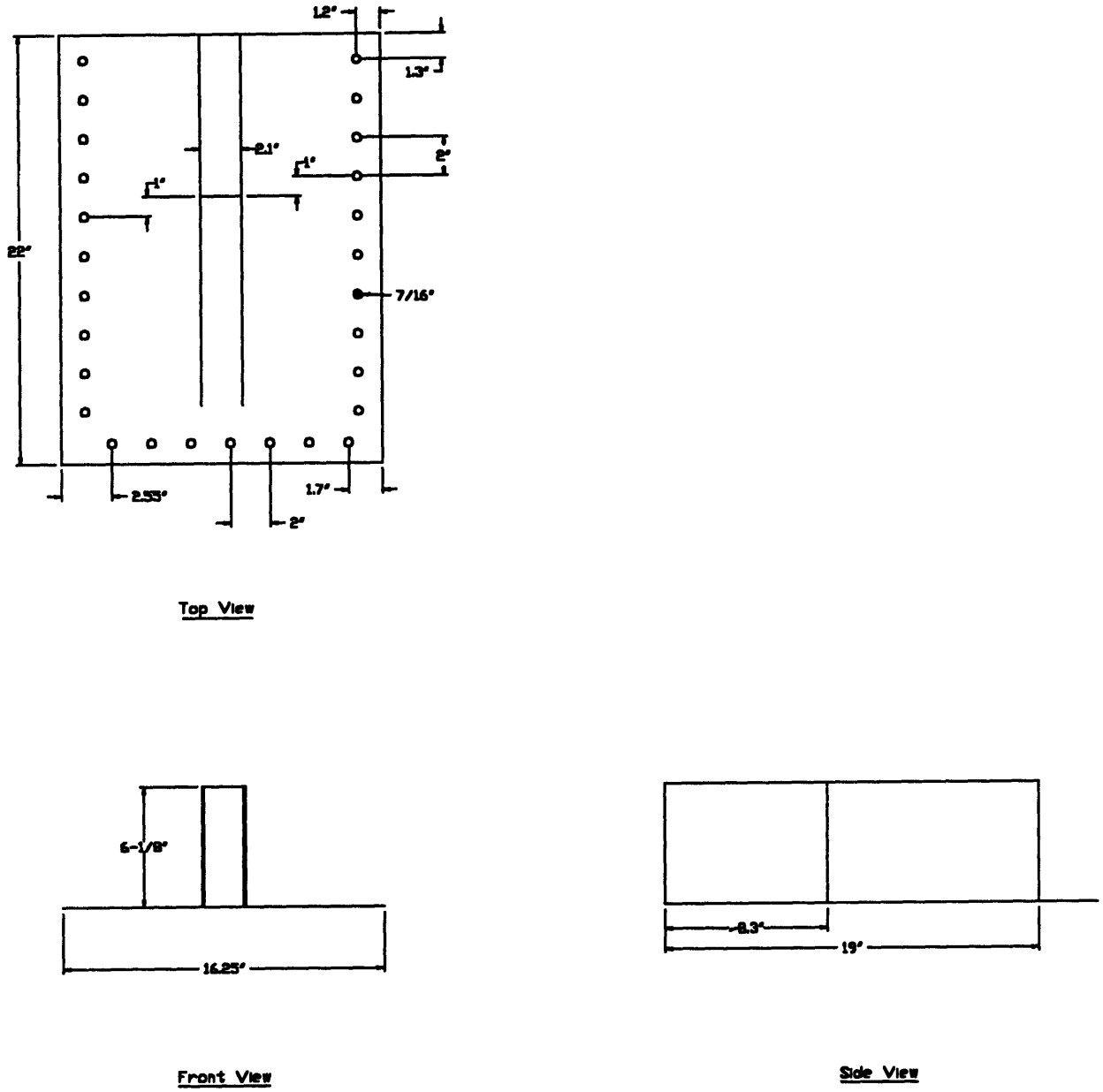

Figure B-1. Narrow Transversely Stiffened Specimen Construction Drawing

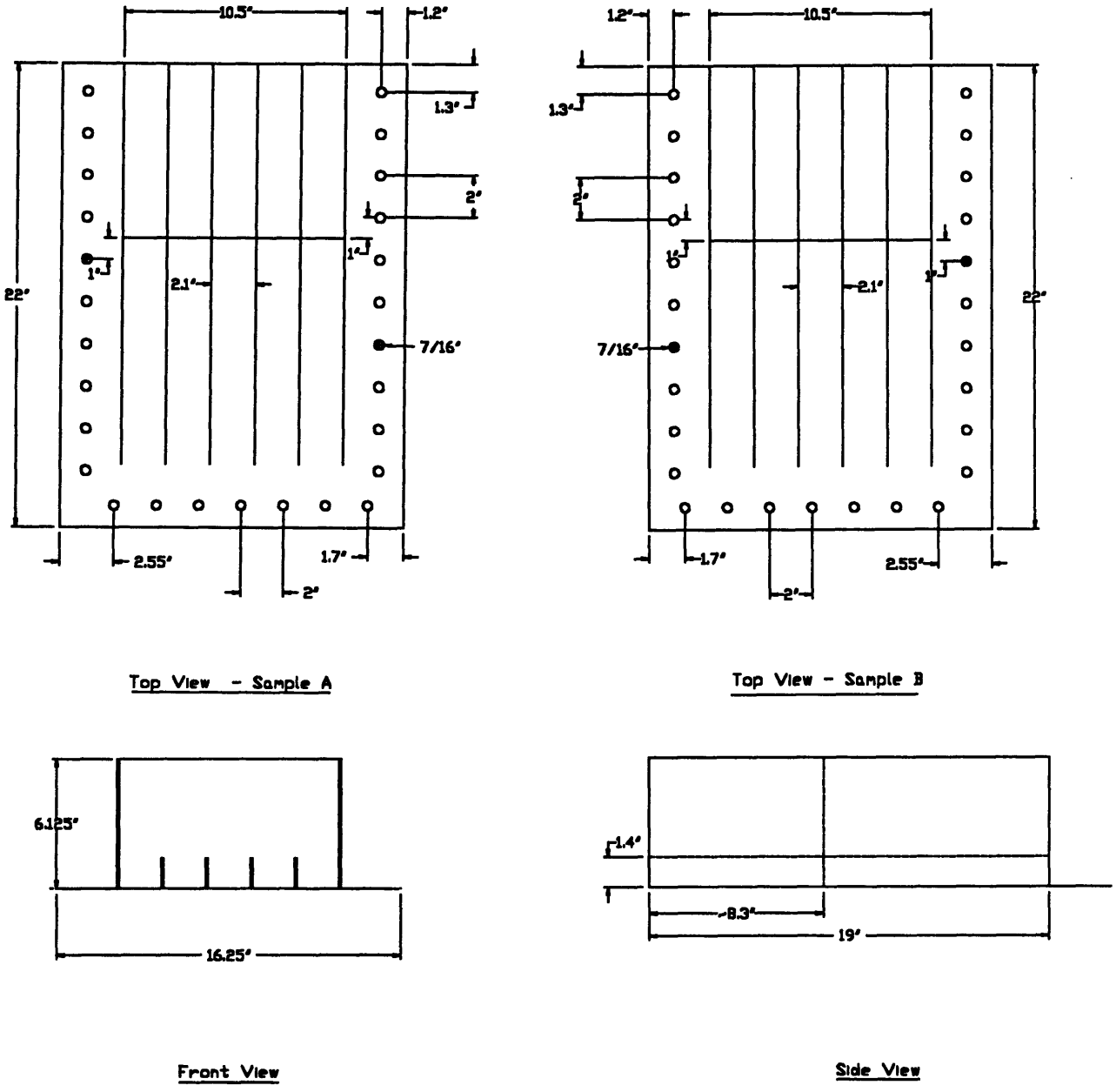

Figure B-2. Wide Transversely Stiffened Specimen Construction Drawing

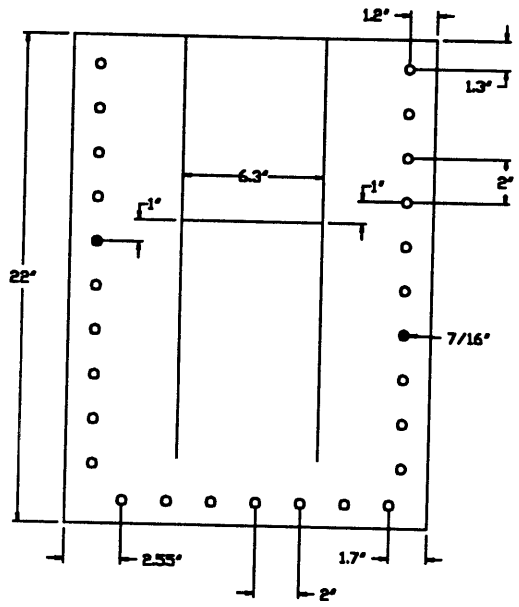

Top View

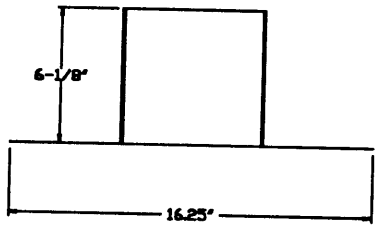

Front View

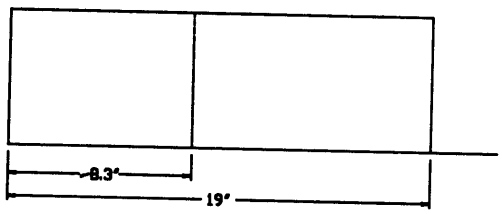

Side View

Figure B-3. Orthogonally Stiffened Specimen Construction Drawing

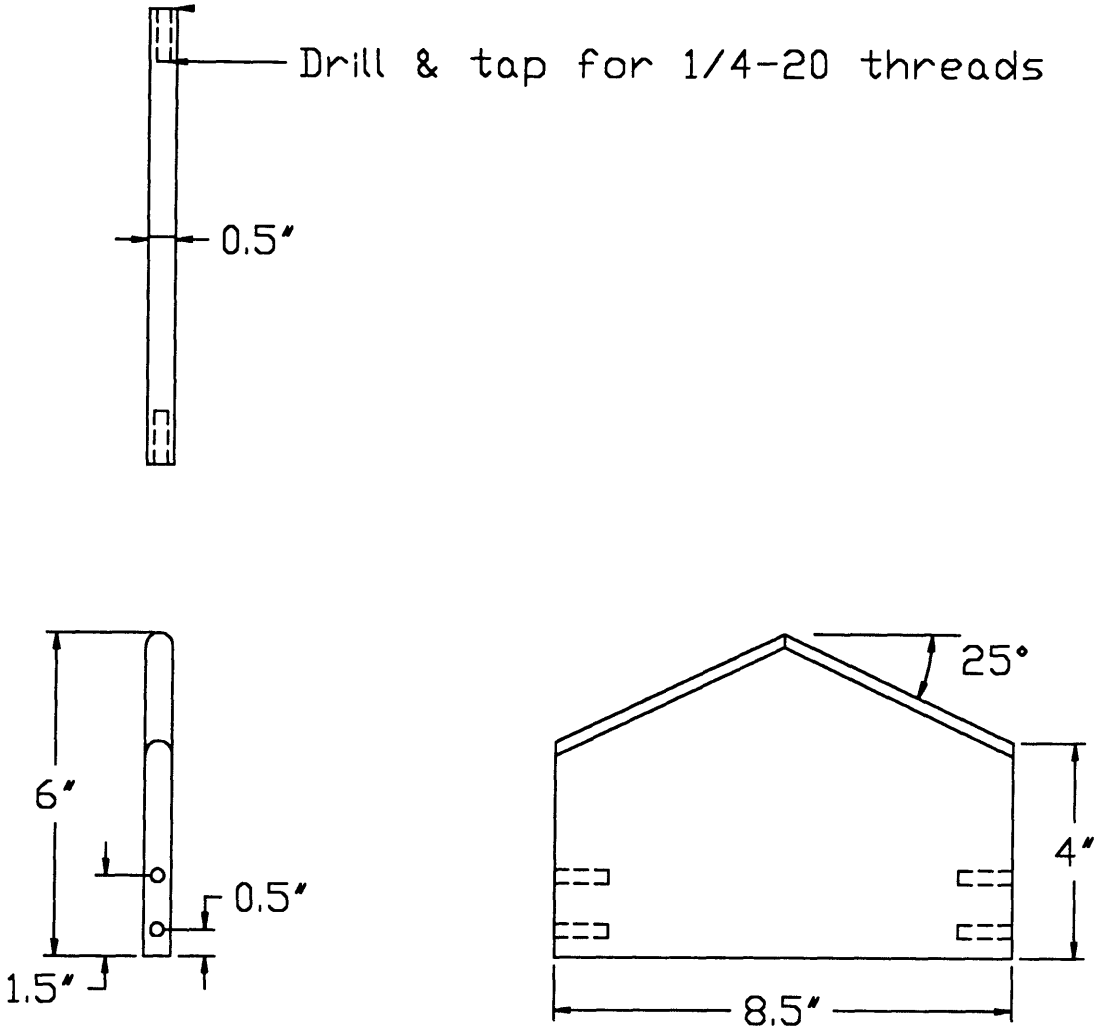

Figure B-4. Narrow Wedge Construction Drawing

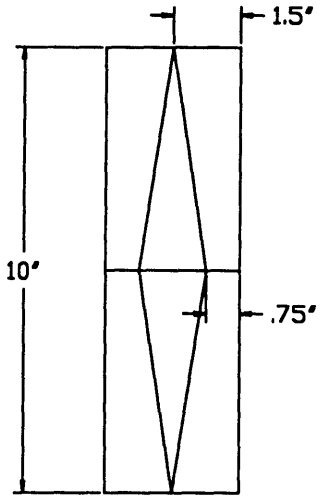

Top View

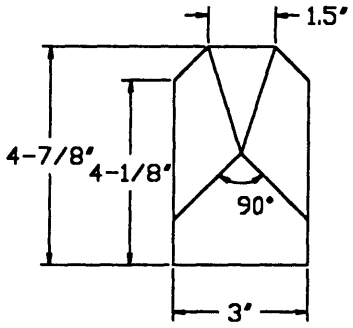

End View

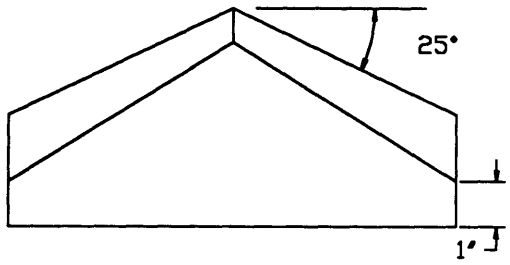

Side View

Figure B-5. Wide Wedge Construction Drawing

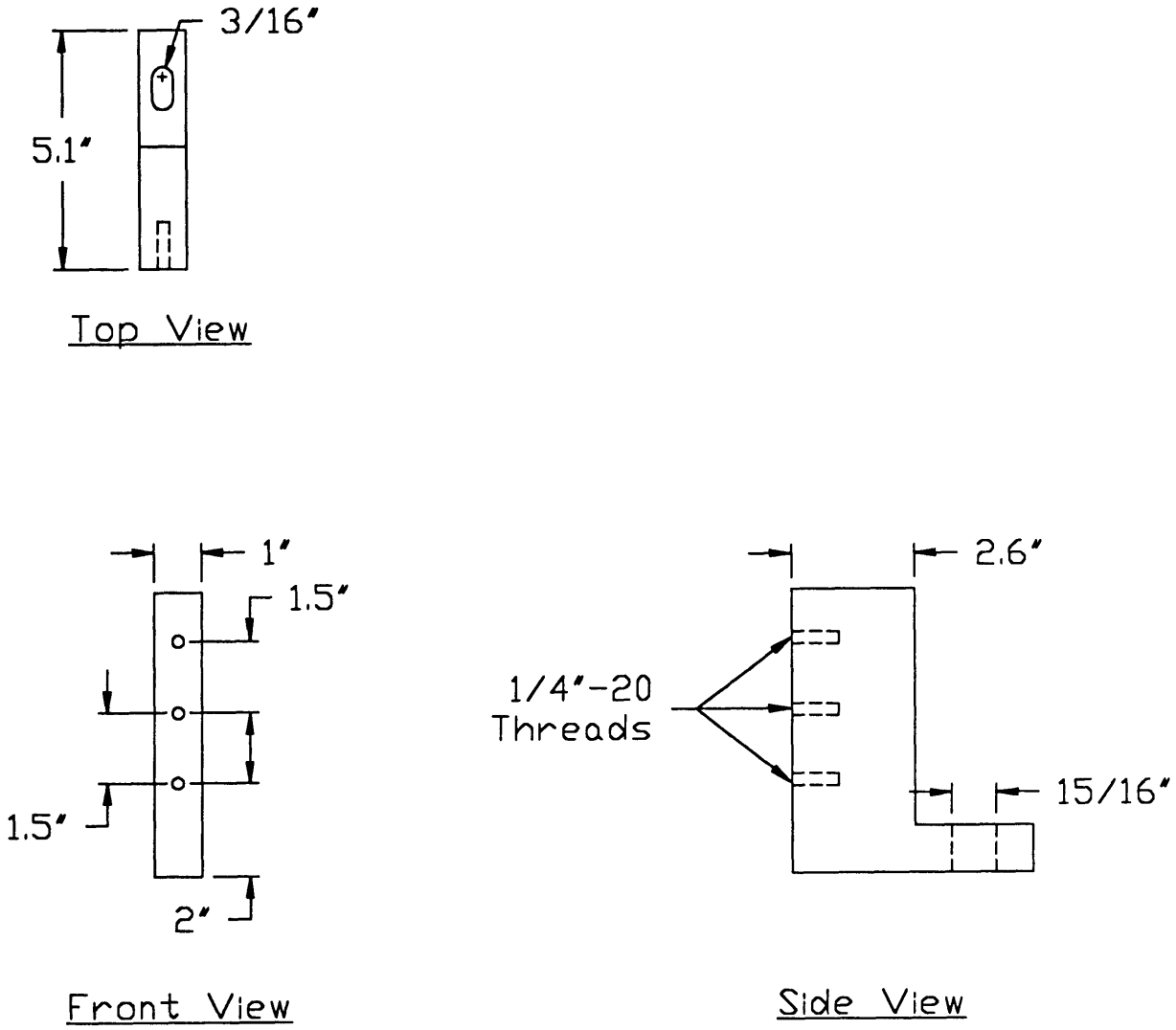

Figure B-6. Narrow Specimen Bracket Construction Drawing

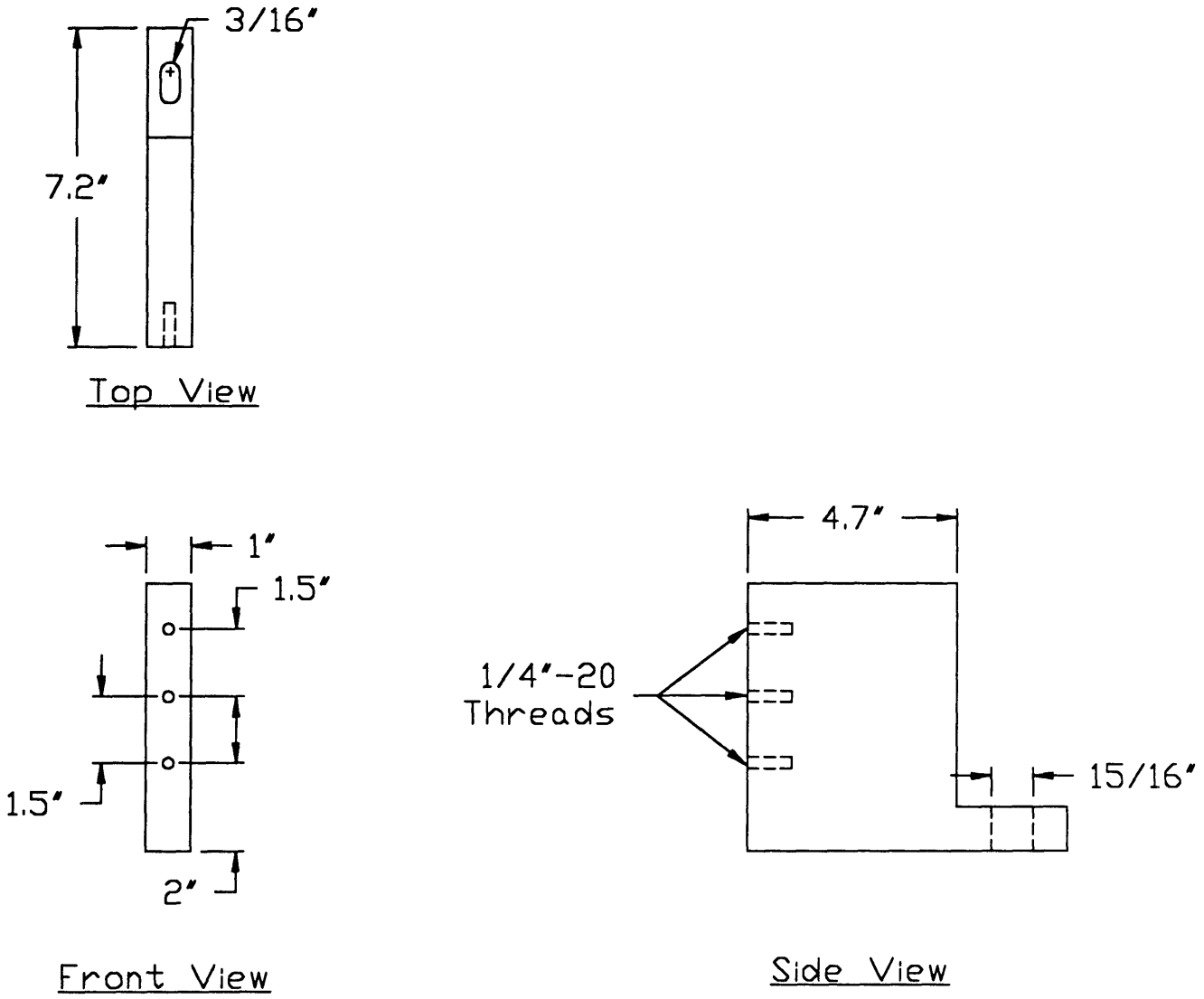

Figure B-7. Wide Specimen Bracket Construction Drawing

Appendix C - Lazy-T Weld Bend Tests

C.1 Purpose

This appendix provides information on Lazy-T weld bend tests conducted to investigate the strength of welds made using the electron beam welding (EBW) process. A secondary purpose of the tests was to provide information to assist in the development of full scale Lazy-T tests using material thicknesses commonly found in oil tanker design. The work in this appendix was done in collaboration with Mark D. Bracco.

The Lazy-T test was suggested by McClintock (1994) as a means for testing T-joints in the web folding mode of deformation and fracture. Figure 2-13 illustrates the weld failure modes proposed by McClintock (1994). The strength of EBW T-joints was questioned when the EBW joints did not fail even when subjected to large deformations during the scaled model testing conducted by Yahiaoui et al. (1994).

C.2 Limit Load Calculation

Figure C-1 shows a free body diagram for the T-joints tested. The load, P, is applied by the crosshead of a universal testing machine. Teflon tape was positioned under points A and B to minimize sliding friction.

Prior to conducting tests, a calculation of the limit load was made to determine the test equipment size needed. From the geometry of the problem, the following is determined;

$$\theta = \tan^{-1}(\frac{b_f}{2h_W}). \tag{C.1}$$

Summing moments about point A gives;

$$P_B \frac{h_W}{\cos\theta} - Pb_f \sin\theta = 0. \tag{C.2}$$

Defining b as the depth of the specimen (into the page), σ_{TS} as the tensile strength of the material and t_W as the thickness of the web gives the fully plastic bending moment;

$$M_P = \frac{b\sigma_{TS}t_W^{\ 2}}{4}. \tag{C.3}$$

Referring to the geometry in Figure C-2 where μ is the coefficient of sliding friction, the bending moment due to web folding at the weld joint is;

$$M = P_B h_W \cos\theta - \mu P_B h_W \sin\theta\,. \tag{C.4}$$

Setting the fully plastic bending moment, equation (C.3), equal to the bending moment at the weld joint, equation (C.4), results in;

$$P_B h_w(\cos\theta - \mu\sin\theta) = \frac{b\sigma_{TS}t_w^{\ 2}}{4}. \tag{C.5}$$

Substituting equation (C.2) into equation (C.5) and solving yields the limit load;

$$P_{limit} = \frac{\sigma b t_w^{\ 2}}{4b_f \sin\theta\cos\theta(\cos\theta - \mu\sin\theta)} \tag{C.6}$$

C.3 Test Results

A total of three t-stiffeners were tested. Table C-1 lists the dimensions of the specimens tested. For the calculations, values of $\sigma_{TS} = 324\ N/mm^2$ and $\mu = 0.3$ were used.

Table C-1. T-Stiffener Dimensions

Specimen	h_w (Inches)	b_f (Inches)	Depth, b (Inches)	Thickness (Inches)	Calculated Limit Load, N
1	1.644	1.5	0.482	0.029	47.7
2	1.644	1.5	0.465	0.029	46.0
3	1.647	1.5	0.499	0.029	49.4

Testing was performed on a Instron 4201 universal testing machine in the Remergence Laboratory at MIT. Based upon the calculated limit load, the 500 N load cell was selected for use. Unfortunately, it was inoperative and the tests were conducted with the 5 kN load cell instead. A total three Lazy-T tests were performed. The force displacement graphs are included as Figures C-3 through C-5.

During the Lazy-T tests, the crosshead direction was reversed several times in order to observe the effect of friction. The results of the reversal are depicted in Figures C-3 through C-5. As shown, there is evidence of 'sticking' during the crosshead motion. In spite of the sticking evident in the hysteresis loops, the contribution of sliding friction was determined to be not significant.

As shown in the Figures C-3 through C-5, the force starts to rise sharply when the crosshead displacement exceeds 25 mm. This coincides with the flattening of the T-joint. The same feature was observed on all tests, namely, the weld did not fail. A close examination of the crushed samples indicated the bending took place in the web.

C.4 Conclusions

Several conclusions were drawn from the Lazy-T testing. First, equation (C.6) provided an estimate of the limit load which was within 20% of that observed experimentally. Second, any welded joint should be strong enough so that the deformation occurs in the base metal, not the weld itself. In this case, EBW exhibited sufficient strength since the deformation occurred in the web on all tests. For future planning of full-scale Lazy-T tests, it appears as if friction is not a significant factor provided steps are taken to minimize its effect. The sticking observed during the compliance tests and in the hysteresis loops may be due to off center loading. An alternative may be the Lazy-L test, where the flange is trimmed at the weld joint and the legs are of equal length. The loading on this type of specimen would be symmetric throughout the test. Finally, the analysis can be extended so that the theoretical load is calculated as a function of cross-head displacement.

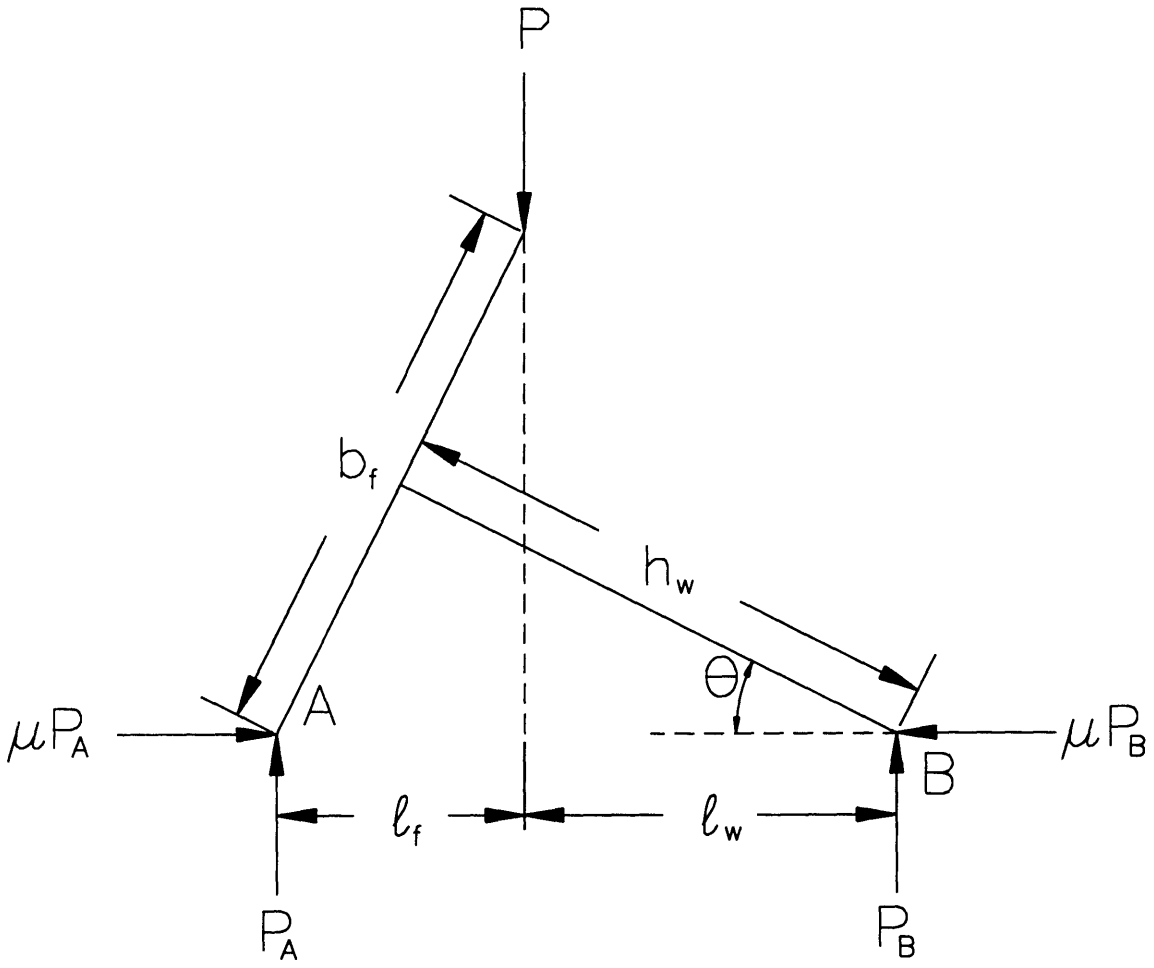

Figure C-1. T-Stiffener Geometry and Free Body Diagram

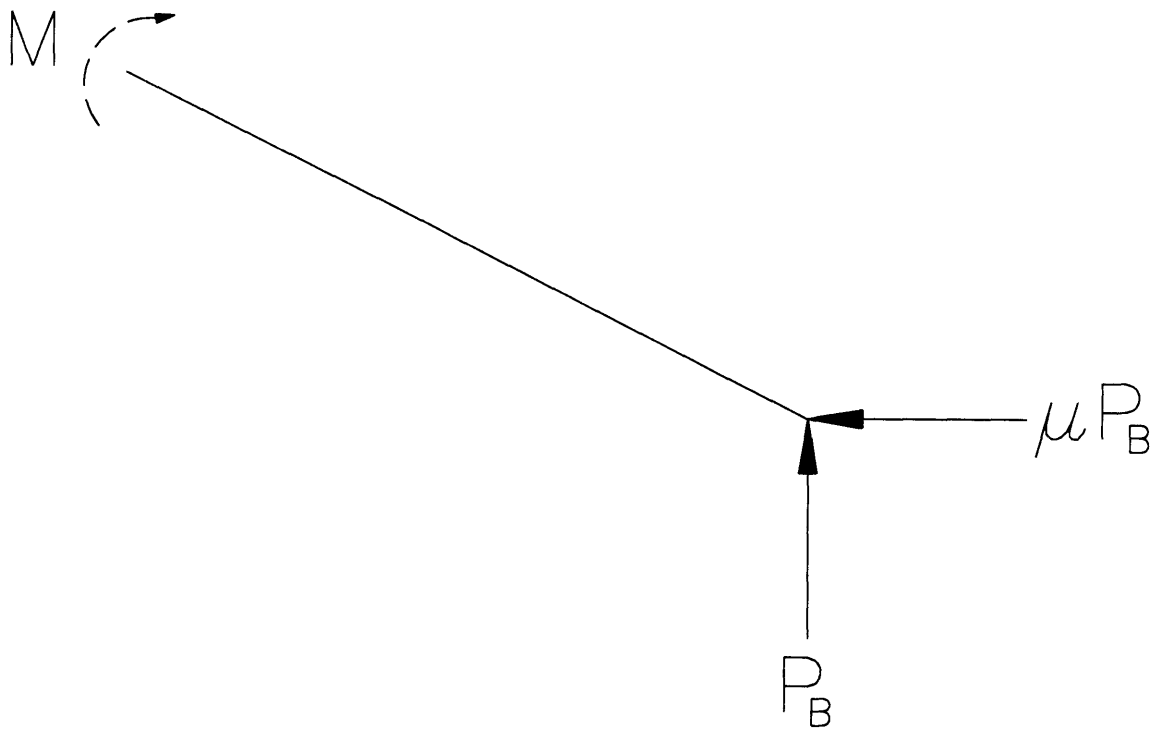

Figure C-2. Bending Moment at the Web Joint

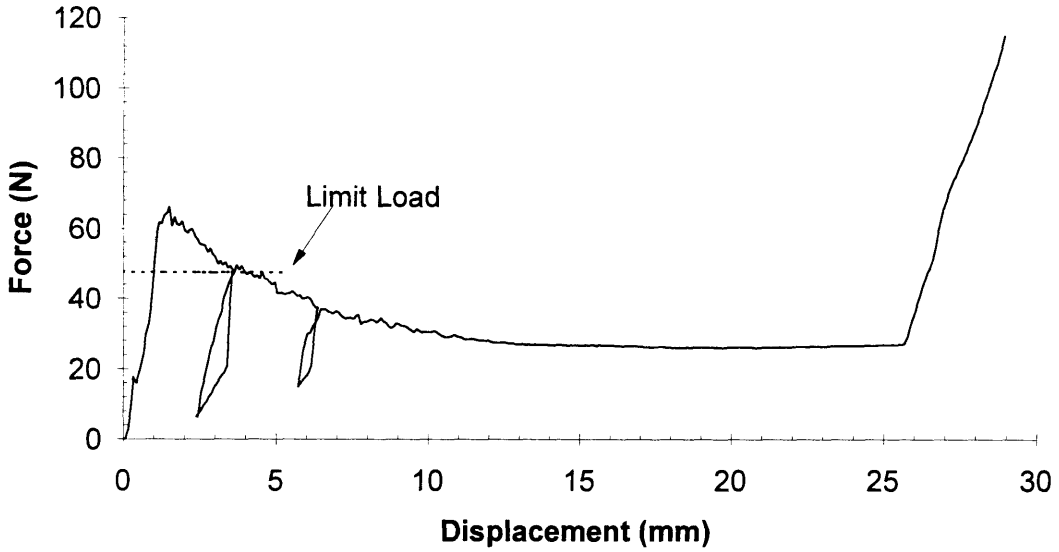

Figure C-3. Lazy-T Test Results for Specimen #1

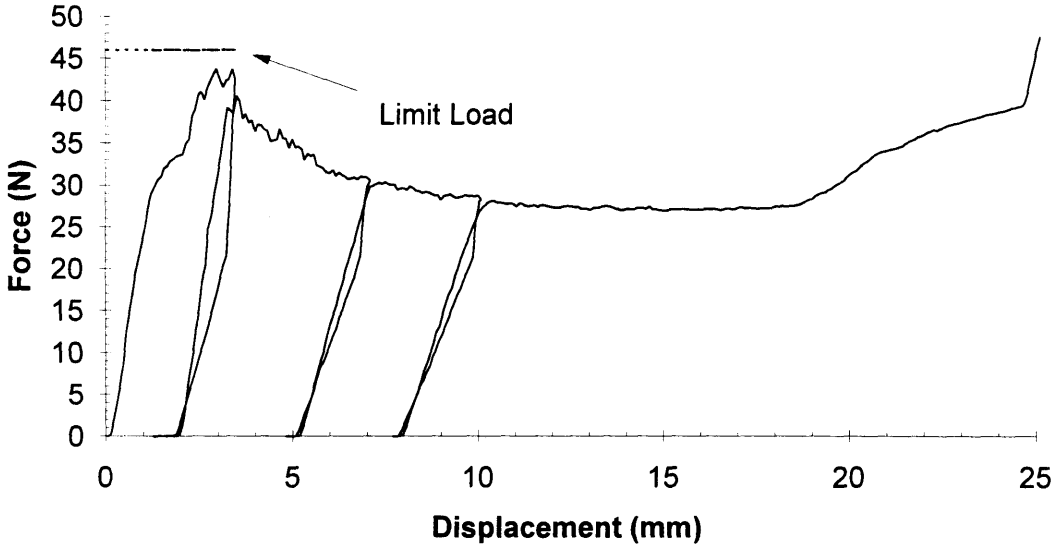

Figure C-4. Lazy-T Test Results for Specimen # 2

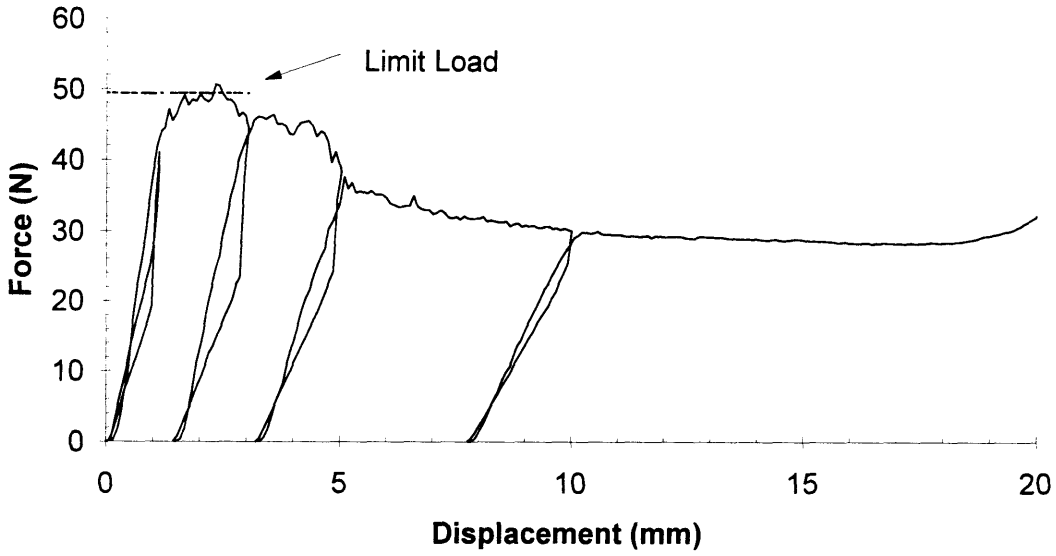

Figure C-5. Lazy-T Test Results for Test #3

Appendix D - Tensile Test Results

D.1 Discussion

Tensile tests results are reported here for the three material thickness used in fabrication of the scaled ship models. A total of twelve specimens were tested: four for each thickness with two each in the transverse and longitudinal direction to the roll axis. The tests were conducted in accordance with ASTM specification A370. The test specimen dimensions are shown in Figure D-1. The reported results include yield strength (YS), ultimate tensile strength (UTS), percent elongation, and the accompanying engineering stress-strain curves, as shown in Table D-1 and Figures D-2 through D-13. The work reported in this Appendix was done in collaboration with Mark D. Bracco.

Table D-1. Tensile Test Specimen Properties

Specimen No.	Thickness (mm)	Orientation (from roll axis)	0.2% YS (N/mm^2)	UTS (N/mm^2)	% Elongation
1	0.749	0°	244.8	328.9	41.3
2	0.749	0°	180.0	329.6	41.0
3	0.749	90°	175.8	319.9	41.3
4	0.749	90°	176.5	319.2	39.4
5	1.130	90°	211.7	332.3	38.5
6	1.130	90°	213.1	334.4	37.3
7	1.130	0°	229.6	338.5	38.0
8	1.130	0°	207.5	333.7	38.5
9	1.829	0°	153.1	299.9	45.9
10	1.829	0°	137.2	280.6	45.8
11	1.829	90°	145.5	282.7	44.7
12	1.829	90°	146.2	282.7	45.0

Conversion Factor: 0.006895 (N/mm^2) = 1 psi.

The results of Table D-1 can be averaged for each thickness as shown in Table D-2.

Table D-2. Tensile Test Specimen Averaged Properties

Thickness (mm)	Average 0.2% YS (N/mm^2)	Average UTS (N/mm^2)	Average % Elongation
0.749	194.3	324.4	40.8
1.130	215.5	334.8	38.1
1.829	145.5	286.5	45.4

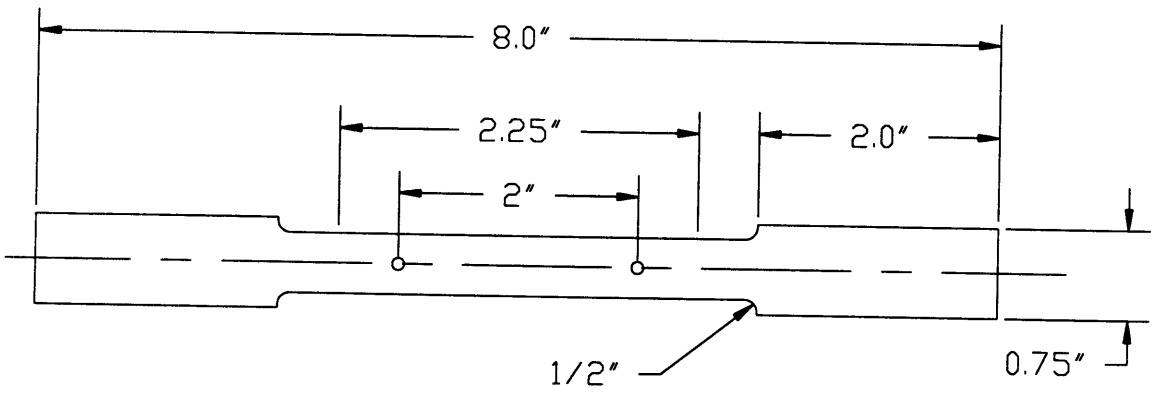

Figure D-1. ASTM A370 Flat Tensile Specimen

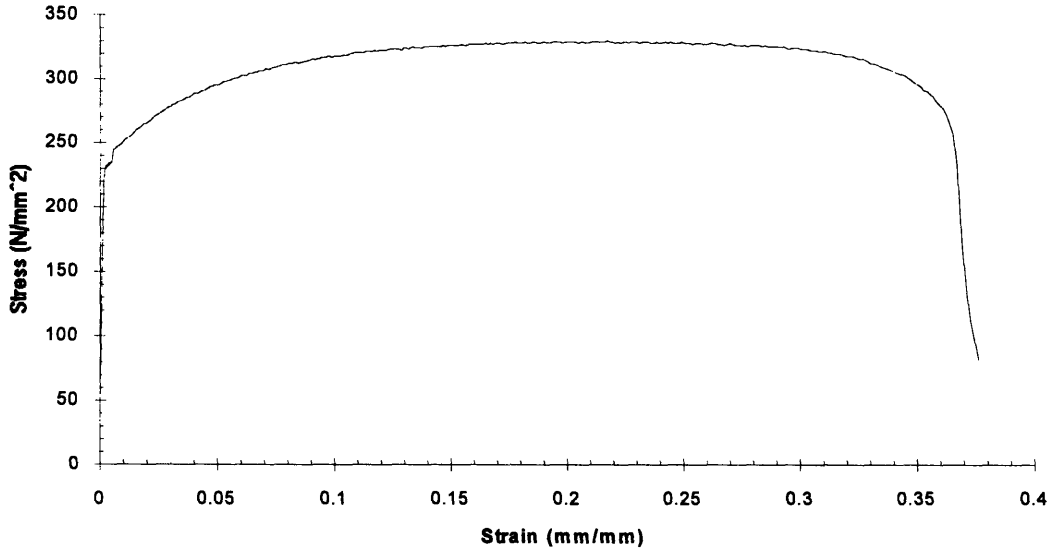

Figure D-2. Specimen 1 - Engineering Stress-Strain Curve (t = 0.749 mm, 0° from roll axis).

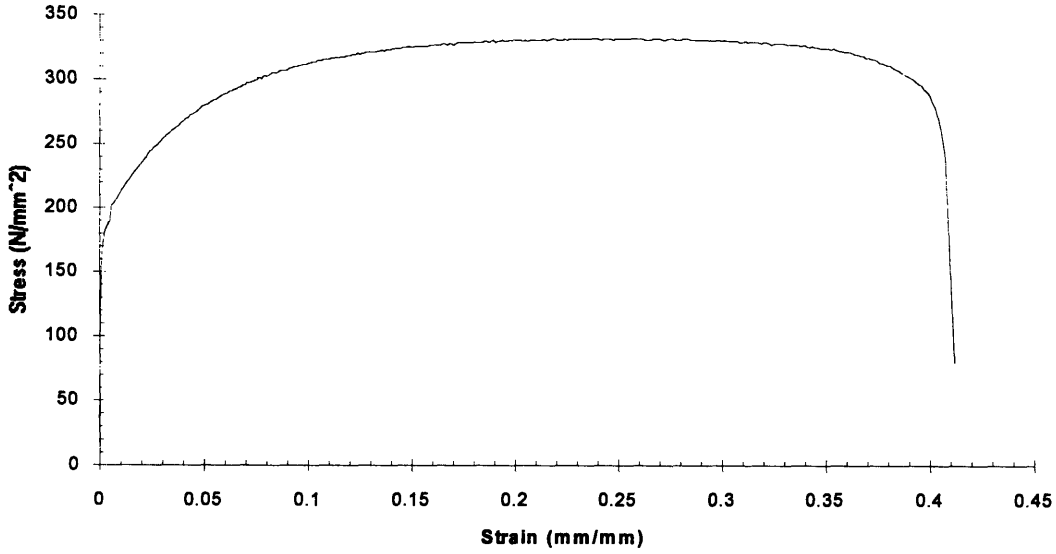

Figure D-3. Specimen 2 - Engineering Stress-Strain Curve (t = 0.749 mm, 0° from roll axis).

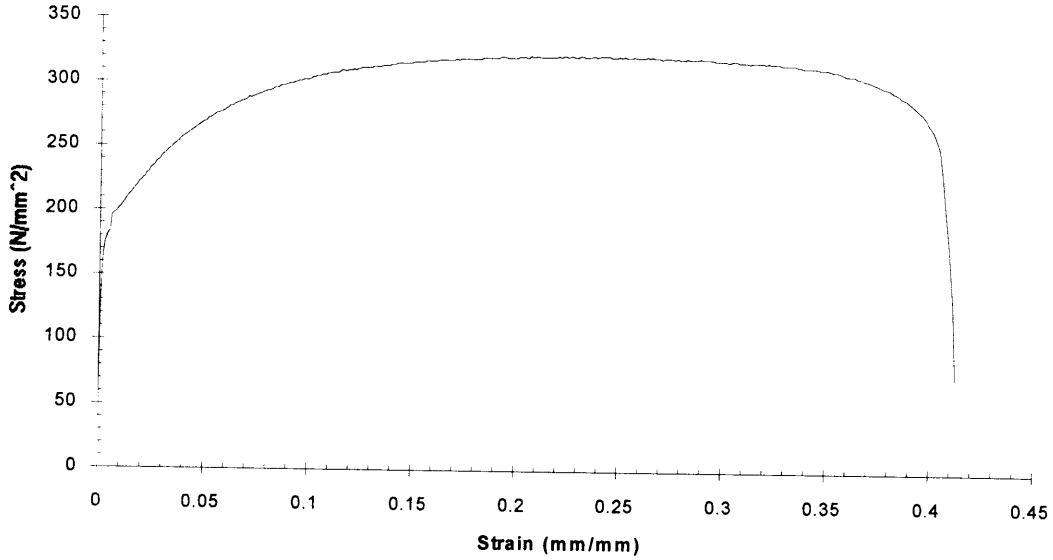

Figure D-4. Specimen 3 - Engineering Stress-Strain Curve (t = 0.749 mm, 90° from roll axis).

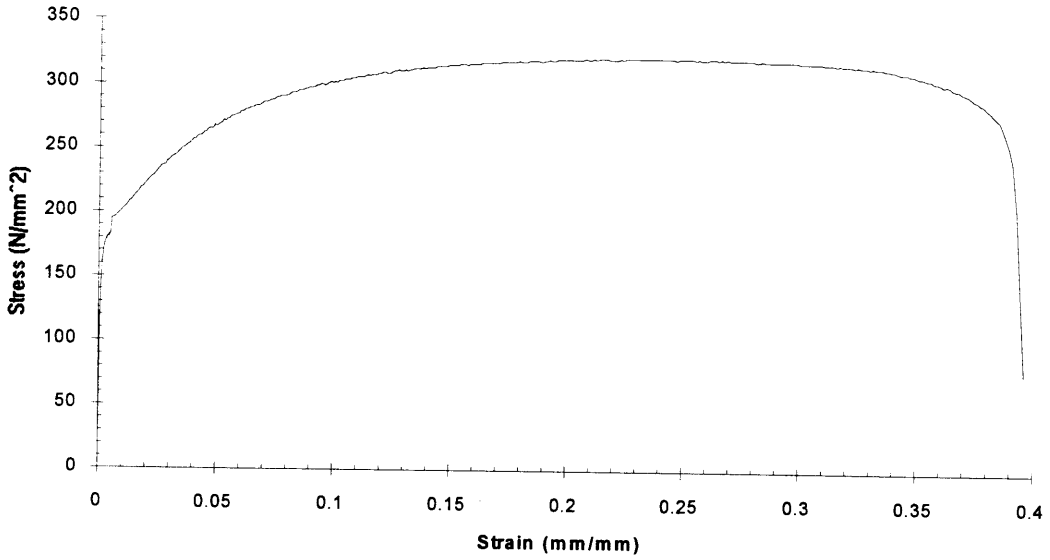

Figure D-5. Specimen 4 - Engineering Stress-Strain Curve (t = 0.749 mm, 90° from roll axis).

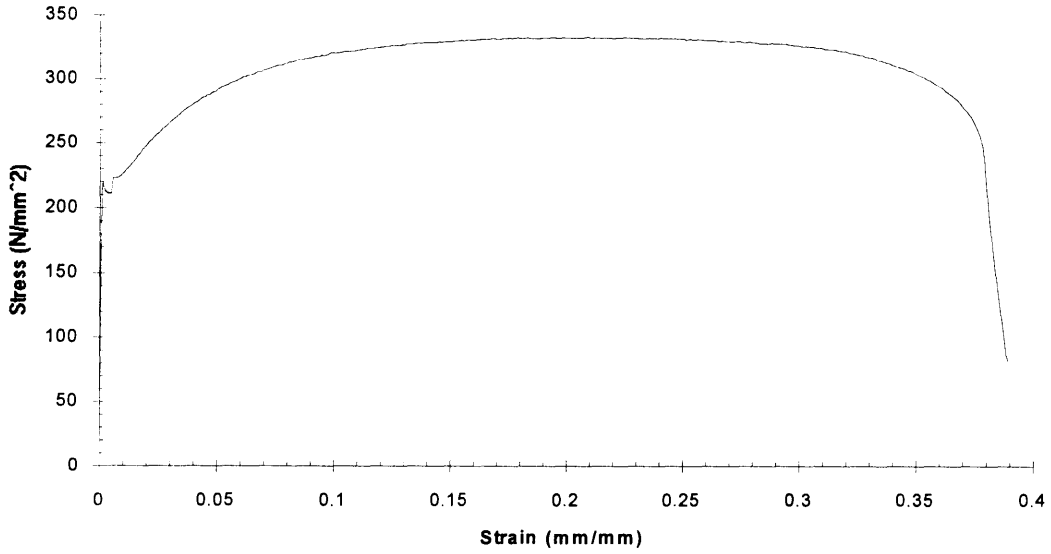

Figure D-6. Specimen 5 - Engineering Stress-Strain Curve (t = 1.130 mm, 90° from roll axis).

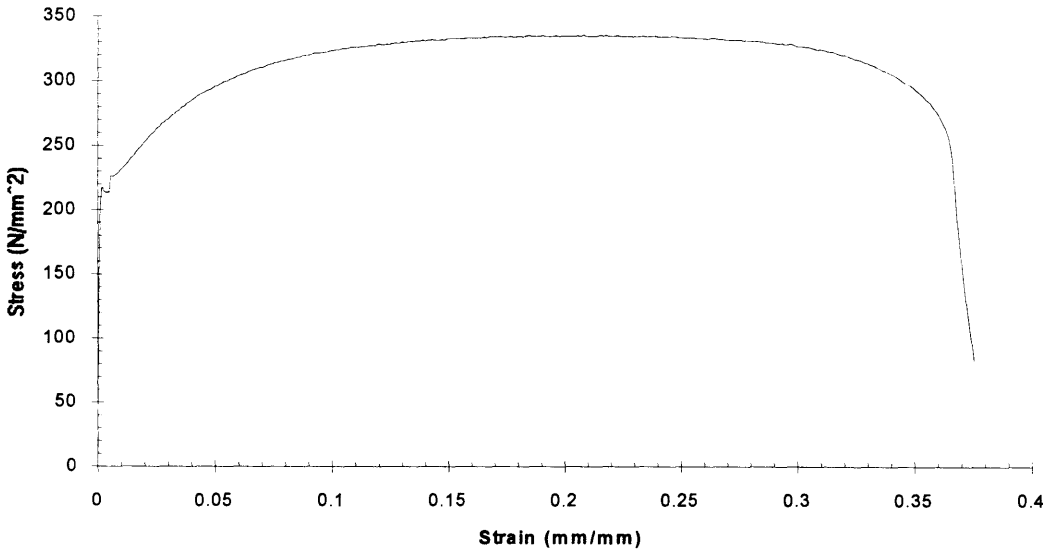

Figure D-7. Specimen 6 - Engineering Stress-Strain Curve (t = 1.130 mm, 90° from roll axis).

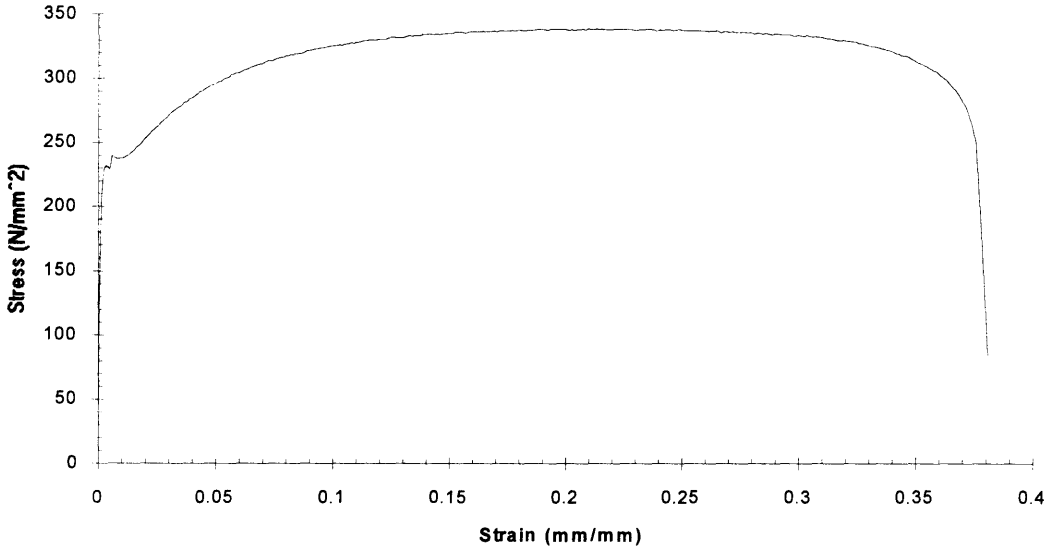

Figure D-8. Specimen 7 - Engineering Stress-Strain Curve (t = 1.130 mm, 0° from roll axis).

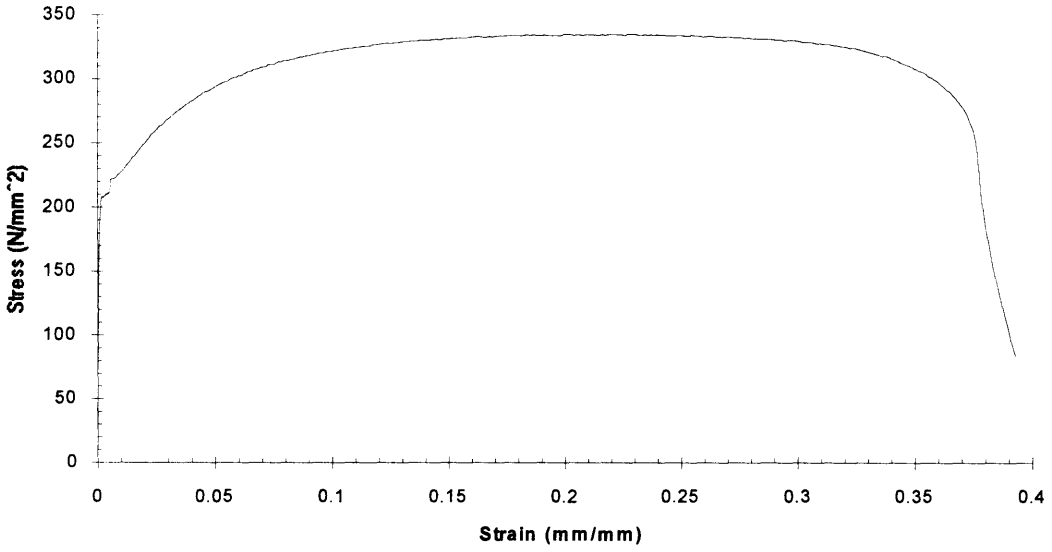

Figure D-9. Specimen 8 - Engineering Stress-Strain Curve (t = 1.130 mm, 0° from roll axis).

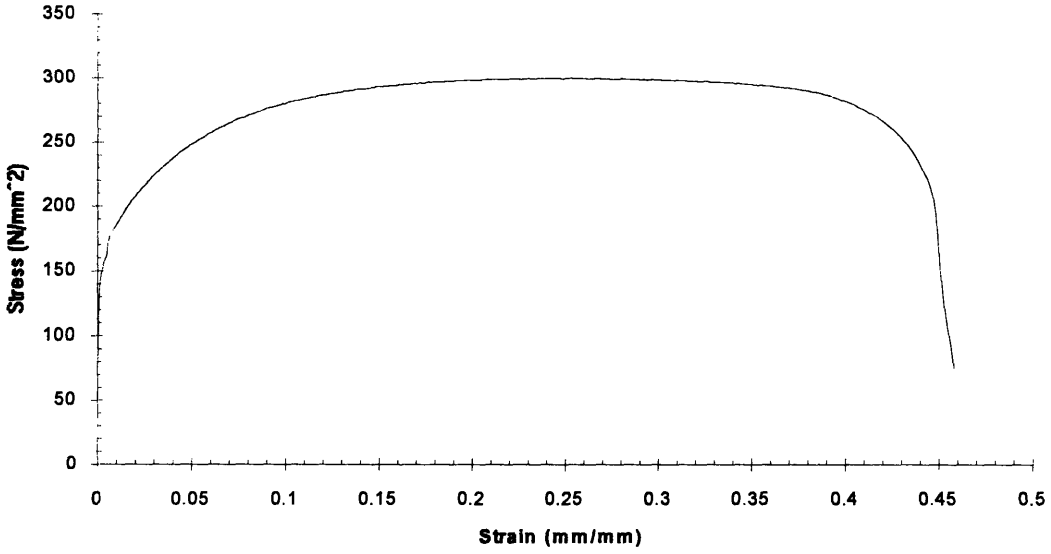

Figure D-10. Specimen 9 - Engineering Stress-Strain Curve (t = 1.829 mm, 0° from roll axis).

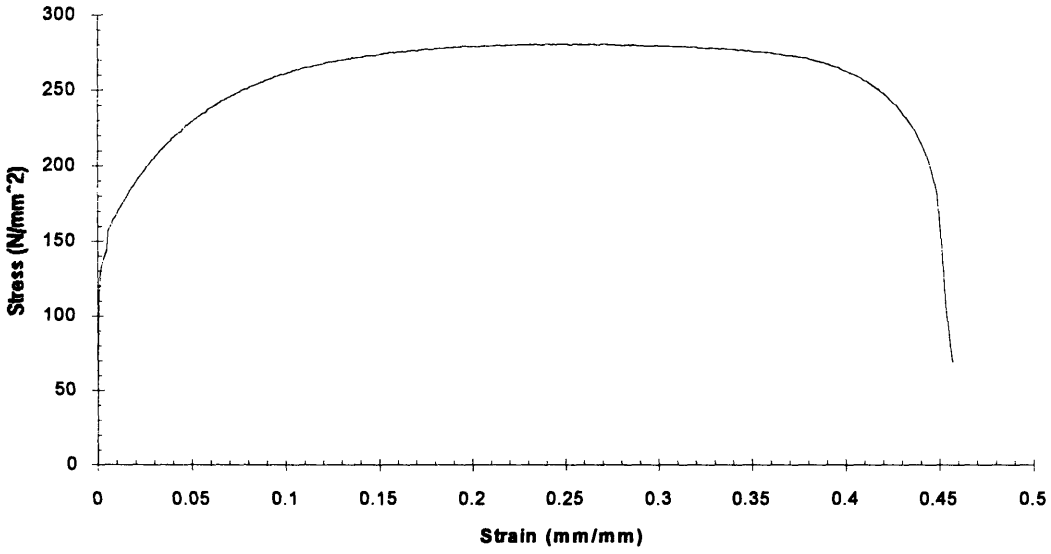

Figure D-11. Specimen 10 - Engineering Stress-Strain Curve (t = 1.829 mm, 0° from roll axis).

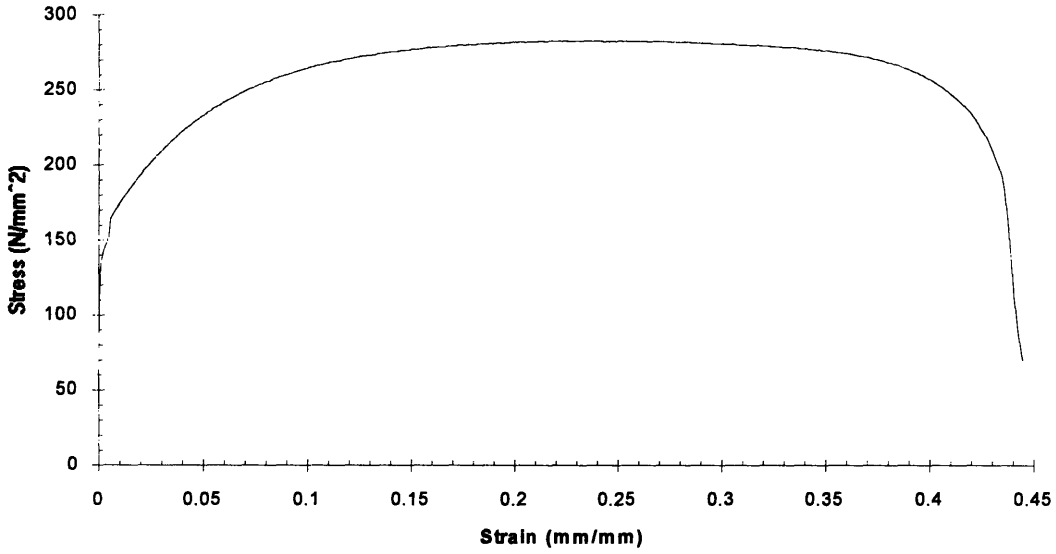

Figure D-12. Specimen 11 - Engineering Stress-Strain Curve (t = 1.829 mm, 90° from roll axis).

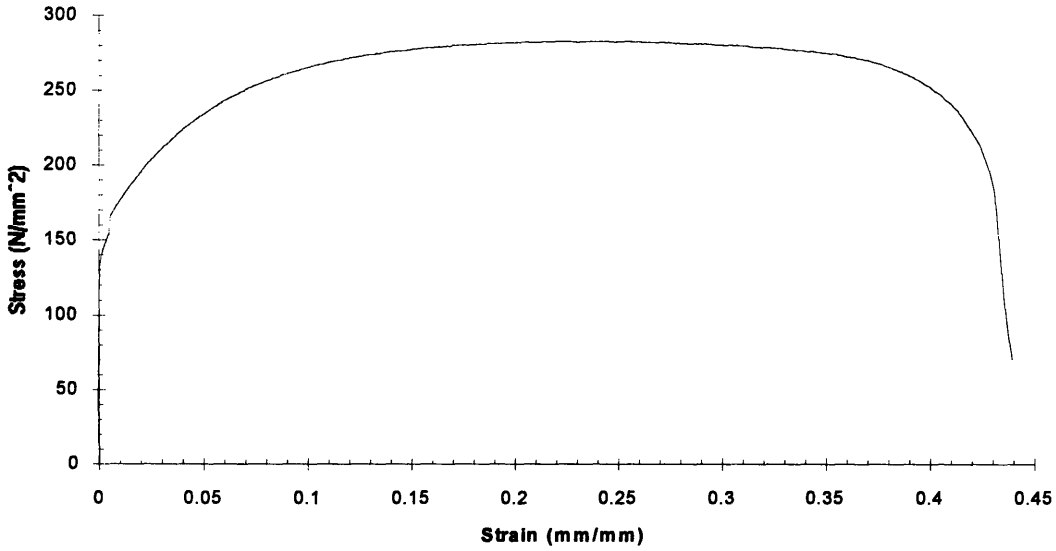

Figure D-13. Specimen 12 - Engineering Stress-Strain Curve (t = 1.829 mm, 90° from roll axis).

Appendix E - Crack Splitting Model Calculations

E.1 Model Description

The crack splitting model was based on the experimental observation that stiffening occurred when the wedge was at a distance equal to ηt away from the transverse member, where η varies from 7-10 and t is the plating thickness. It was assumed that the flap remained tangent to the wedge face throughout the process. Figure 4-3 depicts the undeformed and deformed geometry of the computational model. The model is valid for a wedge with a circular face.

As the wedge advances, the rate of rotation of the flap relative to the wedge, $\dot{\theta}^*$, continues to increase as the point of tangency travels around the circular wedge face. A displacement field is assumed such that the flap rigidly rotates about the stationary hinge line ℓ_6 through the angle ω from 0 to 90 degrees. In one form of the model, the rotation results in membrane stretching along the edge ℓ_0. The critical strain to rupture parameter, ε_{cr}, is introduced to avoid calculating excessive strains. The alternative form of the model considers the rate of work associated with the propagation of a crack along ℓ_0.

Figure E-1 depicts the relevant parameters as the wedge approaches to within ηt of the transverse member. From the geometry, the angle of the flap to the wedge as a function of wedge advancement is;

$$\theta^*(\Delta) = \sin^{-1}\left(\frac{B}{B+\eta t-\Delta}\right). \qquad \text{(E.1)}$$

Depending on plate thickness and wedge width, the initial flap-wedge angle, $\theta^*(\Delta = 0)$, could be less than or greater than the wedge semi-angle, θ. The steady-state cutting model, equation (1.4) assumes these angles are equal.

This was corrected in the computational model by applying a parabolic correction to the initial flap-wedge angle;

$$\theta^*(\Delta) = \theta^*(\Delta = 0) + [\theta - \theta^*(\Delta = 0)][1 - (\frac{\Delta}{\eta t})^2]. \qquad \text{(E.2)}$$

E.2 Rate of Membrane Work in the Flap

From the geometry of Figure E-2, the following is determined;

$$\ell_0 = \frac{\sqrt{2}B}{\sin\theta}\sqrt{1-\sin\theta}, \qquad \ell = \frac{\sqrt{2}B}{\sin\theta^*}\sqrt{1-\sin\theta^*}. \qquad \text{(E.3)}$$

The flap rotation angle is determined using equation (E.3) as;

$$\omega = \cos^{-1}(\frac{\ell}{\ell_0}) = \cos^{-1}(\frac{\sqrt{1-\sin\theta^*}}{\sqrt{1-\sin\theta}}). \qquad \text{(E.4)}$$

Figure E-2 depicts the membrane stretching across the opening. The maximum opening displacement is defined as;

$$u_1 = \sqrt{2}\ell_0\sqrt{1-\cos\omega}. \qquad \text{(E.5)}$$

It is assumed the displacement varies linearly as a function of z, or;

$$u = u_1\frac{z}{\ell_0}. \qquad \text{(E.6)}$$

The strain across the gap is also found as a function of z;

$$\varepsilon = \frac{u}{B/\sin\theta} = \frac{u_1 z \sin\theta}{\ell_0 B}. \tag{E.7}$$

The point at which the strain equals to the critical strain to rupture is found by setting equation (E.7) equal to ε_{cr};

$$z^* = \frac{\sqrt{2}\varepsilon_{cr} B\sqrt{1-\sin\theta}}{2\sin\theta\sqrt{1-\cos\omega}}. \tag{E.8}$$

Defining $N_0 t = \sigma_0 t$ as the fully plastic membrane force, $dS = d\eta d\xi$ and $\dot{\varepsilon} = d\dot{u}/d\xi$ as the velocity strain in local coordinates (η,ξ) rotating with the plate element, the rate of membrane work is;

$$\dot{W}_m = \int_S N_0 \dot{\varepsilon} dS \tag{E.9}$$

Consideration of both cracks results in a rate of membrane work of;

$$\dot{W}_m = 2N_0 \int_S \dot{u} d\xi. \tag{E.10}$$

The maximum strain rate, which occurs at the tip of the opening, is a function of the angular rate of flap opening;

$$\dot{u}_1 = \dot{\omega}\xi, \tag{E.11}$$

with a corresponding displacement rate function of;

$$\dot{u}(\xi) = \frac{\dot{\omega}\xi^2}{\ell_0}, \tag{E.12}$$

where

$$\dot{\omega} = f(\Delta)\dot{\Delta} \tag{E.13}$$

and

$$f(\Delta) = \frac{B\cos\theta^*}{\sqrt{(\eta t - \Delta)^2 + 2B(\eta t - \Delta)(B + \eta t - \Delta)}} \frac{1}{2\sqrt{\sin\theta^* - \sin\theta}\sqrt{1 - \sin\theta^*}}. \tag{E.14}$$

The rate of membrane work is found by substituting equation (E.12) into (E.10) and integrating;

$$\dot{W}_{m-flap} = 2N_0 \int_0^{z^*} \dot{u}(\xi) d\xi .. \tag{E.15}$$

The resulting integrated expression for the rate of flap membrane work is;

$$\dot{W}_{m-flap} = \frac{1}{6}\,\sigma_0\, t\, B^2\, f(\Delta)\, \dot{\Delta}\, \frac{\varepsilon_{cr}^3[1 - \sin\theta]}{\sin^2\theta[1 - \cos\omega]^{3/2}}. \tag{E.16}$$

E.3 Rate of Bending Work in the Flap

In general, the rate of bending work consists of work dissipated by the continuous deformation field and the work dissipated by the discontinuous deformation field. For this simplified deformation field, the plastic hinges are modeled as stationary and plate segments rotate as rigid bodies around the hinges. Thus, there is no continuous deformation and the bending rate of work term simplifies to;

$$\dot{W}_b = 2M_0\dot{\omega}\ell_6. \tag{E.17}$$

The length of the hinge line is found from geometry as;

$$\ell_6 = \frac{B}{\sin\theta}. \tag{E.18}$$

Substituting equations (E.13) and (E.18) into equation (E.17) results in the following expression for the rate bending work in the flap;

$$\dot{W}_{b-flap} = 2M_0\dot{\Delta}f(\Delta)\frac{B}{\sin\theta}. \tag{E.19}$$

E.4 Combined Membrane/Bending Mode

The rate of external work is defined as;

$$\dot{W}_{ext} = F_M\dot{\Delta}. \tag{E.20}$$

Equating the rates of internal and external work results in;

$$\dot{W}_{ext} = \dot{W}_{b-flap} + \dot{W}_{m-flap}. \tag{E.21}$$

Substituting equations (E.16), (E.19) and (E.20) into equation (E.21) and normalizing with respect to M_0 results in the following expression for the combined membrane/bending mode;

$$\frac{F_M}{M_0} = [\frac{2B^2(1-\sin\theta)}{3t\sin^2\theta}\frac{1}{(1-\cos\omega)^{3/2}} + \frac{2B}{\sin\theta}]f(\Delta). \tag{E.22}$$

E.5 Rate of Local Tearing Work in the Flap

The tearing resistance of plates and sheet metal can be described using the specific work of fracture, R^*. In general, R^* is not a material parameter and must be determined from carefully planned and interpreted experiments. For mild steel, its value ranges from 300-1000 N/mm. Using this concept and defining V as the rate of advance of the crack, the rate of local tearing work is defined as;

$$\dot{W}_t = R^* t V . \tag{E.23}$$

V is related to $\dot{\Delta}$ through the rate of change of the flap-wedge angle;

$$V = \frac{\dot{\theta} B}{\sin\theta} = \frac{B g(\Delta)\dot{\Delta}}{\sin\theta}, \tag{E.24}$$

where

$$g(\Delta) = \frac{B}{\sqrt{(\eta t - \Delta)^2 + 2B(\eta t - \Delta)(B + \eta t - \Delta)}}. \tag{E.25}$$

The rate of tearing work is thus defined as;

$$\dot{W}_t = \frac{2R^* t B}{\sin\theta} g(\Delta)\dot{\Delta}. \tag{E.26}$$

Substituting equation (E.26) instead of (E.16) into equation (E.21) and normalizing with respect to M_0 results in the following expression for the combined tearing/bending mode;

$$\frac{F_T}{M_0} = \frac{2B}{\sin\theta}[f(\Delta) + \frac{4R^*}{\sigma_0 t} g(\Delta)]. \qquad \text{(E.27)}$$

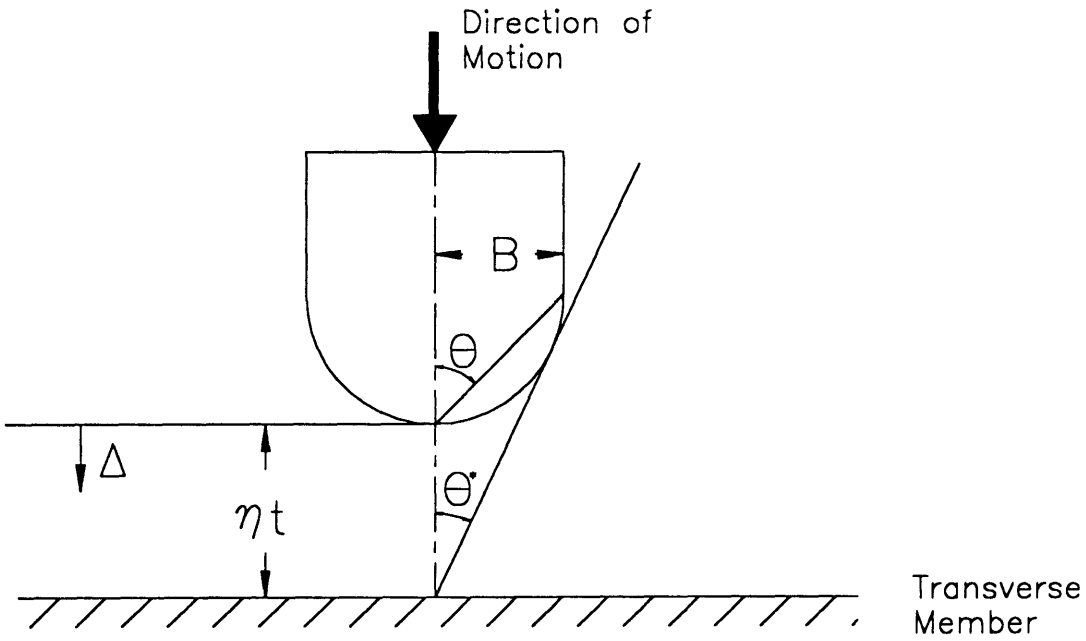

Figure E-1. Geometry As Wedge Approaches the Transverse Frame

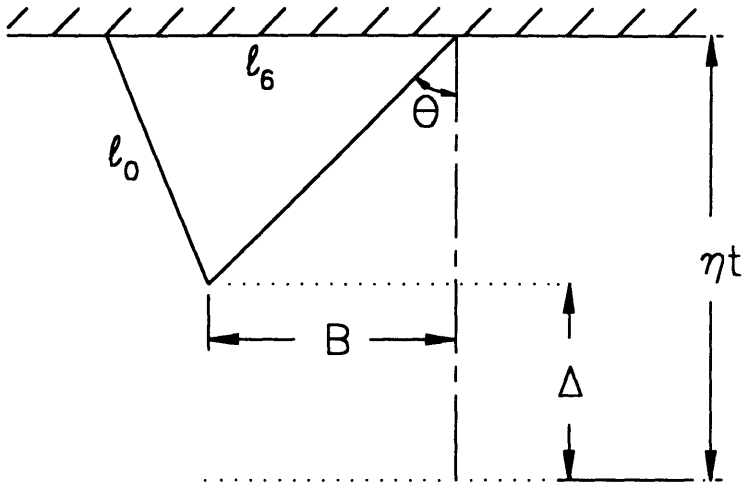

Top View at Transverse Member

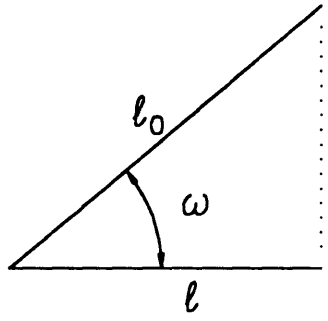

Flap Rotation Angle

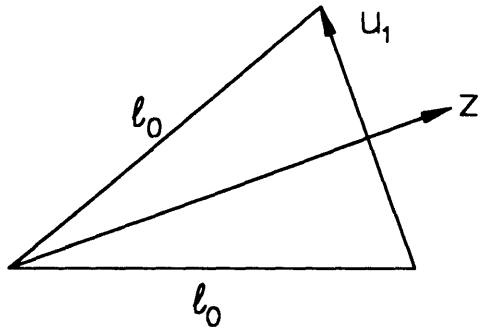

'z' Coordinate

Figure E-2. Crack Splitting Model Details

Appendix F - Web Girder Crushing Model Calculations

F.1 Model Description

Figure 4-5 depicts the undeformed and deformed geometry of the web girder crushing model. From experiments, it was observed that the width of the deformed region, 2ζ, was equal to the wedge width, 2B. It was postulated that H was the concertina fold length given by;

$$H = 0.56(2B)^{2/3} t_p^{1/3}, \tag{F.1}$$

where t_p is the thickness of the plate. Bending of the web was caused by six stationary hinge lines, while bending of the flange was caused by 2 stationary hinge lines. In addition, there was bending about the 2 hinge lines connected the base plate to the transverse member. The shaded area of Figure 4-5 illustrates the stretching in the deformed region.

The relationship between the angles α and β is derived from the geometry of the problems as;

$$\beta = \tan^{-1}\left[\frac{\tan\alpha}{1+2\tan^2\alpha}\right]. \tag{F.2}$$

The projected angle Φ between the first and third hinge lines is given by;

$$\cos\Phi = \frac{\zeta^2 + 2H\Delta}{\sqrt{(\Delta^2+\zeta^2)(\zeta^2+4H^2)}}, \quad \sin\Phi = \frac{2H\zeta - \Delta\zeta}{\sqrt{(\Delta^2+\zeta^2)(\zeta^2+4H^2)}}. \tag{F.3}$$

The angles θ_0 and $\phi_0 = \alpha + \beta$ depicted in Figure 4-5 are expressed as;

$$\cos\theta_0 = \frac{\zeta}{\sqrt{\Delta^2 + \zeta^2}}, \quad \sin\theta_0 = \frac{\Delta}{\sqrt{\Delta^2 + \zeta^2}} \tag{F.4}$$

$$\cos\phi_0 = \frac{\zeta}{\sqrt{\zeta^2 + 4H^2}}, \quad \sin\phi_0 = \frac{2H}{\sqrt{\zeta^2 + 4H^2}}. \tag{F.5}$$

F.2 Rate of Membrane Work

Defining $N_0 = \sigma_0 t_p$ as the fully plastic membrane force in the web, $dS = d\eta d\xi$ and $\dot{\varepsilon} = d\dot{u}/d\xi$ as the velocity strain in local coordinates (η,ξ) rotating with the plate element, the rate of membrane work is;

$$\dot{W}_m = \int_S N_0 \dot{\varepsilon} dS \tag{F.6}$$

The consideration of material points on either side of the centerline of the shaded portions results in a rate of membrane work of;

$$\dot{W}_m = 2N_0 \int_S \dot{u} d\eta. \tag{F.7}$$

The rate of membrane work in the flange (transverse member) and web (base plate) during the deformation process is;

$$\dot{W}_m = \dot{W}_{m-flange} + \dot{W}_{m-web}. \tag{F.8}$$

The in-plane stretching really takes place over the entire deformed region. The shaded area assists in visualizing the magnitude of the stretching.

The rate of membrane work of the flange is considered first. Figure F-1 illustrates the areas where the magnitude of stretching is calculated. The

stretching at the intersection of the web and flange is denoted as $u_{f\text{-}w}$ and considered the same for both for material continuity. From the geometry, the stretching and stretching rate are;

$$u_f = \sqrt{\Delta^2 + \zeta^2} - \zeta, \qquad \dot{u}_f = \frac{\Delta}{\sqrt{\Delta^2 + \zeta^2}}\dot{\Delta}. \tag{F.9}$$

From Figure 4-5, the stretching varies from $u_{f\text{-}w}$ at the weld joint to zero where the wedge ceases to be in contact with the transverse. The distance is denoted as $\rho\zeta$ with ρ defined as;

$$\rho = \frac{\Delta}{\zeta}\frac{1}{\tan\gamma}, \tag{F.10}$$

where γ is the angle complementary to the wedge sloping angle, α, illustrated in Figure 2-6. The average strain in the flange is calculated as;

$$u_{f-avg} = \frac{1}{\rho\zeta}\int_0^{\rho\zeta}(\frac{\rho\zeta - z}{\rho\zeta})u_{f-w}dz = \frac{1}{2}u_{f-w}. \tag{F.11}$$

Thus, the average strain rate in the flange is;

$$\dot{u}_{f-avg} = \frac{1}{2}\dot{u}_{f-w}. \tag{F.12}$$

Substituting equation (F.12) back into equation (F.7) and defining $\overline{N_0}t_f$ as the fully plastic membrane force in the flange results in a rate of membrane work in the flange of;

$$\dot{W}_{m-flange} = 2\overline{N_0}\int \dot{u}_{f-avg} d\eta = \overline{N_0}\rho\zeta \frac{\Delta}{\sqrt{\Delta^2+\zeta^2}}\dot{\Delta}. \qquad (F.13)$$

The following substitution is used to express $\dot{\Delta}$ in terms of $\dot{\Phi}$;

$$\dot{\Delta} = -\dot{\Phi}\frac{\Delta^2+\zeta^2}{\zeta}. \qquad (F.14)$$

Now, consider the rate of membrane work in the web. The displacement at the intersection of the second hinge lines is denoted as u_x as shown in Figure F-1. From the geometry of the problem, u_x is determined as;

$$u_x = \zeta\frac{(\sqrt{2}\cos\alpha - \cos\beta)\sin\Phi + \cos\beta\cos\Phi - \cos\alpha}{[\cos\beta(\sin(\Phi - \cos\Phi) + \cos\alpha]^2\cos\alpha}, \qquad (F.15)$$

and the corresponding strain rate is;

$$\dot{u}_x = -\sqrt{2}\dot{\Phi}\zeta\frac{\cos\alpha\cos\beta - \cos^2\alpha\cos\Phi}{[\cos\beta(\sin\Phi - \cos\Phi) + \cos\alpha]^2\cos\alpha}. \qquad (F.16)$$

The average strain in the web is calculated as;

$$u_{web-avg} = \frac{1}{2H}\{\int_0^H [u_{f-w} + \frac{z}{H}(u_x - u_{f-w})] + \int_H^{2H}\frac{u_x}{H}(2H - z)dz\} = \frac{u_{f-w}}{4} + \frac{u_x}{2}. \qquad (F.17)$$

The corresponding average strain rate in the web is;

$$\dot{u}_{web-avg} = \frac{\dot{u}_{f-w}}{4} + \frac{\dot{u}_x}{2}. \qquad (F.18)$$

Substituting equation (F.17) into equation (F.7) and integrating results in the following rate of membrane work in the web;

$$\dot{W}_{m\text{-}web} = 4\,N_0\,H\,[-\frac{\Delta}{4\zeta}\sqrt{\Delta^2+\zeta^2} + \frac{\zeta\,\sin\phi_0\,(\cos\alpha\,\cos\Phi-\cos\beta)}{2\,(\cos\alpha\,\sin\phi_0-\cos\beta\,\sin\theta_0)^2}]\dot{\Phi}. \qquad \text{(F.19)}$$

F.3 Rate of Bending Work

In general, the bending work rate consists of work dissipated by the continuous deformation field and the work dissipated by the discontinuous deformation field. For this simplified deformation field, all plastic hinges are modeled as stationary and plate segments between the hinges rotate as rigid bodies. Thus, there is no continuous deformation and the bending work rate term simplifies to;

$$\dot{W}_b = 2M_0[\dot{\theta}_1\ell_1+\dot{\theta}_2\ell_2+\dot{\theta}_3\ell_3]+2\overline{M_0}[\dot{\theta}_4\ell_4+\dot{\theta}_5\ell_5]; \qquad \text{(F.20)}$$

where $M_0 = \sigma_0\,t_p^{\,2}\,/\,4$ and $\overline{M_0} = \sigma_0\,t_f^{\,2}\,/\,4$ are the fully plastic bending moments in the web and flange respectively. The lengths of the hinge lines are found from geometry as;

$$\ell_1=\zeta,\quad \ell_2=\frac{\zeta}{\cos\alpha},\quad \ell_3=\frac{\zeta}{\cos\phi_0},\quad \ell_4=\zeta\sqrt{1+\rho^2},\quad \ell_5=\sqrt{\Delta^2+\zeta^2} \qquad \text{(F.21)}$$

Note that ℓ_5 is the length of the hinge line underneath the indenter as discussed later in the section.

Figure F-2 depicts the rotation angles during deformation. θ_4, which is not included in Figure F-2, is the angle the flaps rotate about ℓ_4. Thus, the rotation angles for each hinge line are found from the geometry as;

$$\cos\theta_1 = \frac{\cos\beta - \cos\alpha\cos\Phi}{\sin\alpha\sin\Phi}, \qquad \cos\theta_2 = \frac{-\cos\alpha\cos\beta + \cos\Phi}{\sin\alpha\sin\beta},$$

$$\cos\theta_3 = \frac{\cos\alpha - \cos\beta\cos\Phi}{\sin\beta\sin\Phi}, \qquad \sin\theta_4 = \Delta\sqrt{\frac{1+\rho^2}{\rho^2\zeta^2 + (1+\rho^2)\Delta^2}}, \qquad \text{(F.22)}$$

$$\sin\theta_5 = \frac{\Delta}{\zeta}\sqrt{\frac{\Delta^2 + \zeta^2}{\rho^2\zeta^2 + \Delta^2(1+\rho^2)}},$$

while the rotation rates are found by differentiating with respect to time;

$$\dot{\theta}_1 = \frac{\dot{\Phi}(\cos\beta\cos\Phi - \cos\alpha)}{\sin\Phi\sqrt{C_1 + C_2\cos\Phi - \cos^2\Phi}}$$

$$\dot{\theta}_2 = \frac{\dot{\Phi}\sin\Phi}{\sin\Phi\sqrt{C_1 + C_2\cos\Phi - \cos^2\Phi}} \qquad \text{(F.23)}$$

$$\dot{\theta}_3 = \frac{\dot{\Phi}(\cos\alpha\cos\Phi - \cos\beta)}{\sin\Phi\sqrt{C_1 + C_2\cos\Phi - \cos^2\Phi}}$$

$$\dot{\theta}_4 = \frac{\rho\sqrt{1+\rho^2}}{\rho^2 + (1+\rho^2)\psi^2}\frac{\dot{\Delta}}{\zeta}, \qquad \dot{\theta}_5 = \frac{(1+\rho^2)\psi^4 + 2\rho^2\psi^2 + \rho^2}{[\rho^2 + (1+\rho^2)\psi^2]\sqrt{(\rho^2 + \rho^2\psi^2 - \psi^4)(1+\psi^2)}}\frac{\dot{\Delta}}{\zeta}$$

where

$$C_1 = \sin^2\alpha - \cos^2\beta, \qquad C_2 = 2\cos\alpha\cos\beta$$

$$C_3 = \cos^2\alpha + \frac{\cos\alpha\cos\beta}{\cos\phi_0} + 1, \qquad C_4 = \frac{\cos^2\alpha}{\cos\phi_0} + \cos\alpha\cos\beta, \qquad \text{(F.24)}$$

and

$$\psi = \frac{\Delta}{\zeta}.$$

Substituting equations (F.21) and (F.23) into equation (F.20) yields the rate of bending work in the web as;

$$\dot{W}_{b\text{-}web} = -2\,\zeta\, M_0\, \dot{\Phi}\, [\frac{C_3 - C_4 \cos\Phi - \cos^2\Phi}{\cos\alpha\, \sin\Phi\, \sqrt{C_1 + C_2\cos\Phi - \cos^2\Phi}}], \qquad (F.25)$$

and the rate of bending work in the flange as;

$$\dot{W}_{b\text{-}flange} = -2M_0\dot{\Phi}(\frac{\Delta^2+\zeta^2}{\zeta})\,[\frac{\rho(1+\rho^2)}{\rho^2+(1+\rho^2)\psi^2} + \frac{\rho^2+2\rho^2\psi^2+(1+\rho^2)\psi^4}{[\rho^2+(1+\rho^2)\psi^2]\sqrt{\rho^2+\rho^2\psi^2-\psi^4}}]\,\frac{t_f^2}{t_p^2}. \qquad (F.26)$$

Up to this point, the solution has considered the action of the wedge to be applied as a knife edge. In reality, a portion of the hinges in the central part of the web and the flange under the wedge undergo rotation during deformation, but no stretching. This is denoted as the indenter effect. The angles of the first and third hinges lines in the web under the indenter are expressed as;

$$\cos\theta_1 = \cos\theta_3 = 1 - \frac{\Delta}{2H}. \qquad (F.27)$$

The corresponding rotation rates of the first and third hinge lines are;

$$\dot{\theta}_1 = \dot{\theta}_3 = \frac{\dot{\Delta}}{\sqrt{4\Delta H - \Delta^2}}. \qquad (F.28)$$

The rotation rate of the flange hinge line due to the indenter effect is equal to the rotation rate of γ. Geometrically, γ is defined as;

$$\tan\gamma = \frac{\Delta}{\rho\zeta}. \tag{F.29}$$

The rotation rate of the flange hinge line is then;

$$\dot{\gamma} = \frac{\rho}{\rho^2 + \psi^2}\frac{\dot{\Delta}}{\zeta}. \tag{F.30}$$

The hinge lines are modeled as stationary and the plate segments as rigid bodies, thus only the discontinuous deformation field is considered. Defining b_1 as the width of the wedge over which the indenter effect occurs, and substituting equations (F.28) and (F.30) into equation (4.2) results in the rate of bending work due to the indenter;

$$\dot{W}_{b-ind} = M_0 b_1 \dot{\Delta}\left[\frac{4}{\sqrt{4\Delta H - \Delta^2}} + \frac{2\rho}{(\rho^2 + \psi^2)\zeta}\right]. \tag{F.31}$$

F.4 Rate of External Work

The rate external work done during the deformation of the web and flange is;

$$\dot{W}_{ext} = F_p\dot{\Delta}. \tag{F.32}$$

Using the relation for $\dot{\Delta}$ in terms of $\dot{\Phi}$ from equation (F.14) and substituting into equation (F.32) results in;

$$\dot{W}_{ext} = -F_p\dot{\Phi}\frac{\Delta^2 + \zeta^2}{\zeta}. \tag{F.33}$$

F.5 Crushing Force

Equating rates of internal and external work results in;

$$\dot{W}_{ext} = \dot{W}_{b\text{-}web} + \dot{W}_{b\text{-}flange} + \dot{W}_{m\text{-}web} + \dot{W}_{m\text{-}flange} + \dot{W}_{b\text{-}ind}. \qquad (F.34)$$

Substituting equations (F.13), (F.19), (F.25), (F.26) and (F.31) into equation (F.34) results in an expression for the crushing force. The final expression, in nondimensionalized form;

$$\frac{F_p}{M_0} = \frac{1}{1+\psi^2}\left[\frac{2(C_3 - C_4\cos\Phi - \cos^2\Phi)}{\cos\alpha\sin\Phi\sqrt{C_1 + C_2\cos\Phi - \cos^2\Phi}} - 8H^*\frac{\sin\phi_0(\cos\alpha\cos\Phi - \cos\beta)}{(\cos\alpha\sin\phi_0 - \cos\beta\sin\theta_0)^2}\right]$$
$$+ 2t^{*2}\left[\frac{\rho(1+\rho^2)}{\rho^2 + (1+\rho^2)\psi^2} + \frac{\rho^2 + 2\rho^2\psi^2 + (1+\rho^2)\psi^2}{\rho^2 + (1+\rho^2)\psi^2}\frac{1}{\sqrt{\rho^2 + \rho^2\psi^2 - \psi^4}}\right]$$
$$+ 4H^*\sin\theta_0(1 + t^*\rho\zeta^*) + b_1^*\left[\frac{4}{\sqrt{\Delta^*(4-\Delta^*)}} + \frac{2t^{*2}\rho}{(\rho^2+\psi^2)\zeta^2}\right]$$

(F.35)

where the nondimensionalized quantities are defined as;

$$\psi = \frac{\Delta^*}{\zeta^*} = \frac{\Delta}{\zeta}, \quad \Delta^* = \frac{\Delta}{H}, \quad \zeta^* = \frac{\zeta}{H}, \quad H^* = \frac{H}{t_p}, \quad t^* = \frac{t_f}{t_p}, \quad b_1^* = \frac{b_1}{H}. \qquad (F.36)$$

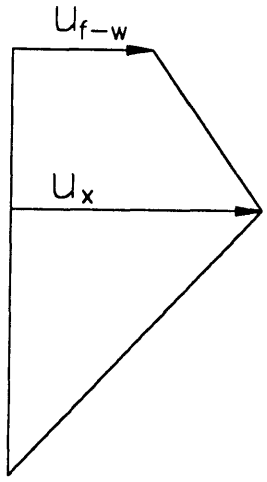

Figure F-1. Expanded View of Stretched Area

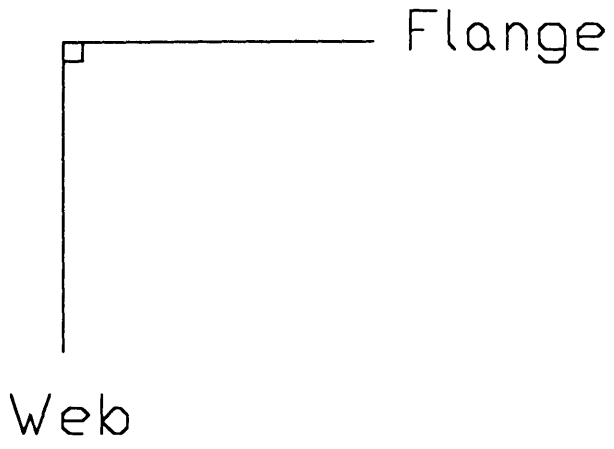

Section A-A Undeformed

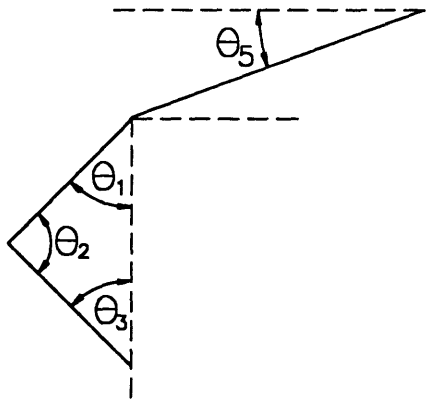

Section A-A Deformed

Figure F-2. Hinge Rotation Angles